Jeffery Selorm Adorkor

Modelling and validation of energy storage components for dynamical analysis of offshore energy systems

Master's thesis in Renewable Energy in the Marine Environment
Supervisor: Elisabetta Tedeschi
June 2020

Master's thesis

NTNU
Norwegian University of
Science and Technology

Jeffery Selorm Adorkor

Modelling and validation of energy storage components for dynamical analysis of offshore energy systems

Master's thesis in Renewable Energy in the Marine Environment
Supervisor: Elisabetta Tedeschi
June 2020

Norwegian University of Science and Technology
Faculty of Information Technology and Electrical Engineering
Department of Electric Power Engineering

NTNU
Norwegian University of
Science and Technology

Abstract

The increasing growth in renewable energy integration and the expansion of transmission and distribution networks in offshore energy systems necessitates an optimal level of system stability and reliability. An important issue in this regard is maintaining generation-demand balance to mitigate the effects of intermittency of renewable sources and variations in load demand. Energy storage is a proven effective solution to enhance grid resiliency by compensating for power mismatch due to the factors mentioned above.

This master's thesis investigates the contribution of energy storage, specifically hybrid energy storage systems (HESS), to the improvement of grid resiliency against load variations. The power system under study is made up of a HESS connected to an AC offshore remote area power system (RAPS) via a two-stage power converter. The focus of this project is the utilisation of the HESS to improve DC bus voltage stability by reducing the load-transient recovery time and mitigating deviation magnitudes. A battery-supercapacitor HESS is implemented considering the complementary energy density and power density characteristics of the constituent storage elements. Its effectiveness in achieving the stability objective is compared with that of a battery in the same application.

Control employed for the hybrid storage converters relies mainly on the response time of the HESS elements. System net power due to load demand variation is decoupled into high and low-frequency components. Due to the difference in the control bandwidths, the supercapacitor compensates high-frequency peak variations, mainly within the first few milliseconds of a transient event, and the battery responds to slower system variations. This HESS control strategy aims to maintain a constant DC bus voltage during a generation-demand mismatch. Consequently, the battery is protected from fluctuating peak currents, improving its lifetime. Furthermore, the supercapacitor's volumetric efficiency is increased, operating within a broader voltage range and absorbing high-frequency peak fluctuations.

The simulation models used for the investigations are developed in the MATLAB and Simulink environments. In the full power system, each HESS element is connected to the DC bus via a 2-quadrant bidirectional DC/DC converter (BDC). The DC bus is then interfaced to the AC grid via 2-level voltage source converter (2L-VSC) with an LCL filter and in series with a step-up transformer. Making up the AC downstream system is a resistive load and three-phase voltage source acting as an infinite busbar. Standalone models of the DC and AC-sides of the power system are verified, where the modelling of the BDCs and 2L-VSC and their control designs are most critical. Other components of the grid are modelled as required for the simulation studies.

Comparative performance evaluations between the HESS and battery are made first in a standalone DC system model and then in a full system model (DC/AC hybrid system). The investigations and results obtained establish the advantages of implementing a full active parallel hybrid battery-supercapacitor HESS topology over single energy storage in reducing transient recovery time and magnitude of voltage deviation. It is finally established that the stability of the DC bus voltage is improved relatively by utilising a hybrid energy storage system employing an effective time-scale/frequency-based control strategy, as compared to a single energy storage unit.

Sammendrag

Den økende integreringen av fornybar energi til havs og utvidelsen av overførings- og distribusjonsnett i maritime energisystemer krever en betydelig grad av pålitelighet og systemstabilitet. Spesielt viktig vil det være å opprettholde balansen mellom etterspørsel og produksjon, til tross for kontinuerlige systemendringer grunnet diskontinuitet fra fornybare kilder og markedsvariasjoner. Energilagring vist seg å være et effektivt alternativ for å løse disse utfordringene da det tillater mer elastisitet og robusthet da det kompenserer for systemendringer ved å bevare strømbalansen.

I denne masteroppgaven undersøker jeg hvilken effekt energilagring, spesielt hybrid energilagringssystemer (HESS), har på forbedringer av det offshore strømnettets elastisitet og pålitelighet. Kraftsystemet som studeres her består av en HESS koblet til vekselstrømnettet til et offshore kraftsystem (RAPS) via en totrinns krafttransformerer. Hovedfokuset i dette prosjektet har vært å se på hvordan HESS kan brukes til å forbedre DC samleskinne spenningsstabilitet ved å redusere gjenopprettingstid og avvik. En batterisuperkondensator HESS er implementert på grunn av de komplementære energitetthet- og effekttetthetsegenskapene som er i bestanddelens lagringselementer. Resultatet av prosjektets evne til å oppnå stabilitet sammenlignes med stabiliteten av batterier utnyttet i tilsvarende bruk.

Kontrollsystemene som brukes til hybridlagringstransformerere er avhengig hovedsakelig av responstiden til HESS-elementer. Nettoeffekten av etterspørselsvariasjoner er fraskilt fra høyfrekvente og lavfrekvente komponenter. På grunn av forskjellige kontrollbåndbredder kan superkondensatoren utligne høyfrekvente toppvariasjoner i løpet av noen millisekunder, og batteriet reagerer langsommere til systemvariasjoner. Denne HESS-kontrollstrategien opprettholder en konstant likestrøms samleskinnespenning under et manglende samsvar mellom produksjon og etterspørsel. Følgelig er batteriet beskyttet mot svingende toppstrømmer, noe som forbedrer dets levetid. I tillegg er superkondensators volumetriske effektivitet forbedres og kan operere innenfor et større frekvensspekter og absorbere høyfrekvente svingninger

Simuleringsmodellen til systemet og dets komponenter er utviklet i MATLAB- og Simulink-programmene, hvor hvert HESS-element er koblet til DC-samleskinnen via en 2-kvadrant toveis DC/DC-omformer (BDC). DC-samleskinnen var deretter koblet til vekselstrømnettet via en 2-nivå-spenningskilde-omformer (2L-VSC) med et LCL-filter og i serie med en trappetransformator. En resistivt belastning og trefaset spenningskilde utgjør vekselstrømnettet i detteprosjektet. Frittstående modeller av DC-sidene og AC-sidene på kraftsystemet ble verifisert, der modelleringen av BDC-ene og 2L-VSC og deres kontrollutforming er av størst betydning. Andre komponenter i rutenettet har blitt modellert etter behov i løpet av simuleringsstudiene.

Sammenlignende ytelsesevalueringer mellom HESS og batteri gjøres først i et frittstående DC-system og full simuleringsmodell (DC / AC hybrid-system). Undersøkelsene og resultatene som ble fremsatt i dette prosjektet fastslår fordelene med å implementere en fullstendig aktiv parallell hybridbatteri-superkondensator HESS-topologi i maritim strømforsyning til å redusere flyktige gjenopprettingstid og størrelsen på spenningsavviket, fremfor å benytte seg av enkeltenergilagring. Det konkluderes derfor med at bruk av en

hybrid energilagringstopologi med en effektiv tidsskala/frekvensbasert styringsstrategi forbedrer kortvarig stabilitet av DC-busspenningen sammenlignet med utnyttelse av en enkelt energilagringsenhet.

Preface

This master's thesis project was completed in the Spring 2020 semester as part of the final requirements of my two-year international master's program: Renewable Energy in the Marine Environment (Erasmus Mundus REM). All activities related to this project are done according to the standards of the Norwegian University of Science and Technology (NTNU) and the Department of Electrical Power Engineering. The work is in collaboration with SINTEF Energy Research.

With my ambition to work in the offshore energy industry, specifically in renewable energy, this project encompasses disciplines aligned with my interests. These past six months have afforded me a chance to gain extensive knowledge about applications of energy storage technologies, topics in renewable energy integration in offshore energy systems, and power system analysis. Utilising MATLAB and Simulink for the practical aspects of this project has increased my proficiency in adeptly using the software for simulation modelling and analysis. Moreover, I believe working on this thesis project has provided me with a chance to learn more about advancements in the electrification of offshore energy systems, mainly offshore oil and gas platforms in Norway. As a conclusion to this thesis project, it is shown that the connection of energy storage improves the grid resiliency of offshore energy systems with a large share of renewables.

My first thanks go to my supervisor, Professor Elisabetta Tedeschi, for guidance me since the beginning of the project in January. Her consistent and prompt responses anytime I requested assistance in different aspects of my project are highly appreciated. I also appreciate the contributions of Salvatore D'Arco, my co-supervisor from SINTEF Energy Research. His advice on tackling the challenges I encountered during simulation modelling was constructive and facilitated my understanding of what needed to be done.

My biggest thanks go to Erick Fernando Alves, PhD employee at the Department of Electric Power Engineering. Regardless of his busy schedule, he has been of most help for most of this semester through his directions and recommendations on research papers to consult. His dedication towards helping me solve the issues I had with my simulation models proved very crucial to the progress of the project. The many hours spent meeting with me on video calls, while the university was closed due to the COVID-19 situation, certainly had a massive impact on the success of my work.

Finally, I would like to thank my family and friends for their endless motivation and support.

I look forward to starting a career in industry and competently applying all the skills I have acquired throughout my years of higher education study.

Jeffery Selorm Adorkor
Trondheim, June 2020

Table of Contents

List of Figures

List of Tables

Nomenclature

γ	State variable introduced by the PI model
ζ	Damping factor
θ	Phase angle
ρ	Damping ratio for bidirectional DC/DC converter controller
ϕ_M	Phase margin
τ	Time constant (modulus optimum)
ωb	Fundamental angular frequency
ω_d	Crossover frequency (symmetrical optimum)
ω_n	Natural frequency
ω_{ob}	Bandwidth of battery inductor current control
ω_{osc}	Bandwidth of supercapacitor inductor current control
ω_{ov}	Bandwidth of outer voltage control
Cb	Base capacitance
Cb_{dc}	DC base capacitance
C_{dc}	DC bus capacitance
e_v	Maximum allowable voltage deviation
f_b	Fundamental/base frequency
f_{sw}	Switching frequency
H_i	Inner current loop PI controller (Bidirectional DC converter)
H_v	Outer voltage loop PI controller (Bidirectional DC converter)
i_{abc}	Three-phase grid current
Ib_{grid}	Three-phase base grid-side current
Ib_{dc}	DC base current
Ib_{vsc}	Three-phase base VSC-side current
$i_{d,q}$	Direct and quadrature components of the three-phase current
K_p	Proportional gain of PI controller
K_i	Integral gain of PI controller
L_1, L_2	LCL filter inductances
L	DC bidirectional converter filter inductance
Lb	AC side base inductance
Lt_{pu}	Per unit total LCL filter inductance
ni_b	Order of reduction of switching frequency bandwidth (battery)
ni_{sc}	Order of reduction of switching frequency bandwidth (supercapacitor)
nv	Order of reduction of switching frequency bandwidth (outer voltage loop)
P	Output active power
Q	Output reactive power
R_1, R_2	LCL filter resistances
R_f	LCL filter damping resistance
R_{load}	Three-phase load resistance
Rt_{pu}	Per unit total LCL filter resistance
S	System apparent power
Sb	Base apparent power
T_a	Time delay due to converter switching
T_{eq}	Equivalent time delay of the inner control loop
T_i	Time constant of PI controller

T_{sw}	Switching period
v_{abc}	Three-phase grid voltage
V_b	Battery input voltage
Vb_{dc}	Base DC voltage
Vb_{grid}	Three-phase base grid side voltage
Vb_{vsc}	Three-phase base VSC side voltage
V_d	Boost converter rated input voltage
V_{dc}	Rated DC bus voltage
v_{dc}	Measured DC bus voltage
v_{dq}	Direct and quadrature components of AC voltage
V_o	Boost converter rated output voltage
V_r	Voltage ripple
V_{sc}	Supercapacitor input voltage
Zb	Base impedance
Zb_{dc}	Base DC impedance

List of Abbreviations

2L-VSC	Two-level voltage sourced converter
BESS	Battery energy storage system
CAES	Compressed air energy storage
CCM	Continuous conduction mode
CSC	Current sourced converter
DFIG	Doubly-fed induction generator
DG	Distributed generation
DoD	Depth-of-discharge
EC	European Commission
ES	Energy storage
ESR	Equivalent series resistance
ESS	Energy storage system
FBESS	Flow battery energy storage system
FESS	Flywheel energy storage system
FRC	Fully-rated converter
FRT	Fault ride-through
GHG	Greenhouse gas
GTG	Gas turbine generator
HES	Hybrid energy system
HESS	Hybrid energy storage system
HESS	Hydrogen-based energy storage system
HVDC	High voltage direct current
IEC	International Electrotechnical Commission
LFAC	Low-frequency AC
MCC	Microgrid central controller
MG	Microgrid
MOSFET	Metal-oxide semiconductor field-effect transistor
MPPT	Maximum power point tracking
NCS	Norwegian Continental Shelf
NSOG	North Seas offshore grid
OOGP	Offshore oil and gas platform
PCC	Point of common coupling
PHS	Pumped hydro storage
PLL	Phase-locked loop
POI	Point of interconnection
PSB	Polysulphide-bromide flow battery
PV	Photovoltaic
RAPS	Remote Area Power System
RES	Renewable energy source
RLC	Resistor-inductor-capacitor
SC	Supercapacitor
SMES	Superconducting magnetic energy storage system
SoC	State-of-charge
SPWM	Sinusoidal pulse-width modulation
TSI	Tidal stream industry
VSC	Voltage sourced converter

VRB	Vanadium redox flow battery
WTG	Wind turbine generator
ZBB	Zinc-bromide flow battery

1 Introduction

An energy system is operated and managed to maintain reliability and quality in its supply of power to consumers/loads. The nature in which offshore energy systems are set up differs from onshore energy systems primarily based on the choice of an electricity supply source and site-specific conditions (including humidity, tidal currents, waves, wind speed) in the marine environment. Power supply to offshore energy systems can be generated from local sources with isolation from the electric grid, remote supply from the onshore electric grid, or a combination of both local and grid-connected solutions. Conventionally, the designated capacity of local supply is planned and managed to match demand closely. For a typically remote supply, it is usual that the power source might be located very far from the offshore system. Considering both supply processes described above, i.e. local generation and remote supply, voltage and frequency stability are of utmost importance. The intermittency of renewable power sources poses a challenge to ensuring a stable and reliable power supply in an islanded offshore system. The effects of transients on system variables like voltage and frequency are prominent due to a weaker grid caused by the reduced inertia introduced by renewable power generators. A power quality issue common to remote offshore systems is harmonics caused by power electronics-interfaced equipment like wind turbine generators (WTG). Non-linear loads like variable speed drives, rectifiers, inverters are also common sources of harmonics. Thus, about stability, various design factors must be considered in the planning and development of a reliable offshore energy system to ensure a continuous supply of quality power to loads.

An example of an energy-intensive offshore energy system is an offshore oil and gas platform (OOGP). Fossil fuel-powered turbines are typically used in supplying power for the platform's power-intensive activities including drilling, extraction, compression, heating, among others. Power demand is, therefore, usually in a range of magnitudes higher than 30MW [1]. The burning of fossil fuels for these processes makes OOGPs a significant contributor to greenhouse gas (GHG) emissions. The alternative to reducing these emissions by establishing a connection to a remote onshore grid for supplementary supply has been proposed in many works of literature. This solution has been tested and verified to cut down on GHG emissions and reduce costs of operation of the offshore platform. However, this strategy becomes unfeasible technically and economically when the platform is located very far from shore—which is a current trend in the installation of offshore OOGPs [2]. This development has led to a heightened interest in wind power integration into OOGPs for parallel operation with on-platform fuel-powered turbine generators to provide a more cost-effective means of reducing emissions from platforms considerably. With this in perspective, the next thing to consider is the impact wind penetration has on power supply quality of a hybrid energy system (HES) of this nature. Load variations make up a large part of generation capacity on an OOGP, and with the addition of a renewable energy source such as wind, stochastic variations are expected. Hence, in the electrical design phase of an offshore energy system, power balance is a primary objective. However, system dynamics due to wind penetration, likely to influence voltage and frequency deviations in the electric grid, must be resolved.

Regarding local generation, there has been a proliferation in the integration of renewable energy sources (RES) like wind, waves, and tides into existing and new offshore energy

1

systems. Wind energy and solar energy are recognised as leading solutions in the progression towards the global objective of achieving zero-emission electrical power supply and this has influenced growth in the exploitation of these RESs offshore to meet the growing demand for electricity. Among the common RESs, wind power is highly commercialised, and Denmark is one of the leading European countries aiming to reach a 50% share in renewable energy (mainly wind) in total power generation by the end of 2020 [3].

Wind energy and other renewable sources are inherently unpredictable, and this poses a challenge for the stability maintenance of an energy system and quality of supply. Employing effective control strategies for a generation unit's converter interface is, therefore, necessary to ensure that system performance is maintained at the nominal level regardless of varying weather and grid conditions. A power system, when isolated from the grid and is electrified using renewable energy, has lower inertia and is vulnerable to disturbances. However, in grid-connected power systems, the upstream grid maintains the system frequency within the nominal region [4].

A variation in the power source or a change in demand can cause a collapse of the system when the voltage at the point of interconnection drops or rises to beyond the capacity limits of power electronic interfaces. Other issues due to the intermittency of renewable sources can be named, including frequency fluctuations, also due to low system inertia and a small time constant [5]. Reduction in power supply quality is a likely effect due to high-frequency harmonics caused by switching of interfacing power electronic components. Due to disturbances occurring in a millisecond time scale, there is a likelihood of variations in system frequency and voltage affecting reliability and continuity of supply. This situation in the long term has undesirable effects both for the power system operator and the consumer. Measures, therefore, must be taken to ensure the quality and continuity of supply even during small disturbances.

Proposed strategies to increase grid strength against power demand-mismatch include the connection of controllable distributed generators (DGs). Though feasible in increasing the grid's inertia, their slow dynamic responses become a concern in the provision of appropriate and early support to stability. Another proposal which is the connection of an energy storage device allows choosing from among several technologies with different properties to suit diverse applications. In 'net zero' energy systems of the future, discharge times spanning from one-tenth of a second to years are expected of energy storage. The capacity to provide grid support, therefore, does not depend solely on a single energy storage technology.

Energy storage (ES) plays an essential role in achieving the objective of improving grid resilience by mitigating the effects of source and load variations on system variables/quantities. The connection of energy storage devices/systems provides a means to improve the stability of systems with a high penetration of renewable power from distributed generators. In this project, battery-supercapacitor hybrid energy storage is used to provide short-duration storage services to an energy system.

1.1 Objective

This project investigates the grid support application of a hybrid energy storage system (HESS) to improve bus voltage stability during transients caused by unexpected load demand variations. Work done focuses on ensuring cooperative but independent control of outputs of two hybridised storage devices connected to the DC bus of a hybrid DC/AC power system. The HESS is used to maintain a constant DC bus voltage during a generation demand mismatch. During the event of an increase in load demand, the DC bus voltage falls below its nominal value. However, the hybrid storage discharges by supplying surplus demand to restore the voltage. Similarly, when load demand decreases, the DC bus voltage rises, and the hybrid storage charges to absorb surplus power in restoring the voltage.

The DC bus currents are shown in Figure 1.1. i_{dc}, i_c, and i_{Load} are the energy storage system (ESS) converter output current, the capacitor current, and the load current, respectively. C_{dc} is the DC bus capacitor. I_{dc} is calculated, as shown in (1.1) and (1.2) using Kirchhoff's Current Law (KCL):

$$i_{dc} = i_c + i_{Load} \tag{1.1}$$

$$i_{dc} = C_{dc}\frac{dv_{dc}}{dt} + i_{Load} \tag{1.2}$$
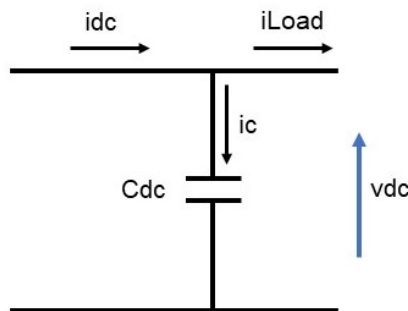
Figure 1.1: DC bus currents

A typical application where this project is relevant is an offshore remote area power system (RAPS) where connection to the onshore main utility grid is not feasible. Therefore, the offshore energy system is powered by electricity from renewable energy sources, recognisably wind energy and solar power, in parallel with the traditional gas turbine/diesel unit(s) as explained earlier.

A schematic diagram of the power system studied for this project is shown in Figure 1.2. The DC section of the grid consists of a full active hybrid energy storage unit composed of a battery and supercapacitor in parallel topology. The battery and supercapacitor have voltage capacities of 200V and 250V, respectively. They are connected to a common DC bus via individually controlled bidirectional DC/DC converters. The DC bus has a nominal voltage of 400V. The DC section described above is interfaced to the AC section of the grid via a 2-level voltage sourced converter (2L-VSC) with an AC-side voltage of 260V. Connected between the 2L-VSC and the balanced 3-phase 3kW resistive load and three-

phase voltage source (acting as an infinite busbar) is a series LCL filter to absorb high-frequency harmonics and a step-up transformer rated at 5kVA.
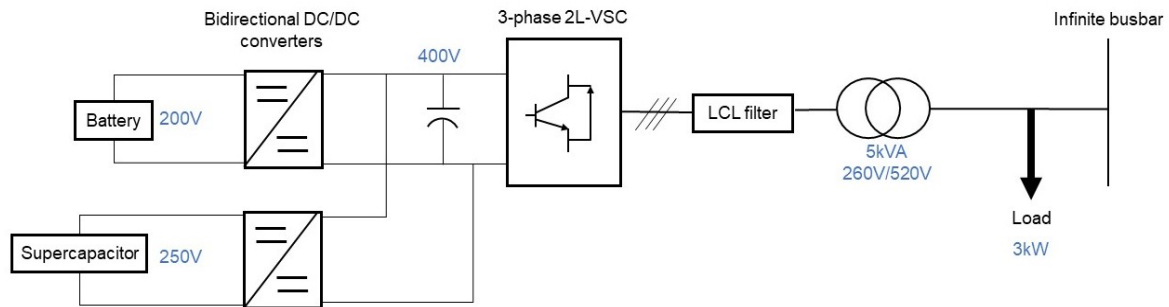
Figure 1.2: Schematic of the power system

1.2 Scope of work

The scope of this project includes a design aspect which delves into control design and implementation with an emphasis on the hybrid energy storage converters. The work covers the design, modelling, and control of a bidirectional DC/DC converter and a 3-phase inverter. Different HESS topologies are discussed, and a decision is made on which topology is simple and easy to implement, but effectively fulfils the purpose for which it is required. The choice of the most suitable storage technologies for hybridisation are discussed in this work. The modelling of the AC section of the power system, along with the control of the inverter, are discussed.

Simulation models are designed and developed using the MATLAB and Simulink software. The DC and AC section standalone models of the system are developed individually to carry out individual verifications. Standalone models of the DC section with only a battery and then with the battery-supercapacitor hybrid are developed. These models are used later in the chapter focusing on the comparative evaluations of both storage systems in improving DC bus voltage stability.

Primarily, the scope of this master's thesis encompasses selecting appropriate energy storage (ES) devices for hybridisation and implementing an effective control strategy to ensure adequate performance response in maintaining grid resiliency.

1.3 Limitation of scope

The limitations of the work done in this project are as follows:

- Firstly, validation of the designed simulation model in the laboratory is outside of the scope of this project, contrary to the initial plan to carry out experimental studies. This change in plan is as a result of the closure of the university due to the COVID-19 situation.

- The scope of the project does not cover energy storage applications in improving stability in a grid-connected system but only in remote standalone type. The design of controllers to monitor modes of connection at every point in time is therefore outside this project's scope. Inclusion of such a strategy demands designing controllers capable of facilitating a smooth transition between operating in the grid-connected mode and isolated mode

- The parallel connection of the hybrid storage to a renewable energy source such as a wind turbine or PV panel is left outside of the scope. Considering such a system would mean also designing a controller for the power source, e.g. a boost converter with maximum power point tracking (MPPT) for a PV system. Though necessary in studying how energy storage responds to changes in the primary energy source output power, it is not considered in this project

- Various energy storage applications in power systems are discussed with relevance to this work, but only voltage control support is covered in the scope of this project

- Detailed modelling of the upstream electric power system is not included in the scope. Though relevant in modelling a more sophisticated power system for advanced studies, this project focuses only on DC bus voltage stability and the downstream power system, i.e. AC load.

- The effects of inductive and capacitive loads are left outside the scope of the project. As will be seen later, the load used in the analysis is a purely resistive balanced load

- The detailed modelling of storage technologies to factor in their chemical, electrochemical, and mechanical properties is outside the scope of this work. As such, both the battery and supercapacitor are modelled as DC voltage sources in series with the DC converter inductor and its small resistance. Making an investigation of the time variation of storage properties like efficiency, heating, and lifespan can provide another sound basis for additional study, but beyond this work's scope due to time limitation

- Converter design, including effects of switching operations, is not covered. Hence, design criteria such as on-state resistance and peak switching currents of switches are computed but not implemented in the converter control design. Performance criteria such as switching losses are also not included in the modelling tasks even though mentioned briefly. This limitation goes on further to cover charging/discharging effects on degradation, temperature variation, and efficiency

- Since millisecond to second-long voltage variations are of significance for this work, only short-term energy storage technologies are considered eventually. Long-term energy storage technologies are not included in this scope since their ramp power rates give longer response times than needed for this work

- Battery State of Charge (SoC) is an important variable which is in some cases included as an input variable for converter control design. However, it is not factored

in the work scope due to the short simulation periods. It is assumed that the SoC varies within its rated value for the duration of the transients studied

1.4 Research method

The primary search engine which has been used in acquiring information from research publications and books with titles relevant to this project is Google Scholar. It provides direct links to different databases of scientific research for which NTNU students have access. Some of these databases include ScienceDirect and IEEE. Oria, which is also the online search engine for NTNU Library, was also used in getting additional articles.

The reviewed works of literature provide information on offshore energy systems; microgrids; hybrid energy storage in power system applications; energy storage technologies and their power system applications; and the design of bidirectional converters and VSCs. Various configurations of power electronic converter interfacing of hybrid energy storage to the DC grid are studied. The selected configuration is discussed in detail, and it is implemented on a practical scope in the modelling. Based on the different properties and advantages of available storage technologies in providing grid support, two ES technologies are selected based on the desired storage properties, which are discussed in detail later.

To simplify the simulation model and avoid communication errors to complicate the system, only local current controllers are used. Various conventional and proposed control methods employed in the energy management and coordination of multiple energy storages are reviewed to inform a decision on the design approach for the implemented control strategy. A trade-off between simplicity and effectiveness is employed.

1.5 Organisation of report

The report is written in MS Word, and all modelling and simulation are done in the MATLAB and Simulink environments. The MATLAB scripts and Simulink simulation models are provided in Appendices A and B, respectively. Chapters are enumerated, and sections and subsections under each chapter follow a hierarchical numbering order, i.e. 'x.y.z.' For example, Chapter 2, subchapter 3, section 3 is numbered as '2.3.3.' Equations are identified using numbers in parenthesis, i.e. (x.y) where 'x' is the chapter number, and 'y' is the position number of the equation in the list of equations within the chapter. The MATLAB scripts and figures in the Appendix are referred to often, and cited in the report with the format 'A.x,' 'B.x,' or 'C.x'. The uppercase letters represent the Appendix subsection where the script or figure is located, and the lowercase letters show the position of the script or figure in the given subsection.

All cited references can be found in 'Bibliography.' The standard of referencing used is the Institute of Electrical and Electronics Engineers (IEEE) style, and cited sources are identified as numbers in square parenthesis within the text.

This report is made up of eight main chapters, 'Introduction' inclusive, and subchapters where necessary. The Appendix makes up the last section of the report and is non-paginated. Summaries of each chapter are given below:

Chapter 2

Chapter 2 gives an overview of trends in the development of offshore power systems concerning the integration of renewable energy sources (mainly wind energy). Microgrids are briefly discussed with references to reviewed literature since isolated microgrids have many similar characteristics compared to islanded power systems. This review of microgrids gives a basic introduction upon which the subsequent chapters on subjects pertinent to islanded power systems are built.

Chapter 3

This chapter is dedicated to a review of energy storage technologies. It gives an overview of the importance of energy storage systems in power system applications according to information from reviewed literature. Different properties of energy storage technologies are compared, and the choice of technologies suitable for the project is made. The concept of hybridisation of energy storage technologies is introduced, and more details are provided on the choice of the topology to be used in the simulation model. Reasons for the choices of storage technologies and HESS topology are justified in the chapter.

Chapter 4

It describes the simulation models of the main components of the system. The models are developed on a simpler level, is possible, as compared to the detailed descriptions given in the preceding chapters. The design details are provided by referring to the MATLAB scripts and simulation model figures located in the Appendices section. The design parameters of the different models are established and explained if needed. Standalone models used in verifying the DC and AC sections of the grid are introduced, and the model of the final system is included later with necessary modifications remarked.

Chapter 5

This chapter covers a critical aspect of this master's thesis project. It discusses control design and modelling of the bidirectional DC/DC converters and the voltage source converter. The frequency-based power control approach of the bidirectional DC/DC converters is introduced here, and the process of determining the converter parameters is discussed. The control methods used for the VSC are also discussed with references to the related MATLAB script. The effectiveness of the designed converter controls is finally verified in respective standalone models before finally connecting both sections to form the full power system.

Chapter 6

This chapter presents results from simulations comparing performances of the HESS and battery in a standalone DC system and the full system. Both scenarios, as explained later, give a broader perspective of the nature of different responses expected from the energy storages in both systems. The studied cases are step increases and step decreases in load

demand for both scenarios. For each energy storage, the responses of the DC bus voltage and converter output currents are presented. An in-depth analysis of the presented results is provided to facilitate conclusions to be drawn. The results are then tabulated to give an overview of work done in the whole chapter, and conclusions are drawn based on observations made.

Chapter 7

Chapter 7 gives an overview of limitations in the design considerations and simulation modelling. Considerations or factors not included in the simulation modelling and design are discussed here. This chapter, therefore, gives an idea of what is covered or not in the master's thesis. It also gives a basis for which proposals for further work which are given in Chapter 8.

Chapter 8

The first part of this final chapter presents outlines of findings and essential information that can be gathered from all main chapters of the project report. It then summarises what was done uniquely for the project in the design, modelling and study of the power system. It adds unto the conclusions drawn from the previous chapter, and in the second part, gives proposals for further work.

2 Developments in offshore power systems

Offshore power systems for many years have been going through considerable developments and advancements aimed at creating systems capable of efficiently operating with the least impact on the environment. The prevalence of environmental conditions and the establishment of regulations and operational standards in the offshore energy sector presents new challenges for organisations operating in this industry. Innovative strategies are being continuously adapted to design offshore energy systems with the capacity to deliver reliable supply and maintain longer lifetimes of operation. In recent years, offshore projects have been in development and are expanding geographically, towards creating offshore power grids connecting countries and possibly continents.

The offshore oil and gas platform (OOGP), as explained in Chapter 1, is an offshore power system with a centralised fossil-fuel power generation and high load consumption. Traditionally, OOGPs are electrified with supply from fossil-fuel-powered gas turbines and diesel engines. On the Norwegian Continental Shelf (NCS) for instance, it is estimated that electrical power consumption from platform activities ranges from a relatively low 10MW to several hundreds of MW [6]. At the end of 2019, 87 fields were in production on the NCS [7]; this number will likely increase with further exploration findings. What this causes in effect is a gradually growing demand for electric power supply offshore to support highly energy-intensive petroleum activities. Although gas turbines of enough capacities are installed on these petroleum platforms, they are expensive to operate since they run on fuel, and they generate harmful emissions, mainly carbon dioxide (CO_2) and nitrous oxide (NO_x). According to [8], in 2018, petroleum activities in Norway generated 13.4 million tonnes of carbon dioxide equivalent (CO_2 equivalent); making up a quarter of the country's aggregate GHG emissions.

Considering this, more environmentally friendly alternatives to supply electricity offshore have been under study and research, and some are currently under implementation. Supplying power to the offshore system from an onshore grid using high-voltage subsea power transmission links is one of these measures being taken. The Troll A platform located on the NCS is the world's first OOGP supplied with power from the onshore grid via a voltage sourced converter high voltage DC (VSC-HVDC) transmission link [9]. Although this scheme has proved beneficial in reducing greenhouse gas emissions, it becomes expensive if the platform is very far from the coast. This situation demands longer transmission cables and larger equipment to provide higher transmission capacity. Offshore wind, specifically floating offshore wind turbines in deep-sea regions, has emerged as a highly feasible solution for parallel operation with gas turbine generators (GTGs). With the advent of floating wind technology applicable for deep-sea service and direct connection to platforms, it is possible to isolate the offshore platform from the onshore grid completely [10]. This initiative will help reduce emissions considerably and maximise net revenue by reducing initial costs from running GTGs continuously on fuel. An investigation carried out by [11] delves further into wind farm electrification of petroleum platforms and quantifies its advantages in improving fuel savings and reductions in emissions.

Essentially, offshore power systems are critical players in the electrification of the maritime economy, and they serve as a vital military asset [12]. Reference [12] proposes a generalised offshore power system architecture which comprises seven interconnected subsystems: power generation, power transmission, power distribution, power consumption, offshore intelligence, energy storage, and environment.

The importance of energy storage is emphasised in this architecture owing to the role it plays in dealing with the intermittency of renewable energy sources. It is, therefore, the central point of this project based on which simulation studies and analyses are carried out.

2.1 Integration of renewable energy sources into offshore power systems

With the pressure accompanying the growing rise in global energy demand, there is a motivation to invest in increasing the share of renewable energy in total electricity supply to supplement current supply and slow climate change. Efforts are being made to integrate renewable energy sources (RES) to electrify offshore energy systems.

In recent years, energy generation from sources including wind, wave, tidal, solar, and geothermal are either under research, in development, or used in commercial applications. The most commercialised among these sources is wind energy, and as of early 2019, the overall wind power capacity worldwide was 597GW with 22.1GW being offshore wind, only in Europe [13]. In 2019, a total offshore wind capacity of 3.623GW was added in Europe; representing 501 added offshore wind turbines which made up 10 wind farms [14]. Figure 2.1 shows the installed capacities of offshore wind in Europe for the past decade, indicating a higher share of growth than decline in installations within the 10 years.
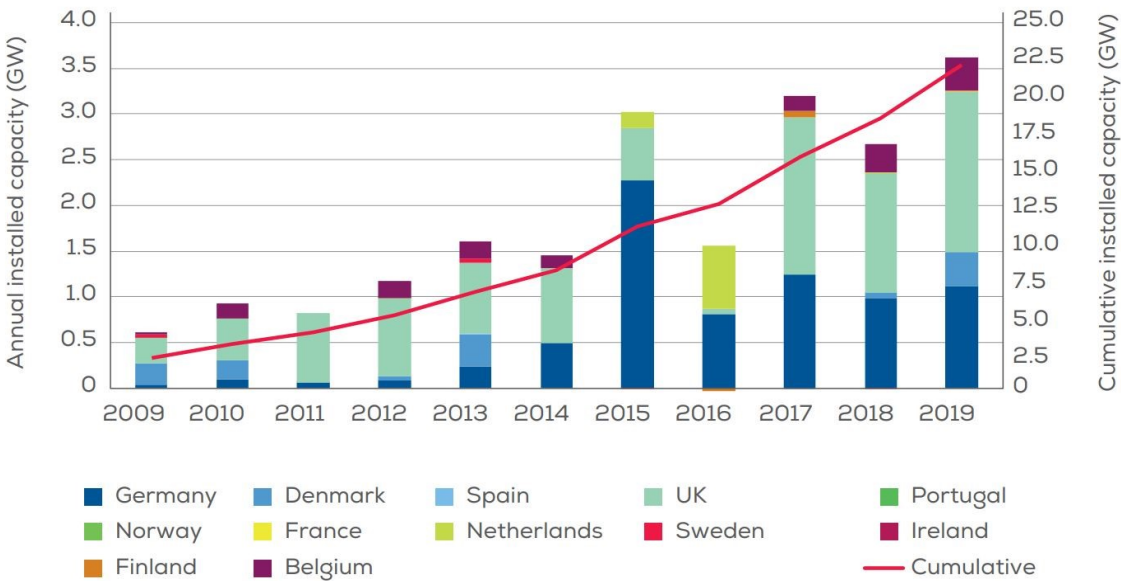

Figure 2.1: Annual offshore wind installations [14]

The European Commission (EC) expects a continent-wide increase in overall wind power capacity, both onshore and offshore, to 150GW by 2030, mainly in the North Sea region [15]. The developed wind farms are expected to be very far from shore at distances of more than 150km. This prospect has necessitated the adoption of technologically feasible offshore power transmission technologies such as high-voltage DC (HVDC) and low-frequency AC (LFAC) transmission.

Offshore wind can be considered as a derivative of onshore wind and harnessing of this energy resource is gradually moving to deep-sea regions offshore. This strategy guarantees access to a higher wind energy potential and provides an eventual substitute for fossil-fuel power when optimum commercial energy storage is available [16]. The tidal stream industry (TSI) has also started to gain some attention recently. Reference [17] estimated that as of 2018, about 20MW of demonstration and pilot projects had been deployed globally. An estimated 1600MW in projects under development were in place for operation in 2020. Offshore solar energy can be generated using photovoltaic (PV) cells and concentrating solar collectors. Solar power plants which have been investigated are made of vertically placed solar collectors arranged around the floating platforms to ensure maximum capture of solar radiation. Work done by [18] discusses some currently operational offshore solar PV plants in some countries.

Hybrid sources can also be investigated to understand the advantages of implementing synergy between complementing energy sources to smoothen and increase their combined output cost-effectively. Different energy storage devices and systems possess varying levels of technical capacity and availability. Still, with hybridisation, an improvement in their combined capabilities can be achieved while their drawbacks are compensated for, giving a smart hybrid system. Reference [19] investigates a hybrid energy scheme made up of wind and wave energy. Reference [20] also studies an alternative hybrid source made up of a PV system, compressed air storage, and hydraulic turbines.

The next widely discussed topic in the development of net-zero offshore energy systems is energy storage. Offshore energy storage, just like onshore energy storage, can be classified in terms of its energy conversion or energy storage process. With a few additional classification types, offshore energy storage can be classified as Power-to-Power and Power-to-Gas. The former refers to energy storage to be supplied as electrical power when demanded, and the latter is the consumption of electricity to produce gas for a specific purpose. The electrolyser, classified as Power-to-Gas, converts energy into hydrogen gas and stores it to be used as a final product or for power retrieval [12]. The Power-to-power classification, on the other hand, encompasses storage devices that discharge to produce electricity and is implemented for this project.

Essentially, the motivation towards further research and investigation into offshore renewable energy is to develop sustainable and cost-effective energy solutions in improving the quality of reliability of power supply.

2.1.1 Impacts of wind energy integration in offshore systems

Renewable energy generators, for example, those used in wind power production, have design properties different from those of conventional synchronous generators [21]. A

typical design in wind power generators is the presence of embedded power electronic converters. Wind energy has limited predictability and is stochastic. On account of this, wind power generators are neither dispatchable nor controllable compared to conventional generators whose 'fuel' or inputs can be easily regulated. Also, the size of generators used in wind turbines tends to be typically smaller than traditional generators.

Wind turbine technologies employed in offshore power systems are adapted from onshore wind turbines of similar design but with a few modifications to enable operation in the harsh offshore environment. The commonly known wind turbine architectures are the fixed-speed concept (Type A) and variable-speed wind turbines (Types B, C, and D) [22]. Types C and D, the doubly-fed induction generator (DFIG) with a small-scale power electronic converter rated at about 30% of the generator's capacity and the induction/synchronous generator having a 100% fully-rated converter (FRC), are widely used in offshore wind applications. The converters provide dynamic reactive power control capabilities. In many applications, the network-side converter connecting the wind turbines to the grid is a voltage source converter (VSC), which has also been used in this project in connecting the energy storage to the AC system. This converter provides independent active and reactive power control within the limit of the converter's apparent power.

Due to wind turbine design and the inherently stochastic nature of wind, integration into an existing offshore power system introduces some system disturbances. The accompanying effects on system variables like voltage and frequency on connecting a wind farm can be categorised into local and system-wide impacts. Local impacts are observed within the electrical location of a connected wind turbine or farm. Hence, an observed change can be attributed to a specific wind turbine or farm within that vicinity. It is important to note that the extent of penetration of wind in the power system does not influence this level of impact. System-wide impacts instead affect the overall system performance or behaviour. They occur due to the connection of wind power, but the scale of impact makes it impossible to attribute it to a specific wind turbine or farm [23].

Aspects of the power system which can be affected by local impacts are node voltages; fault currents, protection schemes, and switchgear ratings; and power quality (harmonic distortion and flicker). Impacts on node voltage and protection schemes affect any power system regardless of the prime mover of the generator and the coupling to the grid. Hence, they can be affected by causes also outside of wind power integration. They must, therefore, be investigated any time new generation capacity is connected. Harmonic distortion, under power quality, mainly occurs when generators are coupled to the grid through power-electronic converters. Variable-speed generators, PV systems, and small-scale combined heat and power generators connected using converters are examples of sources of harmonic distortion. Flicker occurs due to the intermittency of wind.

Further discussions of these impacts are focused on wind turbine architectures with Type C and D concepts. With a final concentration on offshore energy system applications, these two concepts are of greater relevance as regards their interfacing to the grid with power electronic converters and their variable-speed capabilities.

2.1.1.1 Local impacts

Wind turbine Type C and D architectures contribute to fault currents. The variable-speed DFIG (Type C) contributes to fault current via the control system of the power electronic converter. The control system of the coupling power electronic converter is capable of measuring quantities such as bus voltage and rotor currents at high frequencies. Due to the inherent inability of power electronic components to withstand overcurrents, the wind turbine immediately disconnects, and the crowbar protection quickly short-circuits the rotor windings of the generator. FRC wind turbines (Type D) cannot contribute to fault currents because the power electronic components cannot supply overcurrents of such magnitudes beyond their rating. The wind turbine immediately disconnects. In both cases, should the wind farm be connected to an islanded offshore power system with no grid compliance regulations requiring fault-ride through (FRT) capability, the wind turbines immediately disconnect. Primarily, the behaviour of these wind turbines depends on the type of power converter used and the design of the control system.

How a wind turbine affects node voltage depends on if it is a fixed-speed or variable-speed wind turbine. Variable-speed wind turbines (Types C and D) can theoretically affect the terminal voltage through reactive power exchange, but this is dependent on the rating and controller design of the power electronic converter. The squirrel cage induction generator in the fixed-speed wind turbine has a fixed relation between power, rotor speed, and terminal voltage; hence is incapable of exchanging reactive power with the grid. Compensating equipment like a fixed shunt-connected capacitor is fitted to compensate for reactive power consumed.

Under power quality, harmonic distortion is mostly caused by the high-frequency harmonic current generated by the power electronic interface of the mentioned variable-speed wind turbines. In large offshore energy systems with extensive cable networks, harmonic resonance and high harmonic currents due to harmonic voltages already present in the system or power electronic converters are likely to occur. However, with the recent introduction of modern advanced power electronics having high switching frequencies in the kilohertz range and with practical algorithms, harmonics are most often eliminated [23]. As will be seen later in this project, different types of filters are used in eliminating harmonics at specific frequencies.

Flicker, as stated earlier, is specific to wind turbines due to wind supply fluctuations. In variable-speed turbines, flicker does not usually occur since the wind fluctuations aren't directly translated into power fluctuations because the rotor inertia acts as an energy buffer. The power electronic interface effectively maintains the terminal voltage; hence wind fluctuations aren't experienced in the grid. However, in applications with fixed-speed wind turbines, wind fluctuations directly translate into output power fluctuations since there is no mechanical-electrical buffer present. Depending on the strength of the grid, these power fluctuations cause grid voltage fluctuations that are observed as fluctuations in the brightness of light bulbs.

2.1.1.2 System-wide impacts

According to [21], in addition to local impacts, some system-wide impacts affecting power system performance characteristics can also be observed. System frequency; reactive power and voltage; and power system dynamics and stability are some variables affected by system-wide impacts.

The contribution of wind turbines to frequency changes depends on the generator's regulation of its output power. Variable-speed wind turbines can change rotor speed based on fluctuating wind speed and are operated along the maximum power extraction curve. However, a design decision must be made to allow a margin of operation away from the maximum power extraction curve to allow for unexpected system frequency changes. That is, when a frequency drop occurs, a wind turbine should be able to supply more power to restore the frequency to nominal with enough increase margin available. Variable-speed wind turbines to be used in supplying power for offshore system applications, therefore, need to be sufficiently de-loaded to provide proper frequency control when expected.

The network voltage depends on the exchange of reactive power with the reactive inductance of the network. Variable-speed turbines are capable of reactive power exchange and can support network voltage during a power mismatch caused by a peak or dip in the wind power supply or sudden changes in load. This phenomenon again depends on the controller of the converter and the converter's rating. However, the inherent capacitive nature of the wind farm network makes it impossible to fully control voltage at the Point of Common Coupling (PCC). In many applications, reactive power support and voltage support is provided by using a Static VAr Compensator (SVC) or a Static Synchronous Compensator (STATCOM).

The impact on power system dynamics and stability due to variable-speed wind turbines in offshore applications is caused by the power electronic interface. The sensitivity of power electronic components to overcurrents may have severe consequences on a large scale. When the wind turbine disconnects due to a voltage reduction, it results in a generation-demand mismatch over a wide area of the offshore grid should the penetration of wind power be high. Incidents such as faults which result in voltage depression proportionally increase the system current, causing variable-speed wind turbines to disconnect. Hence, generation companies and transmission system operators make Low Voltage Ride Through (LVRT) a requirement to make sure wind turbines remain connected during small voltage drops for specified durations to ensure continuous operation of the grid. No international standard yet exists defining how converters are to contribute to fault currents; hence, a conventional design approach adopted is assuming that the converter contributes to fault currents and designing switchgear or protection equipment in that regard.

2.2 Overview of microgrids

As explained earlier in Chapter 1.1, it is not technically and economically feasible to connect a remote area power system (RAPS) far offshore to the main grid, and this applies to the offshore energy system under study. According to the description of a microgrid (MG) by the IEEE in [24], an MG must be capable of operating in both grid-connected and islanded

modes and act as a single controllable unit relative to a grid. According to [25], a microgrid is made up of interconnected loads and distributed energy resources having clearly defined electrical boundaries. It acts as a single controllable unit relative to the grid. The microgrid is capable of operating connected to the grid or autonomously. Basing on this definition, the offshore RAPS is in technical terms, strictly not an MG because it cannot be connected to the onshore utility grid. Nonetheless, this subsection is dedicated to giving an overview of MGs since some challenges, control strategies, and characteristics specific to the RAPS are comparable to those of an islanded MG. This subsection, therefore, gives a brief but adequate introduction of islanded MGs to give an understanding of the performance characteristics of the power system under study.

There has been a proliferation of microgrids (MGs) in modern power systems because of their many advantages, but one issue with operating them is maintaining stability and control. One other challenge is ensuring MG protection because power flow in the system now goes beyond the conventional unidirectional process [26]. Essentially, electricity demand is ever-increasing, and there is a need to ensure long-term measures in providing secure and reliable power supply. MGs implement distributed generation (DG) units among other components in improving conditions of the conventional power system. The MG has also been determined as a critical building block of the future smart grid [27] which is an organised interconnection between different MGs which exchange data, commands, and power through dedicated links.

The MG is an economically viable alternative to the expansion of already existing power transmission networks, which is both technically and economically challenging [28]. The concept of microgrids (MGs) has been a constantly evolving system technology under implementation in power systems. The MG provides the framework based on which components such as distributed generation (DG) units, energy storage systems (ESSs), and loads can be integrated into the electricity system. An MG comprises low-voltage small distributed generating units, energy storage, and loads; it is capable of transitioning to a standalone system should it disconnect from the main grid. One central aspect of the MG is the control system responsible for ensuring safe continued running of the system during connection to the traditional power grid or autonomously. The choice of controller is dependent on the connection mode and system requirements. When in connected mode, the utility grid controls voltage and frequency, and the DGs supply part or total load. During islanding, the MG controls voltage and frequency by continuously regulating the active and reactive power output. Hence, since the MG is a power generating system, it can be modelled as a DC source. This source can then be connected to the grid via a power electronic interface like a voltage source converter (VSC).

The MG can be of low or medium voltage, and its components are controllable [29]. Primarily, it can be operated in two main modes: grid-connected and islanded. With integration to the grid, MGs provide advantages such as a reduction in transmission losses, enhancement of power quality, and improvement of system efficiency [30]. MGs eliminate the need for costly transmission links from generating stations to loads through their integration into conventional distribution grids and providing direct power supply to loads. They improve system reliability since they ensure continuous power supply to loads even with the disconnection of transmission links due to faults or maintenance procedures [28]. A highly recognised advantage of integrating MGs is the facilitation of renewable energy penetration [31], [32]. In the connected mode, the grid exchanges power with and

supports in maintaining the MG's stability. In the standalone mode, the available ESSs and DGs are required to maintain the MG stability.

Regarding the urgency to fight climate change, steps are being taken to make offshore electrification cleaner and more environmentally friendly. The petroleum sector, for instance, has been a significant contributor to carbon dioxide, CO_2, and nitrous oxide, NO_x emissions. As mentioned earlier, offshore oil and gas platforms (OOGPs) with installed fossil-fuel-powered turbines, e.g. gas turbines, can be connected to the onshore grid using expensive high-voltage DC (HVDC) transmission links. However, in recent years, oil and gas platforms are being moved further offshore, so offshore transmission links are rendered technically unfeasible. This trend highlights the need for alternative means of electrifying offshore platforms by harnessing renewable energy sources like wind and wave and implementing energy storage technologies to maintain the reliability of supply.

Studies conducted for this project solely focus on energy storage applications in a standalone offshore RAPS. Focusing on applications in such a system, three main configurations of ESS can be used: hybrid, distributed and aggregated [29]. According to [29], the distributed and hybrid configurations are more advantageous than the aggregated configuration. The hybrid configuration of energy storage modelling is pursued later in this work as a strategy to improve grid resiliency further.

3 Energy storage systems

3.1 Importance of energy storage for renewable energy integration

Energy storage systems (ESSs) serve the purpose of improving grid reliability in many regards. Currently, the battery energy storage system (BESS) is the most used and a well-proven ES technology and is still under development. It is used in applications and systems including support for renewable energy sources [33], electric vehicles (EV) [34], and power system ancillary services. Under such utilisations, energy storage makes it possible to increase the penetration of renewables into power systems. References [35], [36], and [37] are a few of many publications which discuss and review suitable storage technologies for stationary applications. The main features of the storage technologies are described by [36] and [37], and [35] reviews real-world implementations of energy storage in renewable energy applications. ESSs can be used for short periods, as low as less than a minute, in smoothing power supply to a grid or for longer storage intervals for other purposes (load following and seasonal storage).

Due to the stochastic nature of many renewable energy resources, ESSs and some distributed generation (DG) units like microturbines are required in maintaining grid stability and ensuring reliable supply [38], [39]. In isolated MGs with wind energy integration, the connection of an ESS is vital to compensate for the intermittency of the wind power supply. The connected ESSs must be capable of exchanging power with the grid bidirectionally to support voltage and frequency control by maintaining variations within between acceptable ranges of deviation.

3.2 Energy storage technologies

ESSs can be classified based on the energy conversion technique they use, and these are discussed further in this section. Reference [37] describes some modes and processes by which electrical energy can be stored. These include:

1. Gravitational potential energy using water reservoirs
2. Compressed air
3. Electrochemical energy in batteries and flow batteries
4. Chemical energy in fuel cells
5. Kinetic energy in flywheels
6. Magnetic field in inductors
7. Electric field in capacitors

Some leading ES technologies which are suitable for power applications involving wind energy integration include pumped hydro storage (PHS); compressed air energy storage (CAES); battery energy storage system (BESS) which includes the lead-acid battery, nickel-cadmium (Ni-Cd) battery, sodium-sulphur battery (NaS), lithium-ion battery (Li-ion); flow battery energy storage system (FBESS) which includes zinc-bromide flow battery (ZBB), vanadium redox flow battery (VRB), polysulphide-bromide flow battery (PSB);

hydrogen-based energy storage system (HESS); flywheel energy storage system (FESS); superconducting magnetic energy storage system (SMES), supercapacitor energy storage system (SC) [40]. Figure 3.1 below shows the main categories of ESS technologies.
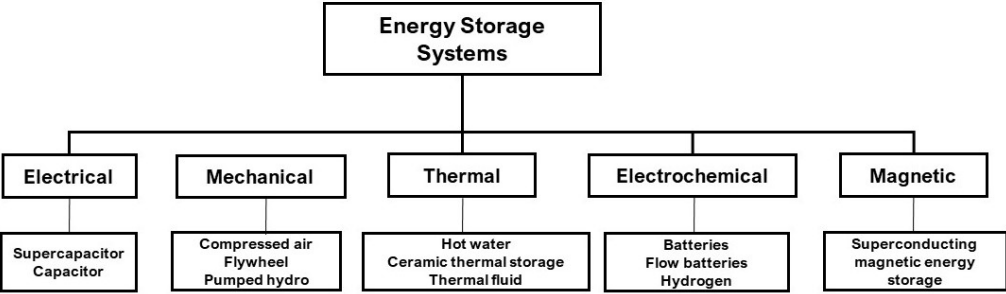

Figure 3.1: ESS categories

They can also be classified based on their times of discharge and response; this is a fundamental concept on which an essential aspect of this project is developed. Discharge time refers to the period within which a storage technology can supply its rated power, whereas response time refers to how long it takes to change its output power. Considering a pumped hydro storage system, depending on its reservoirs capacities', it can have a discharge time spanning from hours to days. Moreover, it is not capable of changing its output should there be a sudden millisecond change in load level. For periods as short as milliseconds, batteries, flywheels, and supercapacitors are better alternatives even over spinning reserves which require some time to ramp up power [41]. Based on these properties, ESSs can, therefore, be classified as short-term and long-term energy storage systems. According to this classification, energy storage applications can be categorised further into power and energy applications. Power applications are necessary for power quality improvement in the system hence are characterised by high power ratings and low energy requirements. In energy applications, the devices are used in long-duration storage suitable for energy management and mobile or stationary applications [42].

In the development of this project, energy storage suitable for either application is used: one with a high energy density and the other with a high power density. According to the descriptions of discharge and response times, it is worth noting that the response time is an important characteristic influencing the choice of energy storage technology in this work as well as in the modelling of converters. Response times between milliseconds to seconds are required since simulations carried out are to study dynamic performance during transient events. Hence, for storage modelling, short-term energy storage is the selected option for application in this project.

3.3 Applications of storage technologies

Based on the characteristic properties such as cycling capacity, energy efficiency, daily self-discharge, among others, the choice of storage technology is dependent on which application it is required for, specifically in an MG system. Descriptions of some common power system applications of energy storage are given below:

3.3.1 Fluctuation suppression

Fast fluctuations occurring within periods less than a minute have significant effects on frequency and voltage usually in standalone power systems which are characterised by lower inertia. Such occurrences affect the quality of power supply [43]. Connecting energy storage in the power system provides a means of limiting these variations within acceptable ranges. Desirable properties of an ESS for use in such an application in an offshore energy application are high ramp power rate and high cycling capability. Batteries, excluding lead-acid batteries, flow batteries, and short-period storage technologies like flywheels, supercapacitors, and SMEs are good examples of technologies possessing these capabilities [40].

A widely used solution is connecting energy storage in the DC link, between the back-to-back converters, connecting a wind turbine-driven doubly-fed induction generator to the grid, as shown in Figure 3.2 below. In a system with a wind turbine connected, the storage system is equipped with controls which can interact with the turbine's controls as well as other system controls in optimising power exchange. Reference [44] presents the case of a supercapacitor interfaced with the DC link through a DC/DC converter. It is designed with two levels of control: high-level control which is the wind farm supervisory control coordinating each generator and low-level control detailing each converters vector control. Reference [45] also proposed a combination of storage systems like batteries or flywheels in hybrid systems with offshore wind, diesel, and photovoltaic generation to mitigate fluctuations. The use of SMES to ensure fluctuation suppression is discussed where the storage devices are connected at the point of interconnection (POI) of the wind turbine generator and the network. The SMES used for this purpose is rated at several MW.
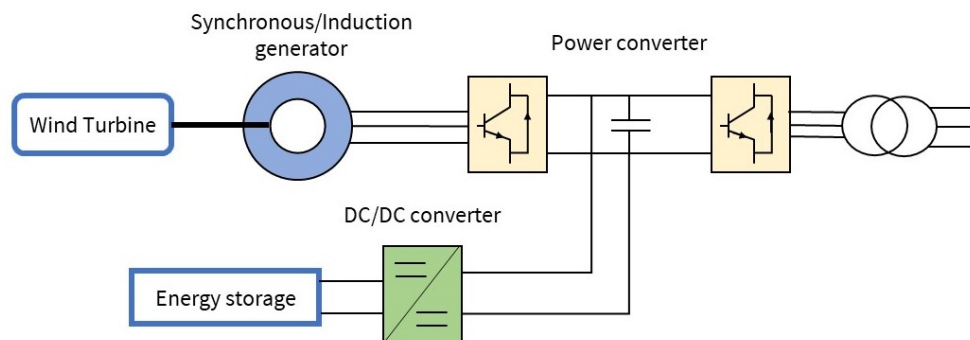
Figure 3.2: ESS connected to DC link of a back-to-back converter of wind turbine generator [44]

3.3.2 Low voltage ride-through (LVRT)

Voltage control at the PCC with an external network is required to prevent disconnection from the load(s) during voltage dips, to avoid a collapse of the system. In this regard, system standards require wind turbine generators to remain in connection to the network for specified short periods when the voltage level at the PCC drops to 0% of the nominal voltage. Since many wind turbine generators have embedded power converters which

inject reactive power into the grid to maintain the rated voltage [46], ESSs might not be required for such a purpose. Regardless, they may be necessary to protect the DC link of the converters from overvoltage. Just as in fluctuation suppression, the necessary properties for the storage systems needed are a high ramp-up rate to facilitate quick power modulation. Hence, suitable technologies are batteries, flow batteries, and small-scale storage devices like SMES, supercapacitors, and flywheels.

A study by [47] involves complementing the DC link of back-to-back converters of a wind turbine generator with a supercapacitor and carrying out simulations. Investigations showed that the voltage ride-through capability of the system is improved with energy storage support. The use of control theories is proposed in [48] where a SMES is connected to a system with a pitch-regulated fixed-speed wind turbine. The SMES is connected to the AC network through a PWM rectifier/inverter and a two-quadrant DC/DC chopper; both converters are connected through a DC link. The effectiveness of the SMES with pitch control in maintaining voltage stability during frequent fault situations is studied. The improvement of voltage stability with the connection of SMES for the facilitation of LVRT is studied in [49].

3.3.3 Voltage control support

Since reactive power control is essential in maintaining system voltage at acceptable levels, certain turbine generator types are desirable; among these are DFIGs with small-scale converters and synchronous generators connected via fully-rated converters (FRCs). This is in line with the discussion in Chapter 2 about recommended turbine architectures in offshore energy applications. The converters embedded in these generators are capable of reactive power control, and in effect voltage control, at the point of connection. Once again, the inclusion of energy storage voltage support improves the dynamics of voltage control. Batteries, flow batteries and short-scale storage systems are also recommended for this purpose based on their high ramp power rates [40].

Reference [50] discusses the coupling of a Distribution Static Synchronous Compensator (DSTATCOM) to a flywheel in the control and maintaining of voltage stability. The ESS supports the DC-link of the DSTATCOM and provides the capability of exchanging active and reactive power. Reference [51] studies the coupling of a STATCOM/BESS combination to a self-excited generator to control reactive power, eliminating harmonic currents, and compensating for load changes within an isolated system.

One main observation is that active power control is dependent on the type of storage technology used. A study carried out by [52] shows that the SMES is a perfect alternative acting within a 16.6ms response time in the step input of both active and reactive power.

3.3.4 Oscillation damping

With high penetration of wind, a grid's stability against disturbances may be compromised. In this regard, wind power plants are required by grid codes to support the grid in

maintaining synchronism during the disturbances. Wind power plants achieve this by the exchange of active power with the grid at frequencies between 0.5 and 1Hz [53].

Since many energy storage technologies are suitable for this application by injecting/absorbing active power within a minute, a high ramp rate is once again needed. Batteries, flow batteries, and short time-scale energy storage are recommended technologies. Modal and frequency domain analyses are used in the study of system stability aspects. Reference [54] proposes the use of a flywheel to eliminate low-frequency oscillations by optimally locating the storage device in a multimachine system.

System changes under consideration are caused by events such as wind gusts, fluctuations in wind supply, short circuits, and local load disruptions. References [55] and [56] investigate the capacity of SMES to manage the exchange of large quantities of active and reactive power. Wind generators with this storage technology are expected to provide oscillation damping. It is worth noting that the consideration of system uncertainties ensures that proper control can be implemented as can be seen in [56]. Here, robust non-linear control of a SMES is proposed in a wind-based network, having oscillating power flow, with an additional power disturbance. It is finally concluded that using batteries and SMES in system damping oscillation control to control variations due to power system disturbances, by managing active and reactive power exchange, is more robust and effective.

3.3.5 Spinning reserve

As defined by [57], spinning reserve refers to excess available power from online generation capacity above the quantity required to supply a given load. It serves as a standby to supply sudden increases in load or losses of generators. Secondary and tertiary reserves which can also be activated based on the operator's discretion are referred to as spinning reserves as well. Storage technologies suitable for this application include SMES, flywheels, BESS, flow batteries, HESS, and CAES. Primarily, batteries and flow batteries have been technologies under consideration for this application.

Standalone power systems benefit the most from the use of storage systems as spinning reserves based on studies by [58]. To use a BESS for spinning reserve purposes with maximum economic benefit, management and optimal sizing are the main factors of consideration. Reference [59] carries out a study of providing spinning reserve to a 30.6MW wind power plant using a 6MW to 6MWh VRB. Also, many works of literature have focused on the use of flow batteries for this application. This technology's short response time and capacity to be overloaded makes it the right candidate. It, therefore, becomes a preferred choice compared to other options like fossil-fuelled power plants [60]. With the implementation of spinning reserve, it can be concluded that wind power fluctuations within thirty minutes are reduced by a factor of 3.

3.3.6 Load following

ESSs are needed to provide energy from a period of minutes to almost 10 hours [61]. This application is once again needed to compensate for the stochastic nature of wind, making it unable to match with power demand always. One significant effect of this occurrence, voltage and frequency variations, make the integration of wind into conventional power systems quite a challenge. In terms of economic challenges, wind power generators suffer penalties when their generation does not satisfy the terms of their agreement. Hence, ES plays a vital role in ensuring these technical and economic challenges are met by storing and supplying electrical power for long hours. Storage technologies like batteries, flow batteries, CAES, and PHS are well suited for this application.

A relevant example of the use of a battery being used for this application is a wind power system in Futumata, Japan, where a 34MW sodium sulphide (NaS) battery bank is implemented to flatten energy production from a 51MW wind power plant [62]. Proper management is a measure not only adopted to ensure energy supply is always available but to maintain an economical operation of the battery system. Regarding this, [63] develops a control algorithm capable of reducing storage during hours when demand is very high to ensure economy. This goal is accomplished to enhance the profit of the system since the market price of energy during these hours is high. It is concluded that with proper control of batteries, the predictability of wind power plants is improved and accompanying costs from integration are reduced. That is, precision in matching output at any time with the forecast is achieved. Based on a study by [64], 34MW, 40MWh of storage capacity are required properties to improve the forecasted output of a 100MW wind power plant (34% of the rated capacity) and allowing tolerance of about 4% per unit. Based on many works of literature, hydrogen-based ESSs are an excellent alternative for load-following applications. Demo projects have been developed in work done by [65] and [66] to study stand-alone systems comprising wind, photovoltaic generation and hydrogen storage. These projects develop management algorithms which use excess energy to produce hydrogen in an electrolyser, supplying this hydrogen to fuel cells to produce energy when needed. A study of such isolated systems with hydrogen energy storage shows that they are technically feasible.

Other applications of ESSs in power grids with renewable energy penetration, specifically wind energy, include peak shaving, transmission curtailment, time-shifting, unit commitment, and seasonal storage.

3.4 Comparison of technical and operational parameters

It can be inferred from the review of energy storage applications so far that for applications requiring early response with high ramp-up rates, some technologies are more advantageous than others. Outstanding among these are BESS, SMES, and flywheels.

Table 3.1 below from [29] details characteristics of some selected energy storage technologies, including the three alternatives mentioned above, commonly used in diverse power system applications. The following diagram in Figure 3.3 maps energy storage to

some power system applications described previously in this chapter referencing information from [67].

Technology	Energy density (Wh/kg)	Power density	Response time	Self-discharge (per day)	Lifetime (year)	Overall efficiency
SCESS	0.1-5	800-23,500	ms-10min	20-40%	5-8	0.85-0.98
Nickle BESS	100-140	50-1000	4h	0.2-0.6%	10-20	0.60-0.73
Li-ion	160-200	150-315	15m-hours	0.1-0.3%	5-15	Up to 0.97
CAESS	-	-	1-24h	Small	20-40	0.70-0.90
FESS	5-100	1000	ms-15min	Small	15-20	0.93-0.95
SMES	0.5-5	500-2000	ms-8m	10-15%	15-20	0.95-0.98
PHES	-	-	1-24h	Negligible	50-60	0.70-0.82

Table 3.1: Comparison of energy storage technologies [29]

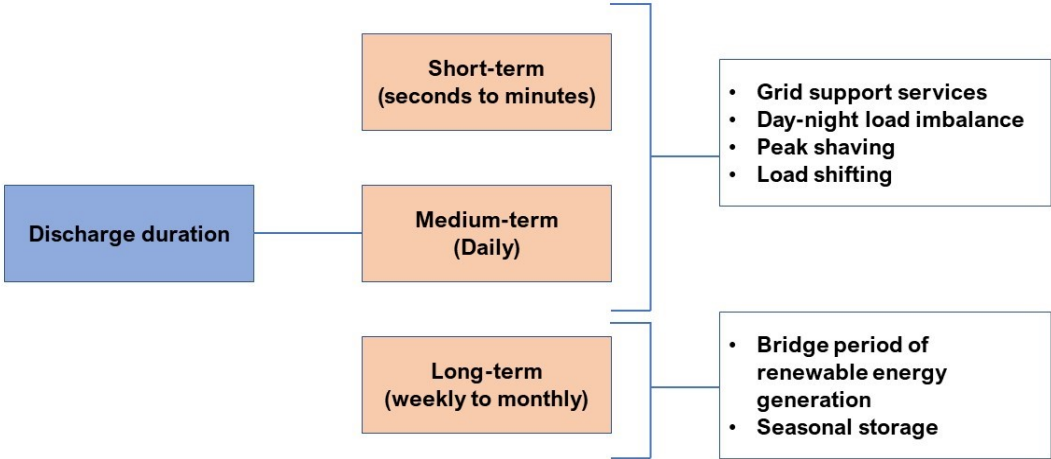**Figure 3.3: Mapping of storage technologies to power system applications based on discharge duration**

For this project, minimum discharge duration, i.e. short-term, is required for providing grid support. It can be inferred from Chapter 3.3 that required characteristics of energy storage relevant for employment in short-term applications are energy density, power density, lifetime, and ramp power rate [29].

According to Table 3.1 above, the supercapacitor has a very high power density (800-23,500), making it capable of responding in the millisecond time scale. Its energy density, however, is low. The lithium-ion battery (Li-ion) on the other hand, has the highest energy density of 160-200Wh/kg compared to the other widely used technologies. As expected, its power density is relatively very low, resulting in response periods within hours. These two storage technologies can be described to have 'the best of both worlds' making them suitable components for the type of study to be carried out. They also have sufficiently high efficiencies enough for the nature of the application for which they're required.

To further support the decision of using a lithium-ion battery and supercapacitor to constitute the hybrid storage unit, Figure 3.4 from [40] shows the response times of the two technologies. The regions emphasised by the squares are with regards to the fact that low capacities in MW (on the horizontal axis) of the devices are required considering the length of time for which they are to operate within an operational period, i.e. within milliseconds. The graph also shows the energy densities of these technologies, with a scale the left vertical axis. Therefore, the final choice for the HESS constituents is the Lithium-ion battery and a supercapacitor.
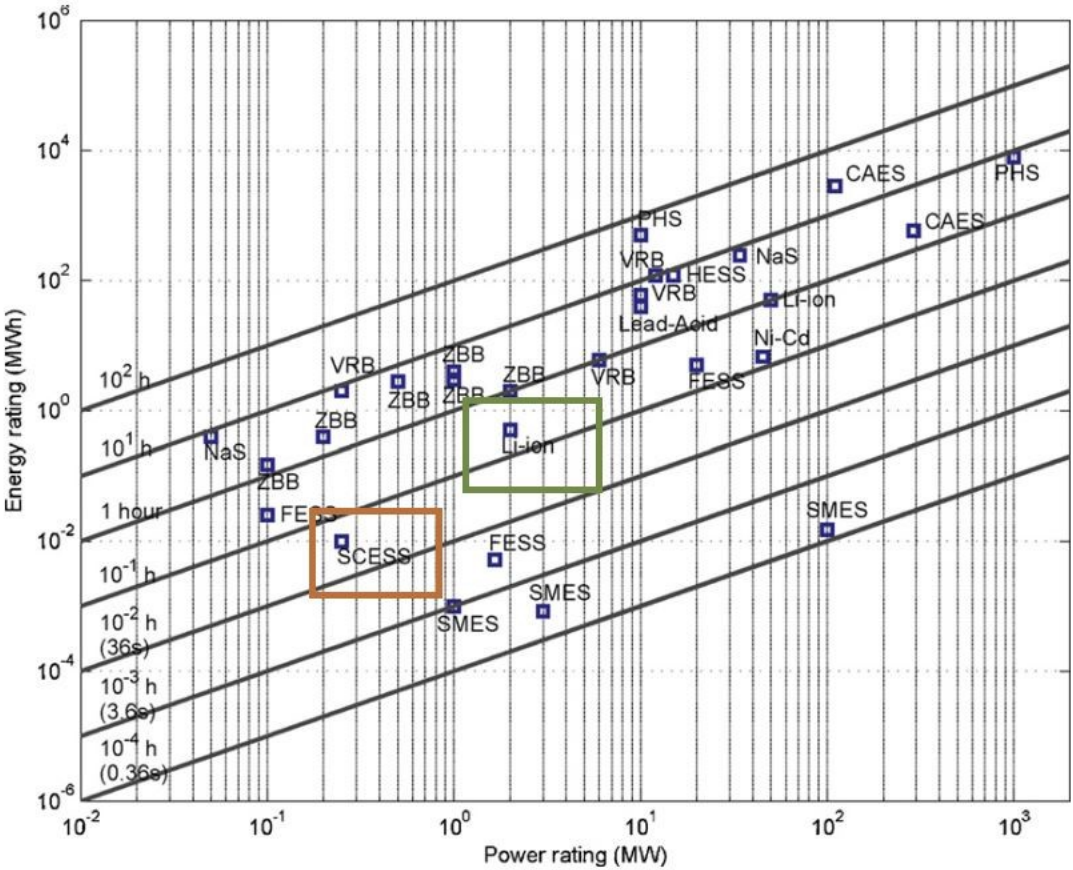
Figure 3.4: Discharge times at low rated power [40]

3.5 Hybrid energy storage

Installation of energy storage in an islanded power system is accomplished using any of three known general configurations: aggregated, distributed, and hybrid [29]. In the aggregated configuration, the ESSs are installed on the same bus to facilitate energy storage modelling. In the distributed configuration, the ESSs are dispersed to various locations within the power system. Finally, the hybrid configuration combines different ES technologies to create a single unit which delivers all required characteristics at sufficient levels. These configurations are illustrated in [29] and shown in Figure 3.5 below.

Research works have shown that the hybrid and distributed configurations are more preferred compared to the aggregated configuration in terms of efficiency. As regards this master's thesis, the hybrid configuration is used to model energy storage to be used for comparative analysis in the power system.

Figure 3.5: a) Aggregated, b) Distributed, and c) Hybrid configurations of energy storage [29]

Based on earlier discussions in this chapter, single energy storage is incapable of providing all the characteristics needed for different power system applications. This observation has necessitated the combination of ES devices having characteristics more favourable than ot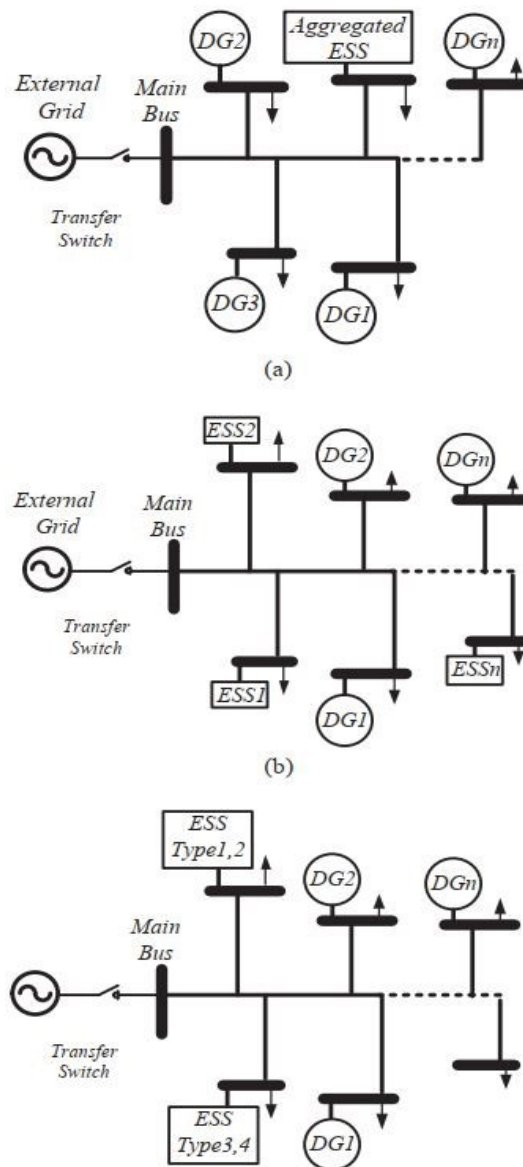hers to give a whole complete storage system, and this is known as hybridisation. A hybrid energy storage system (HESS) is an integration of different ES technologies such that they complement each other's properties resulting in a storage system with improved characteristics.

In research publications like [68] and [69], the HESS has been used in the operation and control of MGs. Work done by [70] implements a supercapacitor and a battery to bring an improvement in the power-sharing strategy employed in a DC MG. Load variations in the DC MG are translated into voltage variations. References [71] and [72] propose a droop control strategy for power-sharing between a SMES and a BESS. With many ES devices having DC terminal voltages, some other works have considered a connection of the HESS to the DC bus. In [73], hybrid storage comprising a flywheel and battery is used in an autonomous MG for frequency regulation. Between the DC bus and MG AC bus is a DC/AC converter. This converter works both as a rectifier or inverter depending on the nature of operation required. For the rectifier mode, power flows from the MG to the HESS, and the constituent storage devices are charged. During the inverter operation mode, power flows from the HESS to MG during the discharge of the storage devices.

Now focusing on the storage technologies which have been selected for the project, the Li-ion battery (referred to from now on as battery) exhibits a relatively slower response compared to the supercapacitor's response. A time-scale or frequency-based approach based on response time is used in the control scheme of their interfacing converters. The HESS's two storage elements are expected to operate within two separate bandwidths due to their different response times. The supercapacitor responds within the first few milliseconds of a deviation, and the battery responds after. This strategy ensures timely regulation of the DC bus voltage, which is the system variable of focus. Balancing power is therefore available to restore the bus voltage to its nominal value after a generator-demand mismatch. Determination of the frequencies of response and the details of modelling are given in the next chapters.

To simply explain power-sharing based on frequency ranges, consider hybrid storage comprising two storage devices having assumed shortest response times of 1 second and 1 minute. These reciprocate to frequencies of 1Hz and 0.01667Hz, respectively. If a sample rate of 1 sample/second is used in filtering the signal, based on the Nyquist-Shannon sampling theorem, a Nyquist frequency of 0.5Hz (1/2 of sample rate) is obtained. This process gives a limited frequency range of [0, 0.5] Hz within which both energy storage devices must operate. Figure 3.6 shows the frequency bands covered by each ES where the device with a longer response time acts in the lower frequency range of [0, 0.0167] Hz whereas that with the shorter response time responds at [0.0167, 0.5] Hz.

Considering the storage device with quicker response time, for example, when there is a change in a system variable, say voltage, power components between 0Hz and 0.0167Hz are attenuated, and power components between 0.0167Hz and 0.5Hz are sent to the storage element.
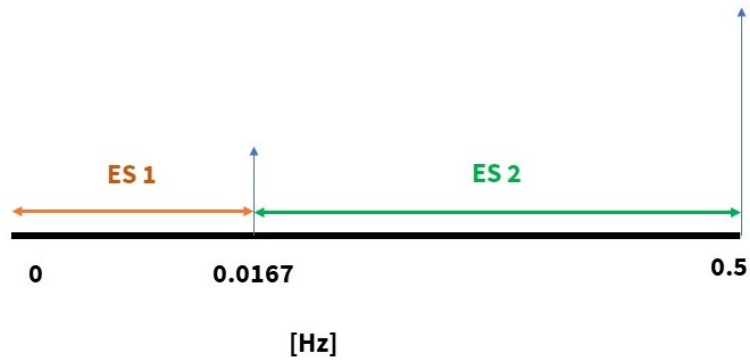
Figure 3.6: Frequency ranges of operation

It can be concluded that power-sharing between the constituent storage devices can be both power and frequency-based to provide better grid support of the energy system during transient and steady-state periods. It must be noted that the choice of bandwidths designated to storage devices as well as other design factors are dependent on the nature of application and stability requirements. These are discussed in detail later.

According to [74], the main battery-supercapacitor HESS topology classifications are passive, semi-active, and full active, as illustrated in Figure 3.7.
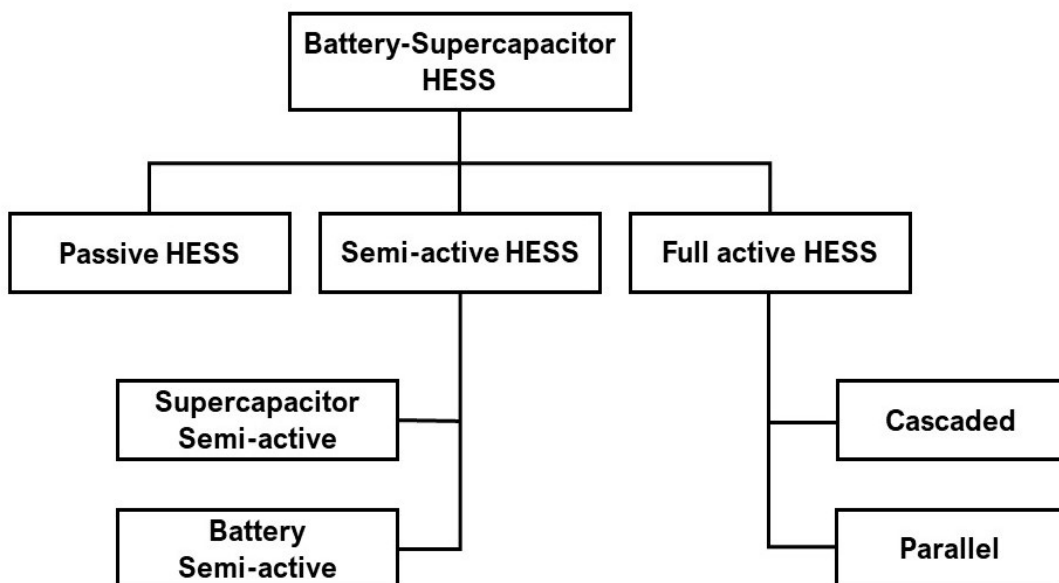
Figure 3.7: Classifications of battery-supercapacitor HESS topologies [74]

The next step in the project development is selecting a suitable battery-supercapacitor HESS connection topology. In connecting hybrid storage to the power system, the ESS elements can be either coupled to the AC or the DC bus. In a standalone system such as that considered for this project, connecting them to a DC bus is considered a better alternative. Firstly, many renewable energy generators and energy storage devices have

27

DC terminal voltages. It is, therefore, a more viable option to connect these components to the DC bus, eliminating the need for many requirements in designing the power converter. Moreover, a DC system does not require synchronisation of controls, and this reduces the complexity of the entire system [75]. In summary, coupling to the DC bus is more straightforward, more effective, and costs less to establish than coupling to the AC bus.

The connection topologies to choose from for the battery-supercapacitor hybrid storage system to be implemented are given in Figures 3.8, 3.9, and 3.10 [74]. The battery-supercapacitor HESS topologies are briefly discussed after.
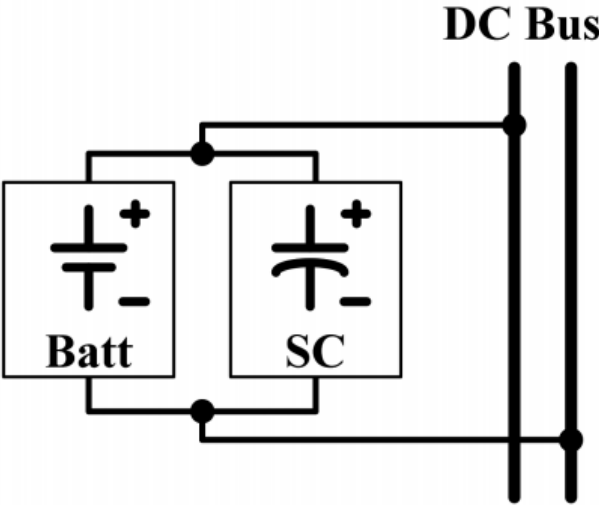
Figure 3.8: Passive HESS topology [74]

(a)   (b)
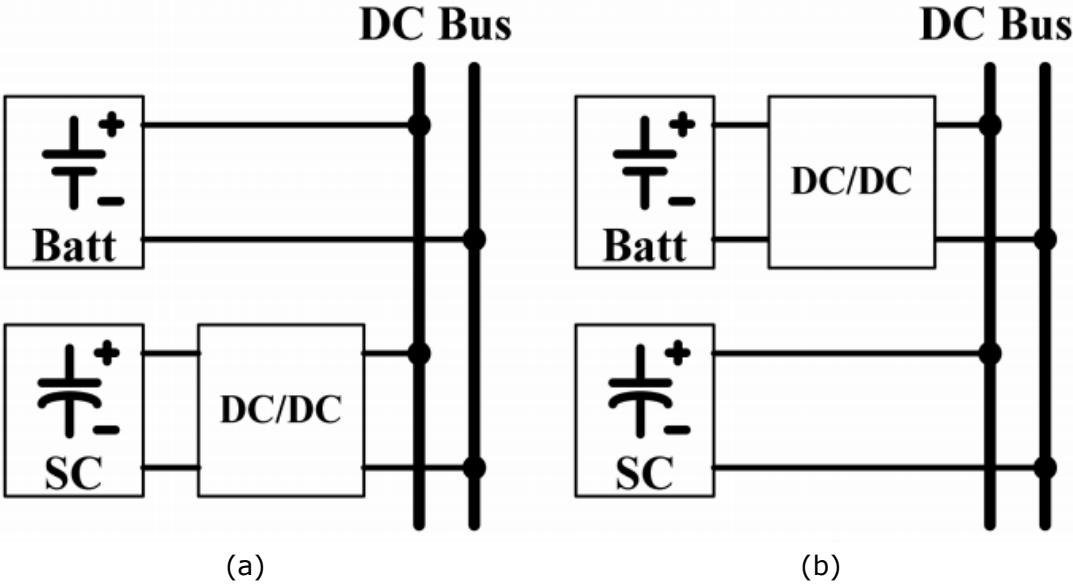
Figure 3.9: Semi-active HESS topology (a) Supercapacitor semi-active HESS topology and (b) Battery semi-active HESS topology [74]
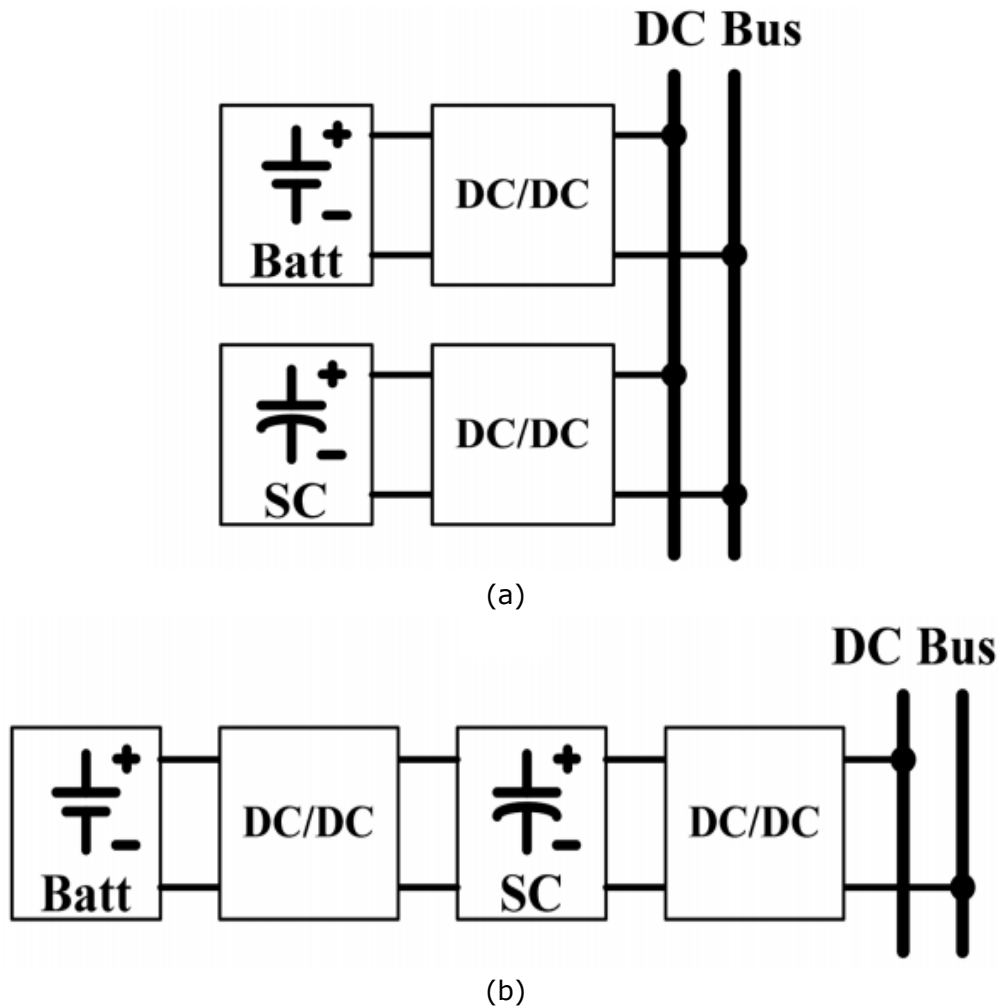
Figure 3.10: Full active HESS topology (a) Parallel active HESS topology (b) Cascaded active HESS topology [74]

3.5.1 Passive HESS

The passive connection of a battery and supercapacitor is the cheapest and simplest topology among the three. It effectively mitigates transients due to pulses in loads, increases the peak power delivered, and eliminates losses due to the use of power converters [76] and [77]. In Figure 3.8, the battery and supercapacitor are connected directly to the DC bus with no interfacing component. Both storage devices share a common terminal voltage which is dependent on the charge and discharge characteristics of the battery and its state-of-charge (SoC). In smaller MG applications, the battery is sized to a capacity capable of supplying for up to five days with no need for an external source of power [78]. The battery, therefore, cycles with a low depth-of-discharge (DoD) and a relatively slow C-rate during charging and discharging. As a result of such a design decision, DC bus fluctuations are minimal; hence, DC bus voltage is kept almost stable.

However, the internal resistances of each storage device influence the process of system current injection and absorption [79]. As such, the supercapacitor's ability to handle

transients is not fully utilised. Also, with the sizing of the battery improving the terminal voltage, the supercapacitor is not used to its full SoC range, giving poor volumetric efficiency [80].

3.5.2 Semi-active HESS

Improving upon the performance of the passive HESS topology, a power electronic converter is used to interface the ESS to the DC bus, giving the semi-active HESS topology. Power flow is actively controlled for this topology [81]. Only one of the hybrid storage elements is actively controlled. Figure 3.9 (a) shows a semi-active topology where the supercapacitor is interfaced to the bus using a DC/DC converter. This is known as the supercapacitor semi-active topology. The battery is directly connected to the bus. The DC/DC converter ensures isolation of the supercapacitor from the DC bus and the battery terminal. Volumetric efficiency is ensured because the supercapacitor acts within a wide range of voltages. With ample battery capacity of the directly connected battery, a stable DC bus voltage is also ensured [82]. However, the passive connection of the battery exposes it to fluctuating high currents which are detrimental to the battery's lifespan [83].

In the other semi-active topology, the battery semi-active topology in Figure 3.9 (b), the battery is isolated from the DC bus and supercapacitor by a DC/DC converter [84]. Compared to the passive and semiconductor semi-active topologies, this topology allows proper control of the battery current regardless of fluctuating load demand. The battery's terminal voltage is not necessarily expected to match the DC bus voltage, and as such, it can be flexibly and adequately sized and configured [85]. The supercapacitor, being passively connected has low volumetric efficiency. Moreover, the linear charge and discharge process of the supercapacitor likely causes fluctuations in the DC bus resulting in instability and reduction in power quality of supply. In avoiding these effects, the supercapacitor capacity must be made extremely large, and this incurs a higher cost.

3.5.3 Full active HESS

In this topology, power flows of both the battery and supercapacitor are controlled via DC/DC converters. This topology allows flexibility in operation, enhances the overall performance of the system, and increases the cycle life of the storage elements [83]. The two commonly known full active topologies are the parallel and cascaded topologies, shown in Figure 3.10 above.

As can be seen in Figure 3.10 (a), both the battery and supercapacitor are isolated from the DC bus by power converters in the parallel full active topology. The parallel HESS is mostly used in grid-scale storage applications allowing control of both storage elements [86]. A properly designed control strategy guarantees improved performance, increased battery life, and better DC bus voltage stability [87]. Decoupling of both devices increases the range of SoC for both and in effect improves the volumetric efficiency of HESS.

In the cascaded topology, shown in Figure 3.10 (b), the battery and supercapacitor are connected in cascade to isolate them from the DC bus. The bidirectional DC/DC converter isolating the battery is usually current controlled to give smoother regulation of the battery exchange. In effect, the battery is protected from extreme charge and discharge events caused by variations in renewable sources or load demand. The DC/DC converter for the supercapacitor is, on the other hand, typically voltage-controlled for DC bus voltage regulation and absorption of high-frequency power exchanges [88]. Since the capacitor now has a broader range of operating voltage, higher voltage swings between the supercapacitor and DC bus are expected. This phenomenon results in more losses in the DC/DC converter due to the inability to maintain efficiency within such a broad range of voltages [89]. The use of two power converters reduces the coulombic efficiency of the HESS as a result of losses in the power converters. Finally, the overall performance of the full active topology is dependent on the reliability of the converters and the control system.

In summary, the objective of this project is to implement a HESS control strategy to increase the resiliency of the grid against voltage deviation and reduce the transient recovery period. This implies that keeping DC bus voltage stable is only a part of the solution. It is desired to implement a HESS topology capable of maintaining DC bus voltage stability to the highest level possible for regular operation. This way, overall system stability is maintained, and the power supply to the load is as reliable as possible.

Considering the HESS topologies discussed so far, it is understandable to eliminate the passive topology as a possible option to use for this project because no control whatsoever applies to the ESS elements. Between the semi-active and active topologies, control is at least applied at a point during power exchange of the HESS. The full active topology, though more complex than the semi-active topology, affords better performance since it gives complete isolation from the DC bus. The battery is protected from high current fluctuations in the DC bus hence improving its useful life, and the DC bus transient voltage stability is improved with the supercapacitor having a broader range of voltages to act. The semi-active topology is a more suitable option when there are possibly more converters in other sections of the power system making coordinated control complex. Hence, in modelling the HESS converters for this project, the HESS full active parallel topology is used. This design decision gives a model appropriate for investigations to be carried out.

4 System modelling

In this chapter, the modelling and design of standalone simulation models of the DC and AC sections of the grid are detailed. These models are then verified to determine that they respond as expected before they are connected to form the full hybrid power system. The simulation models are developed in Simulink, and the relevant parameters computed using the MATLAB scripts provided in Appendix A. Blocks from the 'Simscape Electrical' library are used in modelling the system components.

The DC section comprises a hybrid energy storage system made up of two storage elements. The battery and supercapacitor models used are not technology-specific since a DC voltage source suffices to carry out the required study. The AC section is modelled without much complexity: a balanced three-phase resistive load and a 3-phase AC source (an infinite busbar) make up the downstream grid of the AC section of the power system. This model can be further developed to include components including other fixed loads and flexible loads, a transmission system, additional three-phase sources, gas turbine generator(s), among others. Interfacing the DC bus to the AC section is a 2-level voltage source converter (2L-VSC). Between the converter and the load are a series LCL filter and a step-up transformer.

Analyses carried out using this system show how energy storage mitigates the effects of load demand change on DC bus voltage transient recovery time and magnitude of deviation. Specific component details like switching losses and internal resistances do not contribute to a large extent to the nature of studies carried out here; hence, average models are used for the converters.

As explained in Chapter 3, the desired characteristics inform the decision to select specific ES technologies for different power system applications. In this regard, for this project which focuses on the provision of grid voltage support for an islanded system during load demand changes, response time characteristic is the storage technology required.

Depending on their purpose in a microgrid application, power converters are categorised into grid-feeding, grid-supporting, and grid-forming converters [90]. The grid-feeding converter is controlled as a current source; hence it needs the grid voltage to be formed by either a generator or a power converter before it can operate. In that case, it cannot be operated independently when in islanded mode. The grid-forming converter, on the other hand, can operate in the islanded mode because the AC voltage of the main grid is traditionally formed by synchronous generators. The grid-supporting power converter is an intermediate between the grid-feeding and grid-forming power converters. For an AC grid, it supplies required amounts of active and reactive power to the grid to regulate system frequency and voltage respectively within their range of rated values. It requires a grid former when operated as a current source. However, when controlled as a voltage source connected through an impedance, it can operate in both grid-connected and islanded modes [90]. A typical example of a grid-forming converter is a UPS system which remains offline from the grid when operating conditions are normal. When there is a failure in the grid, the converter forms the grid voltage and this voltage becomes the reference for connected grid-feeding converters. Majority of converters connected in DG systems like PV

and wind turbine generators are grid-feeding. The 2L-VSC used in this project is operating as a grid-supporting converter.

4.1 DC system

A schematic of the DC standalone system is given below where the DC grid is made up of the DC bus capacitor and a controlled current source representing load demand. The Simulink simulation model of this system can be found in Figure B.1.
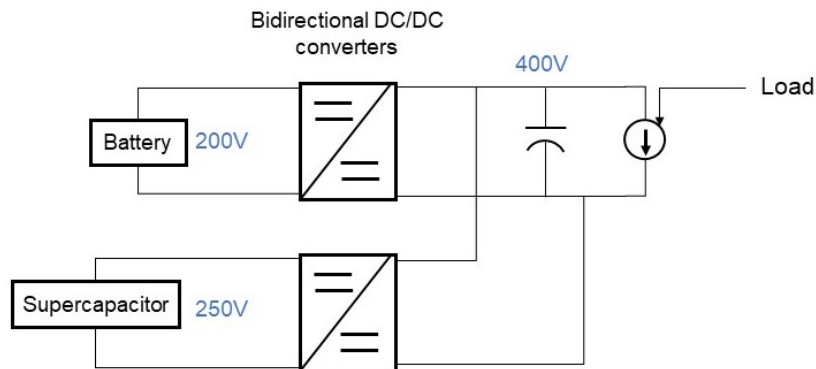

Figure 4.1: Schematic of the standalone DC system

4.1.1 Battery and supercapacitor

At this point in the project development, decisions have been made regarding the type of energy storage technologies to constitute the HESS: A lithium-ion (Li-ion) battery and a supercapacitor. This decision affords an ideal HESS which provides high energy and high power characteristics to handle source variations and load demand changes. Also, an effective HESS topology appropriate to accomplish the objective of improving DC bus voltage stability, with full converter current control, has been selected. With the parallel full active topology, the elements of the HESS model are connected in parallel with corresponding interfacing bidirectional converters isolating them from the DC bus.

The next step of the project involves the determination of parameters for modelling the standalone DC section of the power system to design and verify the control strategy of the HESS. Modelling of the AC system components, specifically the 2L-VSC and the LCL filter, is covered in this chapter as well.

With the battery and supercapacitor being DC voltage sources, the main parameters characterising them are their terminal voltages. Voltage parameter values for the DC bus, battery, and supercapacitor are designated in descending order of magnitude, i.e. $V_{ref} > V_{sc} > V_b$ as a matter of choice since the supercapacitor is required to respond to peak variations in DC bus voltage during system events. The battery supplies most of the load during steady-state operation of the system. The parameters of the battery and supercapacitor used in the modelling are detailed in the following subchapters.

4.1.1.1 Battery

Many literary works have proposed different battery models for various research purposes. Though the decision is to use a DC voltage source for this project, a brief description of a commonly used model given in [91], [92], and [93], shown in Figure 4.2 is given. In case the reader wishes to use a more technology-specific model of a battery; this model suffices as a suitable alternative.

Equation (4.1) expresses the relation between the battery voltage, terminal voltage, charge and charging/discharging current, and internal resistance ($v_{batt}, V_{emf}, i_{batt}, and\ R_1$ respectively) and a parallel RC circuit defining charge transfer and diffusion within electrolyte and electrode [91], [93].

$$v_b = V_{emf} - I_b * \left(R_1 + \frac{R_2}{1 + C_b * R_2 * s} \right)$$
(4.1)

In (4.2), an expression giving battery SoC as a function of initial SoC, battery capacity, and current (SoC_o, A_{batT}, and I_{batt}) is presented.

$$SoC = SoC_o + \frac{1}{3600 * A_{batt}} \int I_{batt} dt$$
(4.2)
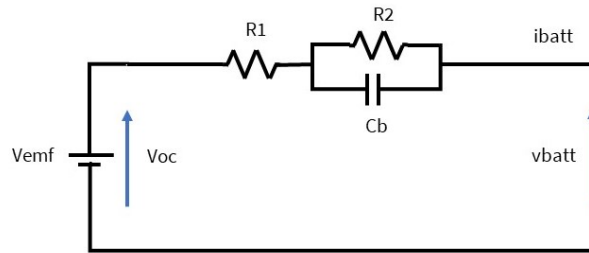
Figure 4.2: Battery model for further analysis [87]

4.1.1.2 Supercapacitor

Just like the battery, a DC voltage source is used as a simulation model for the supercapacitor. Should a more technology-specific model be required, the model proposed by [92] is a good alternative. The supercapacitor current i_{sc} is an input, and it limits supercapacitor operation between high and low voltage limits, i.e. safe operation. The three parameters making up the model are the capacitance, equivalent series resistance representative of charging and discharging resistance, and a parallel resistance representative of self-discharge losses (C_{sc}, Rs_{cs}, and Rs_{cp}). Voltage v_{sc} over C_{sc} is the open-circuit voltage.

The model is presented below:

34
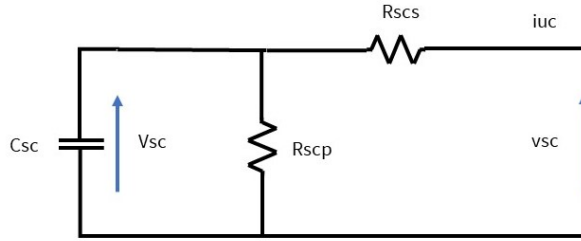
Figure 4.3: Supercapacitor model for further analysis [87]

4.1.2 Bidirectional DC/DC converter

This subchapter details the modelling and design of the bidirectional DC/DC converter (BDC). With a few initial parameters available, the remaining parameters are determined, and some characteristic effects of the converter passive components (including switches and diodes) are computed. The purpose of the detailed design of the converter's passive components is to improve converter efficiency as much as possible. The selected switching frequency (f_{sw}) for the BDC is 10kHz, and it is with this frequency that the component values are calculated. A brief introduction to converter interface technologies is given after which the selected topology is introduced.

Primarily, the power electronic converter interface isolates the energy storage device from the DC bus and provides controllability of output. Converter interface topologies can be categorised into standard topologies, multiport topologies, and multilevel topologies [42]. Standard topologies describe converters, usually known as two-port converters because of the connection of their input ports to the energy source and the output port to the load. The power converter structures can be either single-stage or double-stage for this topology. In the single-stage structure, a single converter controls the charge and discharge of the energy storage and connects the input to the grid. Two converters are used in the double-stage structure: a DC/DC converter to control charge and discharge of the energy storage and a DC-AC converter to provide the connection to the grid and regulation of power output. Multilevel topologies are used in high voltage applications to achieve the desired output voltage by selecting many different levels of input DC voltage. Finally, for the multiport topology, the converter processes energy from multiple energy sources or to multiple loads.

For this project's model, the double-stage structure of the standard topology is implemented. It is worth mentioning that only average converter models are used in the simulations; hence, much focus isn't given to variables due to switching. The choice of which topology of DC/DC converter to use was dependent mainly on the technology of energy storage and the nature of investigations being carried out. The DC network voltage considered for this work is low voltage (120-1500V DC, according to the International Electrotechnical Commission, IEC). Considering primary power sources which are usually not current-reversible, e.g. a photovoltaic source or fuel cell, a boost converter can adapt their low voltage outputs to regulate the DC bus voltage properly. In work done by [94], [95], and [96] a bidirectional buck-boost converter is used both for a battery and supercapacitor. It provides a current reversal capability to allow both charging and discharging. It is important to add that the developed model can be implemented in more

35

advanced studies where technology-specific blocks of batteries and supercapacitors are implemented.

The HESS's charge and discharge capabilities are defined as the buck and boost modes of operation, respectively. Considering that the HESS elements have their input voltages increased at the output to the rated DC bus voltage, the boost converter is selected as a basis for the bidirectional converter to be designed. A brief description of the boost converter, whose typical basic configuration is shown in Figure 4.4 below, is given.
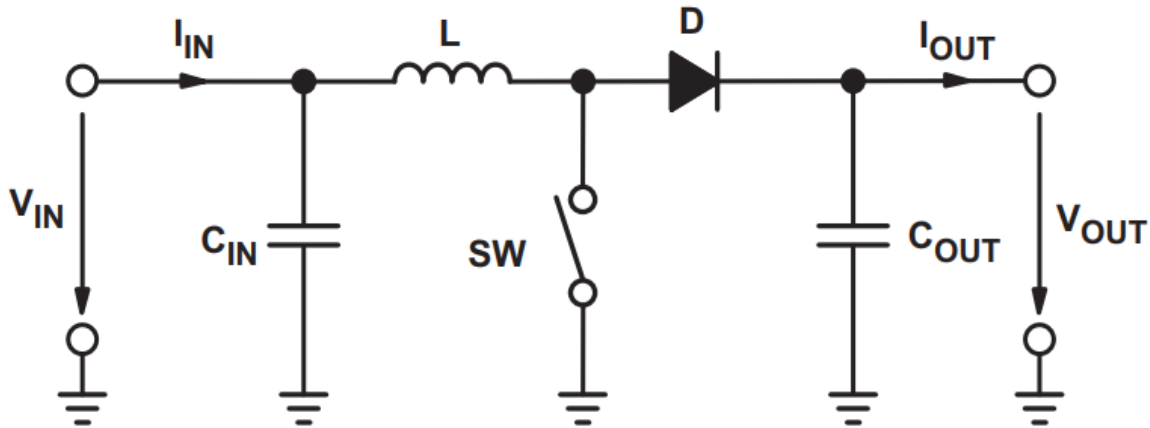
Figure 4.4: Boost converter [97]

Boost converter

The boost or step-up converter is implemented in regulated DC power supplies and regenerative braking of motors. Its output voltage is always higher than its input voltage, dependent on the value of the duty cycle. When the switch is turned on, the diode is reverse biased, and the input source is isolated from the output. During this 'ON' period, the input source charges the inductor to the desired voltage. When the switch is turned off, i.e. the 'OFF' period, the output receives energy supply both from the inductor and the input source. As observed from the figure above, power flow is unidirectional due to the presence of the output diode.

The equation relating the parameters for a given boost converter is given in (4.3) where V_o and V_d are the output and input DC voltages, and the D is the duty cycle.

$$\frac{V_o}{V_d} = \frac{1}{1-D} \tag{4.3}$$

A summary of equations defining the operations of the DC/DC converters described above is given in Table 4.1 from [98]. It shows how the controlled input current and output voltage are computed based on a given duty cycle. The focus here is the characteristics of the boost converter. The highlighted expressions of the boost converter are used in design the bidirectional converter.

Converter	Output voltage, Vout	Input current, Iin
Buck	$v_{out} = DutyCycle * v_{in}$	$i_{in} = DutyCycle * i_{out}$
Boost	$v_{out} = \dfrac{v_{in}}{1 - DutyCycle}$	$i_{in} = \dfrac{i_{out}}{1 - DutyCycle}$
Buck-boost	$v_{out} = \dfrac{DutyCycle * v_{in}}{1 - DutyCycle}$	$i_{in} = \dfrac{DutyCycle * i_{out}}{1 - DutyCycle}$

Table 4.1: Voltage and current equations for converters [98]

In the BDC simulation model made for this project, the diode of the boost converter, see Figure 4.4, is replaced with a second switch. The resulting converter is equivalent to the 2-quadrant DC/DC converter model shown in Figure 4.5 below with two IGBT switches connected to antiparallel diodes. This configuration provides the converter with the ability to direct current flow in and out of the storage device.

During the buck mode where the upper switch (s_b) is closed power is transmitted from the high-voltage side (DC bus) to the low-voltage side (energy storage); hence, the inductor current is negative, and the storage is charged. Conversely, in the boost mode when the lower switch ($\bar{s}_b$) is activated, power is transmitted from the low-voltage side to the high-voltage side, and inductor current is positive [99]. The average duty cycle controlled (D-controlled) 2-quadrant DC/DC converter is used in the simulation model as the BDC. Also, the continuous conduction mode (CCM) of operation is assumed in the determination of the converter parameters.
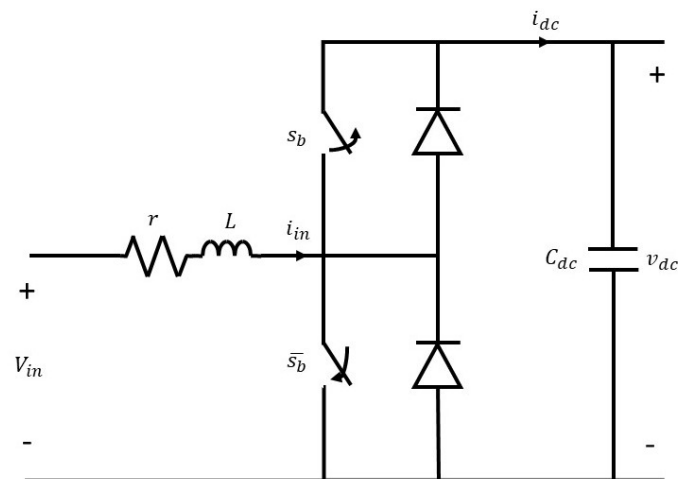

Figure 4.5: Bidirectional converter

The figure above also shows how the energy storage device is connected to the DC grid via its corresponding bidirectional converter. The input voltage is positive, and power losses are considered negligible for this study. The energy storage input voltage is fixed throughout the simulations.

Considering a mode of operation where current is flowing from the AC system towards the DC bus and energy storage, the following equations describe the dynamics of the BDC as given by Sanchez in [100]:

$$\frac{di_{in}}{dt} = \frac{-r_n * i_n}{L_n} - \frac{V_n}{L_n} + \frac{s_n * v_{dc}}{L_n}$$

(4.4)

$$\frac{dv_{dc}}{dt} = \frac{i_{dc} - s_n * i_{in}}{C_{dc}}$$

(4.5)

n used in these equations represent each energy storage device under consideration, i.e. battery and supercapacitor. s_n is the switch signal, i_{dc} is the incoming current from the DC grid, i_{in} is the input current to the converter, v_{dc} is the DC bus voltage, C_{dc} is the DC bus capacitor, V_n is the input storage voltage, and L_n is the converter inductance.

The power stage design computations for both storages' DC/DC converters are detailed in MATLAB script A.1, Appendix A. Information from [101] provides design approximations for the input filter inductor and output DC link capacitor. These equations are necessary when no datasheet information is available, like the case of this project. An arbitrary low value of 0.001Ω is chosen for the inductor series resistance (r_n). The minimum energy storage inductance L_{min} and minimum DC link capacitance $C_{dc,min}$ are determined below. As will be seen from the script, an adjustment is later made to the DC bus capacitor to improve the output response. Since the calculated value is the minimum value, this is acceptable, so long as system stability is not affected.

$$L_{min} > \frac{D_n * V_n * (1 - D_n)}{f_{sw} * 2 * I_{dc}}$$

(4.6)

$$C_{dc,min} > \frac{I_o}{V_r * f_{sw}}$$

(4.7)

Where D_n is the duty cycle of the storage device, V_n is the storage input voltage or source voltage, f_{sw} is the switching frequency of the converter modulator, V_r is the maximum allowable voltage ripple selected as 2%, and I_{dc} is the rated output current determined from the rated output power and the DC link rated voltage. All the values of the components are available in MATLAB script A.1. When the DC and AC standalone systems are connected to give the full system, some of these parameters are modified as observed in MATLAB script A.3.

The remaining BDC passive component characteristics are determined as shown in (4.8) - (4.11) below, where the parameters have the same descriptions as those used in (4.6) and (4.7). The input inductor current (I_n) for energy storage is given as:

$$I_n = \frac{I_{dc}}{1 - D_n}$$

(4.8)

The peak-to-peak inductor ripple current (ΔI_n), where f_{sw} is the switching frequency and L_n is the input filter inductance is:

$$\Delta I_n = \frac{V_n * D_n}{f_{sw} * L_n} \tag{4.9}$$

The inductor maximum RMS current ($I_{n,rms}$), where P_{dc} is the rated output power is:

$$\sqrt{\left(\frac{P_{dc}}{V_n}\right)^2 + \frac{\Delta I_n^2}{12}} \tag{4.10}$$

Finally, the inductor switching peak ripple current ($I_{sw,p-p}$) is given as:

$$\sqrt{D_n * \left(\frac{P_{dc}}{V_n}\right)^2 + \frac{\Delta I_n^2}{12}} \tag{4.11}$$

The design parameters of energy storages and bidirectional converters for the standalone DC system simulation model are all presented in Tables 4.2 and 4.3 below:

Parameter	Description	Value
V_b	Input voltage	200V
D_b	Duty cycle	0.5
L_b	Converter filter inductance	0.2mH
r_b	Inductor series resistance	0.001Ω
I_b	Input inductor current	25A
$I_{b,r}$	Inductor peak-to-peak current ripple	50A
$I_{b,rms}$	Maximum inductor RMS current	28.87A
$I_{b,sw}$	Inductor switching peak ripple current	22.82A
ESR_b	Capacitor equivalent series resistance	0.3505Ω

Table 4.2: Nominal battery converter parameters

Parameter	Description	Value
V_{sc}	Input voltage	250V
D_{sc}	Duty cycle	0.38
L_{sc}	Converter filter inductance	0.23mH
r_{sc}	Inductor series resistance	0.001Ω
I_{sc}	Input inductor current	20A
$I_{sc,r}$	Inductor peak-to-peak current ripple	40A
$I_{sc,rms}$	Maximum inductor RMS current	23.09A
$I_{sc,sw}$	Inductor switching peak ripple current	16.83A
ESR_{sc}	Capacitor equivalent series resistance	0.48Ω

Table 4.3: Nominal supercapacitor converter parameters

Selection of the DC bus capacitor's ESR value is a matter of choice between the computed values for the battery and supercapacitor. Hence, the capacitor's ESR is selected. The rated values for the DC grid parameters are also presented.

Parameter	Description	Value
V_{dc}	Nominal DC bus voltage	400V
P_{dc}	Rated power	5kW
V_r	Maximum voltage ripple (2%)	8V
f_{sw}	Switching frequency	10kHz
I_{dc}	Rated load current	12.5A
R_{dc}	Rated load	32Ω
$I_{dc,max}$	Maximum load current	13.75A
C_{dc}	DC bus capacitor	1.3mF
ESR_{sc}	Capacitor equivalent series resistance	0.48Ω

Table 4.4: DC bus components and grid parameters

4.2 AC system

4.2.1 Three-phase, two-level voltage sourced converter (2L-VSC)

A schematic of the standalone AC system is presented in Figure 4.6. For this project, a 2-level voltage sourced converter interfaces the HESS to the 3-phase AC system. An average voltage reference-controlled (U-ref controlled) model of the VSC is used in the simulation model. A VSC is used because its commutation algorithm can be implemented using Pulse-Width Modulation (PWM). Also, it is better at self-commutation and does not inject as many harmonic currents into an AC grid compared to a current sourced converter (CSC) performing a similar function [102]. A brief discussion of the 2-level VSC is given in this subchapter to set a premise to understand the later sections better.
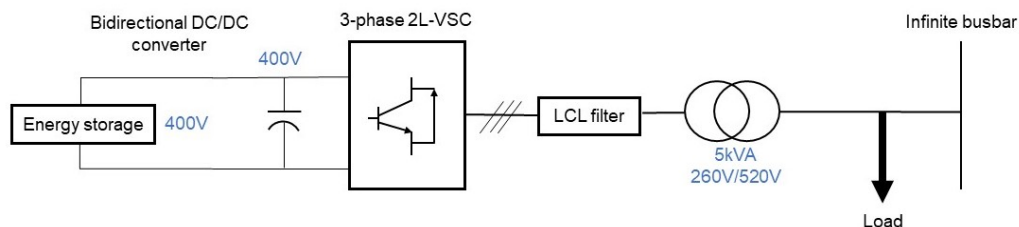
Figure 4.6: Standalone AC system schematic

The structure of the 3-phase 2L-VSC is shown in Figure 4.7 below. It is composed of three identical half-bridge converters whose DC-sides are connected to a common DC bus, and in this project's case, in parallel to the HESS and DC bus capacitor on the other side. It is called the 2L-VSC because its AC-side terminals can assume voltages of $+0.5V_{dc}$ or $-0.5V_{dc}$, where V_{dc} is the DC-side voltage [103]. In maintaining safe operation,

semiconductor switches on the same leg are operated in a complementary manner. As such, each switch must be able to sustain the DC voltage since at every instant only one switch is active. The 2L-VSC can provide bidirectional power flow between the DC-side voltage source and the 3-phase AC grid. In this project, an AC passive grid with a resistive load is modelled. Each half-bridge converter is indexed with letters a, b, c to associate them with each phase of the AC system.
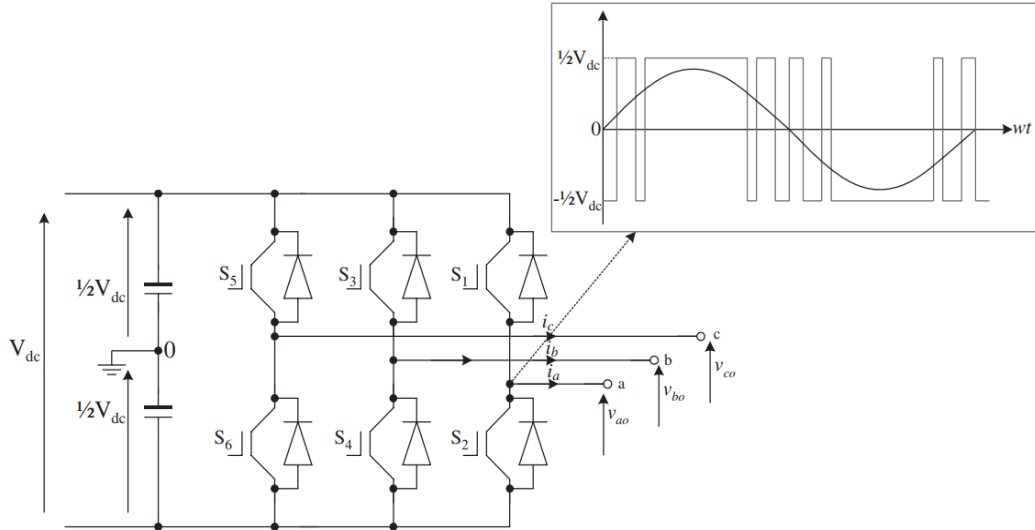

Figure 4.7: Two-level VSC [22]

A VSC system can be controlled in either the $\alpha\beta$-frame or dq-frame; this is explained further in Chapter 5. For this project's simulation model, the VSC is controlled in the dq-frame. Using the dq-frame, signals and variables are converted to equivalent DC quantities. Hence, conventional PI controllers are implemented in control because they are not influenced by the operating frequency. In asymmetrical 3-phase systems, $\alpha\beta$-frame representation results in time-varying signals which makes control design more involving. However, a dq-frame representation gives models with constant parameters, therefore simplifying the control task. Conventionally, components of many large power systems and developed and analysed in the dq-frame [104], hence the representation of the VSC in this frame allows analysis and design based on methods used for many other commercial power systems. This gives a unified framework based on which much valuable information can be accessed. Based on the reasons given above and more, the decision to model and control the 2L-VSC in the dq-frame has been well-informed.

The AC-side terminal active and reactive power of the 2L-VSC is formulated using the dq-components of the AC voltage and current (vd, vq and id, iq) as:

$$p_{ac} = \frac{3}{2}(v_d * i_d + v_q * i_q) \tag{4.12}$$

$$q_{ac} = \frac{3}{2}(v_q * i_d - v_d * i_q) \tag{4.13}$$

In the control of the VSC for this project, v_d is aligned to the AC voltage vector to set v_q at zero. The real and reactive power components exchanged between the VSC and AC grid, therefore, become proportional to the converter currents i_d and i_q, respectively.

The angular position of the rotating voltage vector is given as

$$\theta = tan^{-1}\left(\frac{v_\beta}{v_\alpha}\right) \qquad (4.14)$$

Where v_β and v_α are the components of the voltage in the two stationary reference frame axes based on Clarke's transform. The angle θ is computed using a phase-locked loop (PLL), as shown in Figure B.7.

Assuming a power balance between the DC and AC grids, the AC power from (4.12) can be equated to the DC power, i.e.

$$p_{dc} = p_{ac} \qquad (4.15)$$

$$v_{dc} * i_{dc} = \frac{3}{2}(v_d * i_d + v_q * i_q) \qquad (4.16)$$

The next important aspect of VSC modelling is the filter at its output terminals. The filter facilitates feedback control by imposing a current-like performance and eliminates or mitigates harmonics in the output current. In enhancing output power quality from the VSC, an LCL filter is usually connected in series with it. A simple LCL filter is shown connected between the VSC and transformer in Figure B.6. The LCL filter has proven very useful in minimising the distortion of current injected in the utility grid; hence, the choice to design one for this project's power system. Considering that a star-star (Y-Y) transformer is connected after the VSC, the goal is to design a three-phase filter, with a wye-connected filter capacitor and with damping, for a non-galvanic isolated inverter.

In following a systematic filter design procedure, characteristics such as filter size, output current ripple, and switching ripple attenuation are considered [105]. In avoiding resonance of the capacitor with the grid due to reactive power requirements, a passive damping resistance is connected in series with it. For the filter design, the following parameters are used: line-to-line RMS and phase voltages at the VSC side (V_{vsc} and $V_{vsc,ph}$), rated active power (P_n), voltage at DC bus (V_{dc}), nominal grid frequency (f_n), switching frequency of PWM (f_{sw}), and the resonance frequency (f_{res}). All computations carried out here are found in MATLAB script A.2.

The filter parameter values are computed as a percentage of the base values of impedance and capacitance, i.e. Z_b and C_b . The AC base values for the model are presented in detail later in Chapter 5. In designing the filter capacitance (C_f) the requirement under consideration is achieving a maximum power factor variation of 5%. The filter capacitor is therefore given as:

$$C_f = 0.05 * C_b \qquad (4.17)$$

This value can be adjusted to be higher should there be the need to compensate for the inductive reactance of the filter. The maximum ripple current (ΔIL_{max}) at the inverter output

is given in (4.18) where m is the modulation factor for a usual sinusoidal pulse-width modulation (SPWM) converter. Given that L_1 is the inverter side inductor of the filter and T_{sw} is the switching period,

$$\Delta IL_{max} = \frac{2V_{dc}}{3L_1}(1 - m) * m * T_{sw}$$ (4.18)

Knowing that maximum peak-to-peak ripple current occurs at $m = 0.5$, the equation above simplifies to:

$$\Delta IL_{max} = \frac{V_{dc}}{6 * f_{sw} * L_1}$$ (4.19)

As a matter of choice, a 10% ripple of the rated output current is desired, i.e.

$$\Delta IL_{max} = 0.1 * I_{max}$$ (4.20)

$$\Delta IL_{max} = 0.1 * \frac{P_n \sqrt{2}}{3 * V_{vsc,ph}}$$ (4.21)

The inverter-side filter inductance L_1 can now be determined using this value of maximum ripple current in (4.21). The inductor resistance R_1 is selected arbitrarily, and this value is adjusted until the desired response is obtained in the grid outputs.

The second inductor of the filter L_2 is selected as the total leakage reactance of the windings of the step-up transformer connected in series with the filter. This value is usually 0.06pu; hence, it is used as such in designing the filter. The typical leakage resistance is 0.02pu, and this is used as well in determining the total resistance of the system.

The final component is the capacitor's damping resistor R_f which attenuates part of the ripple due to switching to avoid resonance. The selected value is considered as approximately a third of the filter capacitor's value, at the resonance frequency f_{res}. The resonance angular frequency (ω_{res}) is given in (4.22) below with the limitation that $10f_n < f_{res} < 0.5f_{sw}$:

$$\omega_{res} = \sqrt{\frac{L_1 + L_2}{L_1 * L_2 * C_f}}$$ (4.22)

Finally, the damping resistor is calculated below:

$$R_f = \frac{1}{3 * \omega_{res} * C_f}$$ (4.23)

Following these steps, the LCL filter with a wye-capacitor configuration is designed and connected at the output of the 2L-VSC. The final tested system parameters for the 2L-VSC and its output filter are tabulated below:

Parameter	Description	Value
V_{dc}	DC side voltage	400V
V_{vsc}	AC RMS line voltage	260V
P_n	Rated power	5kW
f_n	Nominal grid frequency	60Hz
f_{sw}	PWM switching frequency	5kHz
L_1	VSC output side inductor	8.5mH
L_2	Grid side inductor	2.2mH
C_f	Filter capacitor	9μF
R_f	Damping resistor	4.60Ω

Table 4.5: 2L-VSC and filter parameters

4.3 Overall system

The Simulink simulation model of the entire power system is given in Figure B.11. It shows all the system components presented earlier in the chapter. Also, the schematic of this model given in Figure 1.1, Chapter 1 can be used as a reference.

As explained earlier, the storage devices (DC voltage sources) are connected to the DC bus through corresponding 2-Quadrant bidirectional DC/DC converters. These converters provide both boost and bidirectional capacities. The power electronic interfaces provide full controllability for the HESS elements [106]. They act cooperatively to match the HESS's output voltage to the DC bus voltage. A capacitor with an equivalent series resistance (ESR) is connected across the DC bus to provide electrical inertia for keeping DC bus voltage almost constant during a transient event [96]. The controlled current source, which was acting as a variable load in the DC system, is now taken. The input ports of the 2L-VSC are connected across the DC bus capacitor. This modification means the DC voltage source acting as energy storage and the series resistor and inductor representative of the converter passive components are removed from the standalone AC system model.

The transformer connected after the LCL filter described earlier steps up the converter's low voltage output to a higher voltage demanded by the AC grid. The resistive load and three-phase AC source in swing mode (infinite busbar where nominal voltage, phase, and frequency are defined) remain as the final components of the system.

5 Control design

Coordination of the ES devices in the HESS can be categorised as passive [80], semi-active [107], or active [108]. Active coordination is the most efficient since it eliminates the mismatch between the ES terminal voltages and voltage at the system bus. Moreover, ES output powers can be scheduled to ensure complete utilisation of power and energy capacities. Hence, ES active coordination is used in the control of the HESS for this project. The next task for HESS control is the decomposition of system net power.

Many HESS control algorithms implement a filter-based central control which sends the system net power through low or high-pass filters in generating references for the different ESs [109]. Literature from [110] defines system net power as the difference between load consumption and power generation. It can be decomposed into high-frequency and low-frequency components where the low-frequency component causes slow power variation, and the high-frequency component results in power variation within short periods [111]. The ranges of these frequency components are dependent on the choice of the control designer. Reference [113] uses a wavelet transform to decouple high frequency and low-frequency components of net power demand to operate a hybrid battery-supercapacitor system. Work done by [114] involves applying a model predictive control strategy to designate quick and slow changes in output current to a battery and supercapacitor HESS. All strategies used by the literature above need to measure system net power accurately, and a central controller is needed to generate the power reference for each ES based on its operating range. However, this approach likely suffers from communication delays or errors. Decentralised control can be adopted to improve system reliability and eliminate the need for central controllers depend on communication links. In decentralised control, each terminal makes an individual decision based on conditions or measurements in its locality [115].

In this project, the response of both storage devices to a load demand variation is incorporated in the control design. In explaining this further, a slow response time defines operation at low bandwidth and vice versa for high bandwidth. For example, the supercapacitor absorbs variations in the high-frequency range, giving it a higher bandwidth of operation. This, on the other hand, is on account of its quick response time. Primarily, the ES with high energy density offsets power mismatch during steady-state, and the ES with high power density balances power mismatch during the transient period [112].

A schematic of the DC standalone system based on which the HESS control is designed was presented in Figure 4.1 earlier. The HESS elements act as current-controlled voltage sources connected with their corresponding DC/DC converters. The initial load resistance is parametrised as R_{dc} after which the resistance value can be changed by choosing different current values to represent a change in demand. The implementation of decentralised control strategies for both the DC and AC grid converter controllers is described further in the subsequent subchapters.

5.1 Bidirectional DC/DC converters

This subchapter describes the control design for the battery-supercapacitor HESS converters in the standalone DC system. The DC/DC converters are required to keep the DC bus voltage constant. Droop control is most commonly used in decentralised control of storage converters in literature like [116] and [117]. According to the droop-based control strategy, proportional power-sharing is only achieved during steady-state conditions, i.e. power-scale control. At the output of the converter, a virtual resistance (also droop coefficient) is seen from the relationship of classical voltage/current (V/I) or voltage/power (V/P) characteristics used in the droop control scheme [96]. This scheme is expressed mathematically as:

$$V_{out} = V_{ref} - R_i * I_{out}$$

(5.1)

Where V_{out} and I_{out} are the output voltage and current of the ith converter, V_{ref} is the nominal/reference bus voltage, and R_i is the droop coefficient observed as a virtual resistance at the DC bus. This virtual resistance (R_i) is calculated in (5.2) where V_{max} and V_{min} are the maximum and minimum allowed DC bus voltage variations and I_{max} is the maximum allowed converter output current.

$$R_i = \frac{V_{max} - V_{min}}{I_{max}}$$

(5.2)

In ensuring stable operation of the converter controllers, knowledge of the dynamic characteristics and suitable feedback and compensation application must be possessed.

5.1.1 Control strategy

Regarding the variant dynamic nature of different storage technologies, proportional power-sharing based on frequency ranges is recommended, i.e. time-scale control [95]. Employing this control strategy provides effective maintenance of DC bus voltage stability during transient and unbalanced load conditions. It also ensures optimum power-sharing between battery and supercapacitor or any other storage devices and guarantees an overall better response to system changes compared to power-scale control. Continuous control of the converter duty cycle ensures regulation of the DC bus voltage and well-timed or reduced charging and discharging frequency of the battery and supercapacitor. Stresses on the battery are therefore reduced, and its operational life is improved.

A general structure of the primary control method for a DC/DC converter is shown in Figure 5.1. This structure has been modified further in the design of the HESS control presented in Figure 5.2. H_i represents the inner current control loop and H_v represents the outer voltage control loop. V_{ref} is the reference voltage and I_{ref} is the inductor current reference obtained from the action of the outer voltage loop PI controller. I_o is the converter output current and V_o is the output voltage, both measured during the simulation. The other parameters are as described in the earlier chapters.
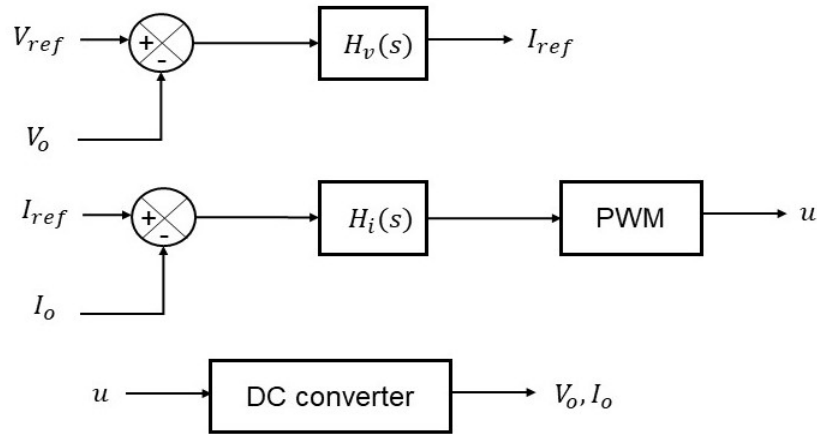
Figure 5.1: Primary control method of PI controllers [100]

The Simulink model of the DC/DC converter control used for this project based on the control method presented above is shown in Figure B.2. The scheme is shown in Figure 5.2 below.
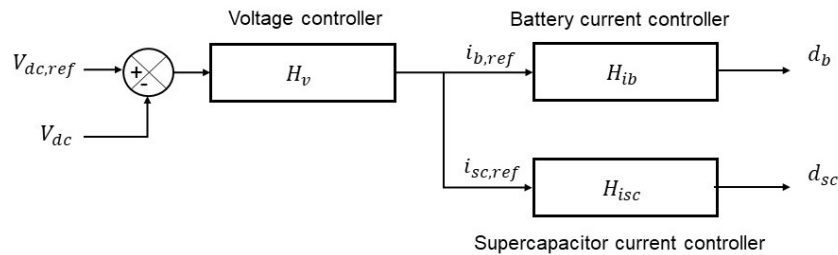

Figure 5.2: HESS control scheme

In the control strategy adopted for this work, the supercapacitor compensates variations due to fast transients, whereas the battery supports slow transients. The controllers are therefore designed with different bandwidths based on this requirement. The instantaneous grid voltage (v_{dc}) is compared with the reference voltage (V_{dc}) and the error is sent to an outer voltage loop PI controller to generate the total reference current (I_{ref}). This current is decoupled into battery and supercapacitor reference currents where the controllers act on the average power component and the dynamic component, respectively. The inner current loops control current injection into the system, and the outer voltage loop control controls the terminal voltages of the converters. The inner loop PI controllers generate duty cycles (d_n) with which the average converters are controlled, regulating their output voltage and current. Since average models of the DC converters are used, the DC/DC PWM generator is not required.

State-of-Charge (SOC), though an essential factor, is not included in the control strategy for this study because it is assumed that it remains within acceptable ranges throughout the investigations carried out.

Based on information from [118], the boost mode (discharging) and buck mode (charging) share the same transfer function; hence, it is possible to design a unified controller for

both modes of operation. Therefore, during the control design process, one mode must be chosen as a foundation, and the boost mode is selected considering the lower input storage voltages.

Using boost converter equations, the rated duty cycles (D) for both storage devices are computed using the expression in (5.3). The other parameters are the output voltage of both ESS elements, i.e. the DC reference voltage (V_{dc}) and their input voltages (V_i). The rated duty cycles of the battery and supercapacitor are given in (5.4) and (5.5), respectively. Parameters with subscripts 'b' represent the battery, and those with subscript 'sc' represent the supercapacitor.

$$V_{dc} = \frac{V_i}{1 - D} \tag{5.3}$$

$$D_b = 1 - \frac{V_b}{V_{dc}} \tag{5.4}$$

$$D_{sc} = 1 - \frac{V_{sc}}{V_{dc}} \tag{5.5}$$

Only the continuous conduction (CCM) mode of operation is considered in the design, where there are only two states of the converter: ON and OFF, and current is continuous.

5.1.2 Model of PI controller

It is apparent from the review of literature that the PI controller is typically implemented and has proven effective in converter applications relevant to this project. As will be seen later, the dynamic model of a PI controller introduces a new state variable to the system; hence, bringing feedback and output regulation.

Regarding Figure 5.3 below, a standard PI controller model mostly used in power electronics control is described by (5.6) and (5.7) where y_{ref} is the reference input of the system, y is the output, u is the controller output, d is the decoupling term, and K_p and K_i are the controller proportional and integral gains, respectively. The added state is γ_l where the subscript 'l' represents different PI loops.

$$\gamma_l = y_{ref} - y \tag{5.6}$$

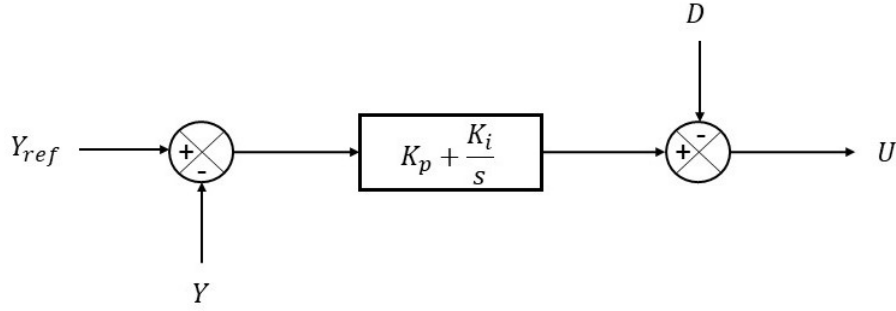$$u = K_p * \left(y_{ref} - y\right) + K_i * \gamma_l - d \tag{5.7}$$

Figure 5.3: Block diagram of standard PI control [100]

Using the block diagram above, (5.6) and (5.7) are expressed in the Laplace domain as:

$$U = \left(K_p + \frac{K_i}{s}\right) * (Y_{ref} - Y) - D \tag{5.8}$$

Generally, given that b is a parameter specific to a plant to be controlled, the plant can be represented as:

$$H(s) = \frac{b}{s} \tag{5.9}$$

Given that the proportional and integral gains result in a PI controller given as:

$$G_c(s) = K_p + \frac{K_i}{s} \tag{5.10}$$

The characteristic closed-loop polynomial equation is [100]:

$$A(s) = s^2 + K_p * b * s + b * K_i \tag{5.11}$$

Now, to find the expressions for the PI controller gains, (5.11) is equated to the standard second-order equation $s^2 + 2\rho\omega_o s + \omega_o^2$ where ρ is the damping ratio, which determines the shape of the control response. ω_o determines the speed of response. The controller gains are determined as:

$$K_p = \frac{2\rho\omega_o}{b} \tag{5.12}$$

$$K_i = \frac{\omega_o{}^2}{b} \tag{5.13}$$

The time constant of the controller system: $T_i(s) = \frac{2\rho}{\omega_o}$.

A damping coefficient (ρ) of 0.7 is selected for the design of the controllers—this value yields good step response as well as well-damped oscillations.

5.1.3 Bidirectional DC/DC converter control design

Implementing the PI controller model detailed above, the PI controllers for the BDC are now designed. Equations describing the dynamics of the bidirectional converter have already been presented in Chapter 4.1.2 and are presented again. The parameters have the same descriptions as before. These equations apply to both the battery and supercapacitor converters.

$$\frac{di_n}{dt} = \frac{-r_n * i_n}{L_n} - \frac{V_n}{L_n} + \frac{s_n * v_{dc}}{L_n} \tag{5.14}$$

$$\frac{dv_{dc}}{dt} = \frac{i_{dc} - s_n * i_n}{C_{dc}} \tag{5.15}$$

The supercapacitor has a faster rate of charge and discharge, and the outer voltage PI controller is tuned using its power stage parameters.

The PI controllers for the inner current control loops are tuned in the frequency domain using bandwidths (which determines the speed of response of the energy storages). Using a selected switching frequency (f_{sw}) of 10kHz and bandwidth of ω_{sw} for the DC/DC converter PWM, the bandwidth for the supercapacitor inner current loop (ωo_{sc}) is chosen lower than ω_{sw} by order of 6 (ni_{sc}) [119]. In diverting every fast-changing transient to only the capacitor, the battery current control loop is limited to a relatively smaller bandwidth (ωo_b) lower than ω_{sw} by an order of 10 (ni_b). Primarily, the voltage control loop is much slower compared to the current control loops, and to maintain stability during controller operation, a bandwidth (ωo_v) lower than that of the PWM switching by order of 20 (nv) is maintained. The entire controller design process is detailed in MATLAB script A.1.

$$\omega_{sw} = 2 * \pi * f_{sw} \tag{5.16}$$

$$\omega o_b = \frac{\omega_{sw}}{ni_b} \tag{5.17}$$

$$\omega o_{sc} = \frac{\omega_{sw}}{ni_{sc}} \tag{5.18}$$

$$\omega o_v = \frac{\omega_{sw}}{nv} \tag{5.19}$$

To maintain the stability of the converter, it must always operate within ranges less than the right hand-plane zero frequency given in (5.20). This frequency is dependent on the supercapacitor power stage [86].

$$f_{RHPZ} = \frac{(1 - D_{sc})^2 * R_{dc}}{2\pi * L_{sc}} \tag{5.20}$$

$$\omega_{RHPZ} = 2 * \pi * f_{RHPZ} \tag{5.21}$$

D_{sc} and L_{sc} are the rated duty cycle and the converter inductance of the supercapacitor computed earlier in the modelling tasks of Chapter 4.

Based on the PI model developed in the previous section and the above design considerations, the current controllers and voltage controller for the HESS are designed. The general current controller is designed using the following equations, where n represents each storage element.

$$Kp_n = 2\rho\omega_{on}L_n \tag{5.22}$$

$$Ki_n = \omega_{on}^2 L_n \tag{5.23}$$

The voltage controller is designed to regulate the DC bus voltage:

$$Kp_v = 2\rho\omega_{ov}C_{dc} \tag{5.24}$$

$$Ki_v = \omega_{ov}^2 C_{dc} \tag{5.25}$$

As has been explained, the voltage controller bandwidth is expected to be lower than that of both current control loops, i.e. $\omega_{ov} < \omega_{on}$ and specifically for this controller design: $\omega_{ov} < \omega_{ob} < \omega_{osc} < \omega_{RHPZ}$.

The equations presented above are used in the MATLAB script A.1 to calculate the controller parameters (gains). The results are presented in Table 5.1 below:

Parameter	Symbol	Value
Switching frequency	f_{sw}	10kHz
Switching angular frequency	ω_{sw}	62.8krad/s
Battery current loop bandwidth	ω_{ob}	6.28krad/s
Supercapacitor current loop bandwidth	ω_{osc}	10.47krad/s
Voltage loop bandwidth	ω_{ov}	3.14krad/s
Battery current controller proportional gain	K_{pb}	1.76
Battery current controller integral gain	K_{ib}	7895.7
Supercapacitor current controller proportional gain	K_{psc}	3.44
Supercapacitor current controller integral gain	K_{isc}	25702
Voltage controller proportional gain	K_{pv}	11
Voltage controller integral gain	K_{iv}	12337
Right hand zero frequency	f_{RHPZ}	8.49kHz
Right hand zero bandwidth	ω_{RHPZ}	53.33krad/s

Table 5.1: DC converter controller parameters

5.1.4 Verification of bidirectional converter

In this chapter, the bidirectional converters and their controllers are verified. This verification is done separately for the battery and the supercapacitor. The purpose of this verification is to ensure that the designed DC/DC converter can follow a step change closely, bidirectional power flow, and works as desired in maintaining DC bus voltage.

Figures B.4 and B.5 are the standalone simulation models for the connection of battery and supercapacitor to the DC grid, respectively. These models are used in carrying out the verification simulations to determine the feasibility of the converters and their control. Three cases are simulated for this task: a step increase and a step decrease in load demand to investigate boost/discharging capability, and a negative step decrease in load demand to determine buck/charging capability of the converter.

5.1.4.1 Step increase in load demand

For a step increase in load demand from the rated value (I_{dc}) of 12.5A to 15A, changes in the converter output current and DC bus voltage are observed for the battery and supercapacitor converters. It is observed that the converter output currents for both energy storages follow the load demand as required. This ensures that the DC bus voltage is returned to normal after dropping initially due to the increase in demand. The difference observed between the reference and measured DC bus voltages is due to the less robust nature of the PI controllers designed. It is ascertained that the bidirectional converter model increases output current proportionally with the load demand. The results of this simulation are presented in Figures 5.4 and 5.5 for the battery and supercapacitor, respectively.

5.1.4.2 Step decrease in load demand

In simulating a step decrease in load demand from the rated value (I_{dc}) of 12.5A to 10A, changes in converter output current and DC bus voltage are also observed for the battery and supercapacitor converters. The converter output currents for both energy storage converters decrease proportionally with load demand. The DC bus voltage is therefore restored within milliseconds after transient rise due to a drop in demand. The simulation results for the tests are presented in Figures 5.6 and 5.7.
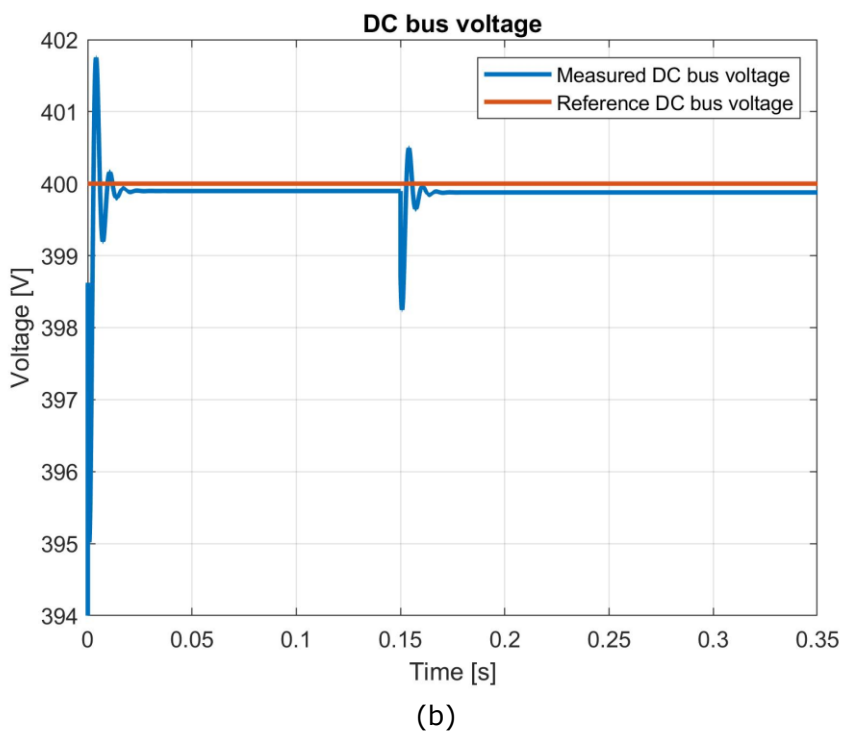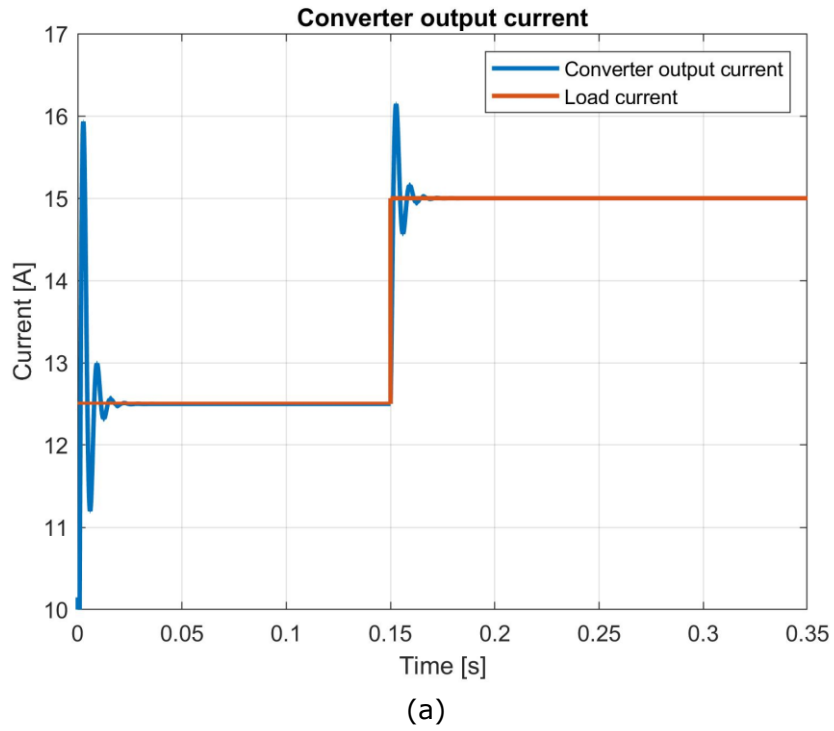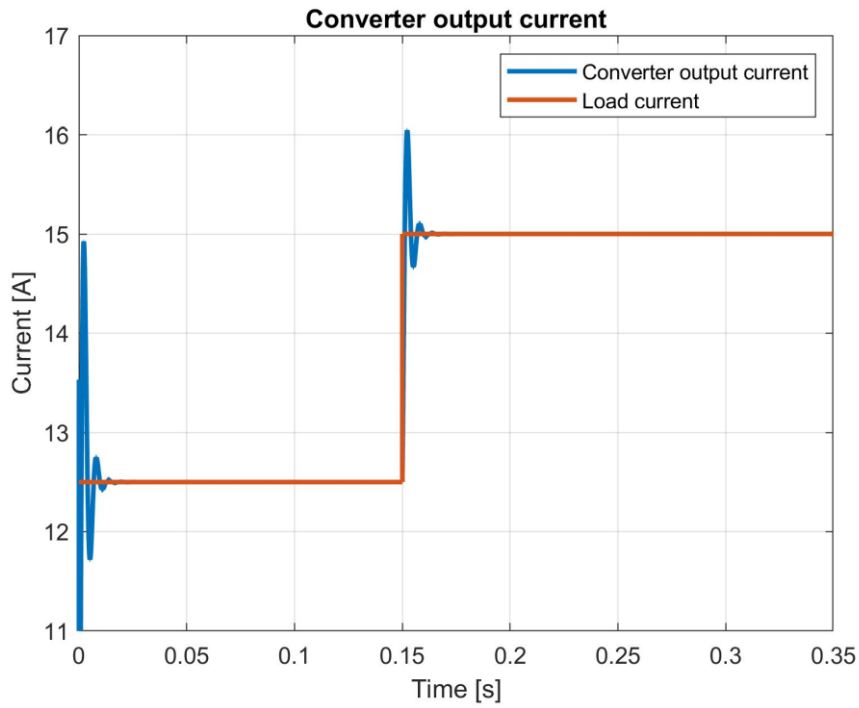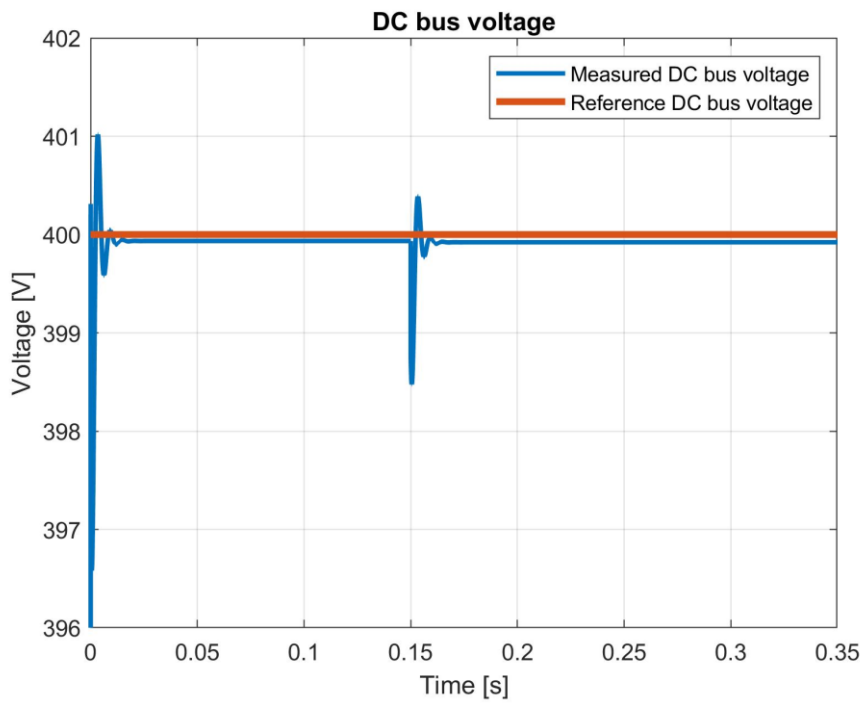
(a)

(b)

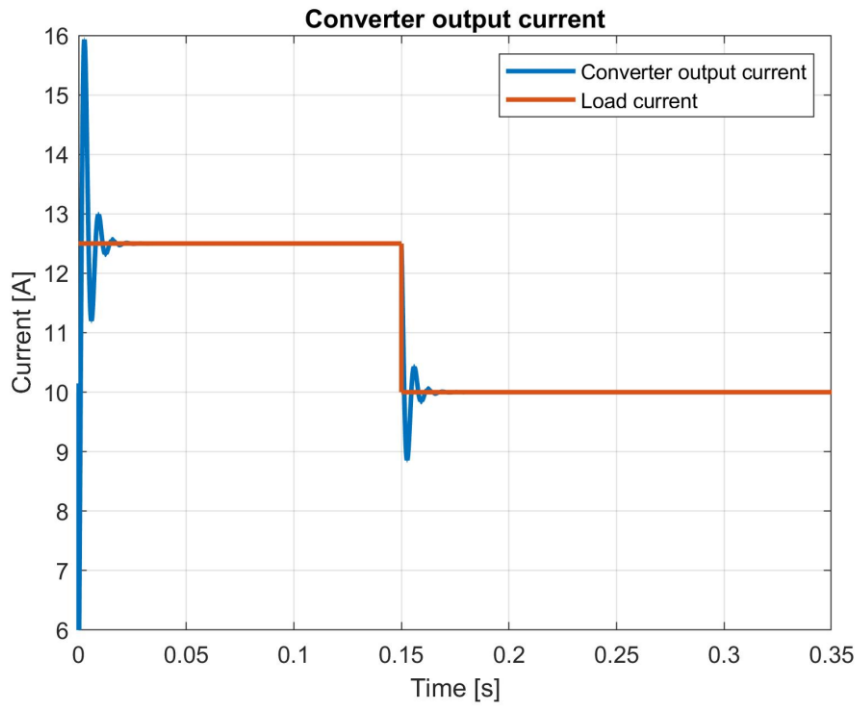**Figure 5.4: Step increase in load demand (a) Battery converter output current and (b) DC bus voltage**
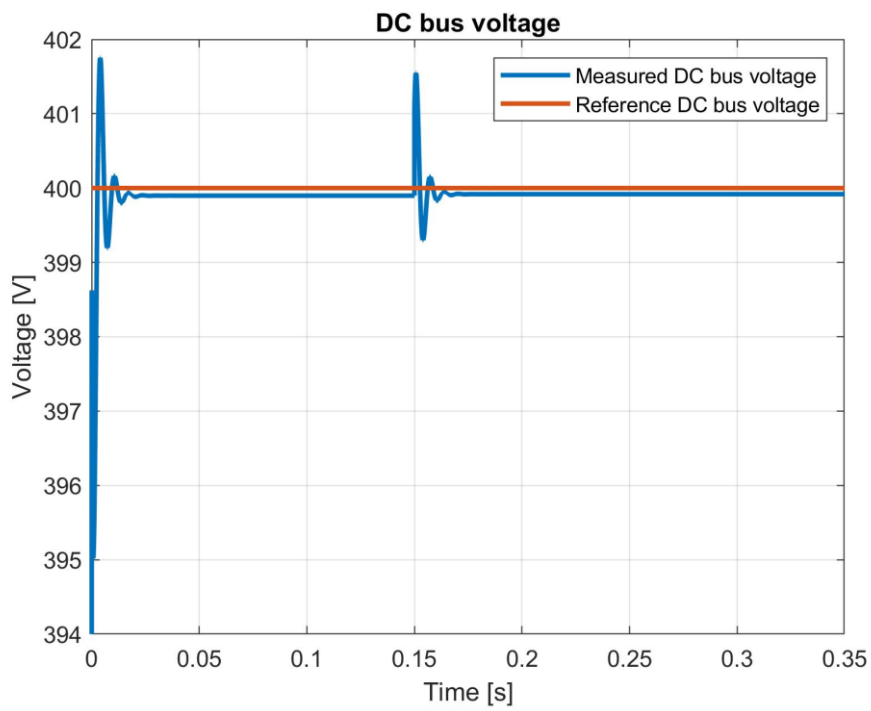
(a)

(b)

Figure 5.5: Step increase in load demand (a) Supercapacitor converter output current and (b) DC bus voltage
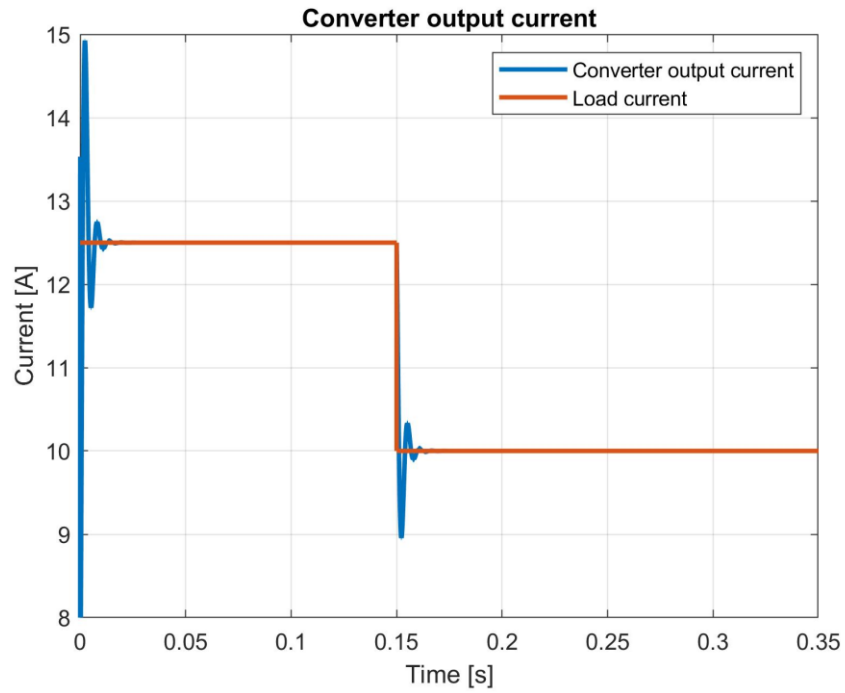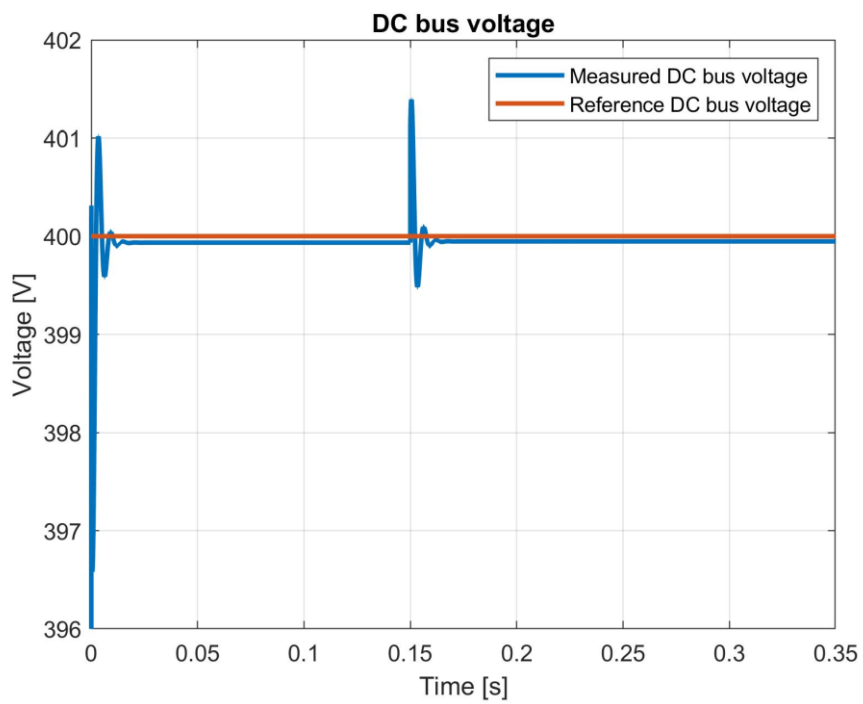
(a)

(b)

Figure 5.6: Step decrease in load demand (a) Battery converter output current and (b) DC bus voltage

(a)

(b)

Figure 5.7: Step decrease in load demand (a) Supercapacitor converter output current and (b) DC bus voltage

5.1.4.3 Negative load current

Finally, a negative load current is applied to verify the charging capability of the DC/DC converter, and only the battery standalone system is used for this verification. The supercapacitor converter is expected to give similar results with little difference. It is expected that converter output current reverses to follow the load current, and this in effect should restore bus voltage after it rises suddenly. In Figure 5.8 below, the bidirectional capability of the converter is verified when output current reverses to -5A to follow load demand.

It is observed that the measured DC bus voltage is not precisely equal to the reference voltage of 400V. Both converters of the battery and supercapacitor, when implemented individually, output a steady-state DC voltage of 399.9V. This little difference observed can be explained to be due to the controller design, which is not completely robust. This difference can also be as a result of voltage drops across small passive elements in the converters and the system. The converter PI controller design is based on a generalised model of a bidirectional DC converter, where controller gains are calculated only based on the following: switching bandwidth, DC bus capacitance, and converter inductance.

Implementing a technique such as small-signal modelling, non-idealities of the converter are incorporated. PI controllers designed using this method are tuned based on the control to inductor current and inductor current to output voltage transfer functions; hence, it is likely to produce more robust controllers and better output response. However, that is not the focus of this project, and since the controllers function appropriately to give the DC bus voltage with little to no steady-state error, they suffice for the simulation model. Moreover, it will be observed later that the HESS gives an output voltage of 400V equal to the reference at steady state, also proving the objective of the project to show how HESS implementation has more advantages over single energy storage.
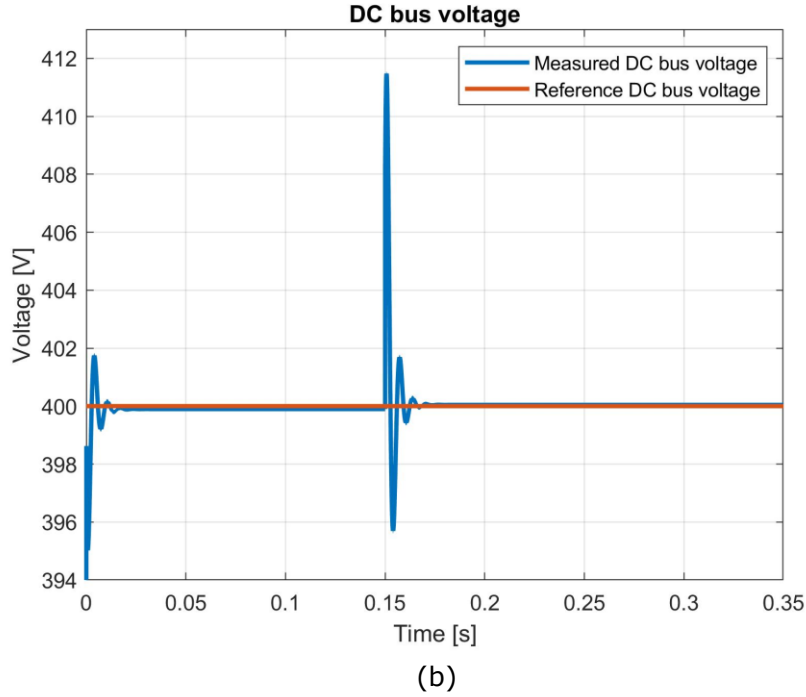

(a)

DC bus voltage

(b)
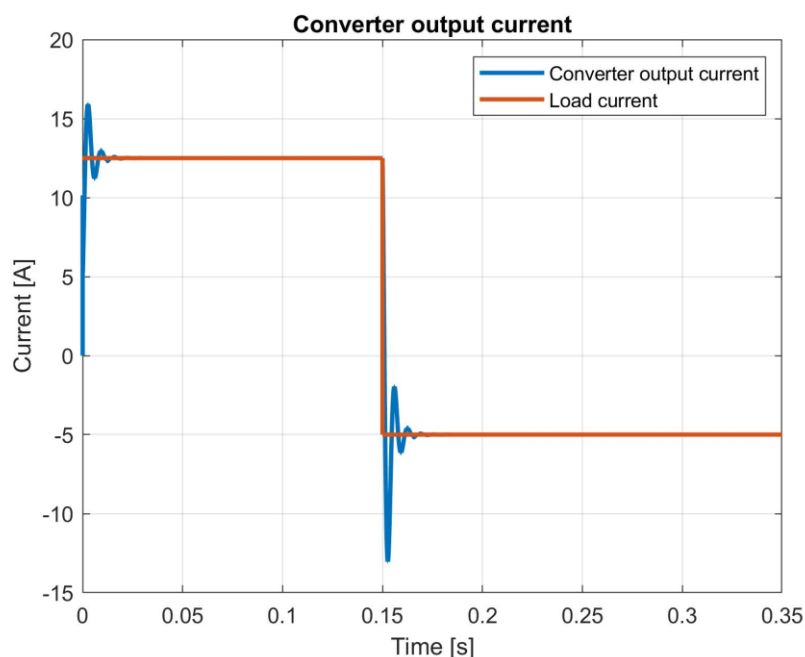
Figure 5.8: Negative load demand (a) Battery converter output current and (b) DC bus voltage

5.2 2L-VSC

This subchapter focuses on the control structure, modelling, and tuning of the two-level VSC used in the AC system. A schematic of the AC system based on which the modelling and verification of the 3-phase grid converter are carried out is presented in Chapter 4, Figure 4.6. The HESS elements and their DC/DC converters are modelled as an equivalent DC voltage source in series with a converter inductance and its resistor. This choice is made since the hybrid energy storage system (HESS) acts in regulating the DC bus voltage at a constant voltage. A resistive load is located at the output of the step-up transformer. A change in load demand is simulated by changing the active power setpoint (P^*) to vary current drawn by the 2L-VSC from the DC source. Since the HESS connected to the DC bus has elements which charge and discharge, the 2L-VSC must be capable of bidirectional power flow.

In the analysis of the AC system, basic equations have been developed based on analysis using Kirchhoff's Voltage Law (KVL) by [120] to describe the behaviour of the system. A general equation relating the phase voltages and currents is given below:

$$V_{abc} = R * i_{abc} + L\frac{di_{abc}}{dt} + V_{abc,conv} \tag{5.26}$$

Where V_{abc}, i_{abc}, and $V_{abc,conv}$ are the 3-phase voltage and current, and the DC converter input voltage, respectively. R and L are the total resistance and inductance of the series LCL filter at the output of the converter.

With the application of Clarke and Park's transformations detailed in Table C.1, Appendix C, (5.26) can be expressed in the dq-frame rotating at an angular frequency ω. These are given as:

$$L\frac{di_d}{dt} = -R * i_d + \omega L i_q - V_{d,conv} + V_d \tag{5.27}$$

$$L\frac{di_q}{dt} = -R * i_q - \omega L i_d - V_{q,conv} + V_q \tag{5.28}$$

Where $i_{d,q}$ and $v_{d,q}$ are the dq components of the 3-phase current and voltage, respectively. Referring to (1.2) and using the same descriptions for the variables and parameters:

$$i_{dc} = C_{dc}\frac{dv_{dc}}{dt} + i_{Load} \tag{5.29}$$

The 2L-VSC system used here is a grid-imposed frequency class because the three-phase AC source connected after load uses a swing mode of operation, making it act like a stiff grid. The operating frequency is, therefore dictated by the AC source and remains almost constant throughout the simulations carried out. The only changes observed in system frequency are during step changes in load demand.

Optimisation of compensators for a current-controlled VSC is quite tricky because the variables are sinusoidal functions of time. The closed-loop control system is associated with a sufficiently large bandwidth to ensure appropriate elimination of steady-state errors and effective disturbance rejection [103].

The 2L-VSC implements a decoupled PQ control where active power and reactive power setpoints are provided. Decoupled PQ control delivers constant active and reactive power based on a desired power factor. The 2L-VSC control strategy to be used is based on field-oriented vector control [121]. This is similar to the vector control method of voltage source inverters (VSIs) connected to induction motors using field-oriented control (FOC) and implementing the abc to dq-transformation or Park transformation. In FOC of induction motors, the instantaneous stator current is decomposed into flux and torque-producing currents. Either the rotor or stator flux linkage can be selected as the reference frame. The idea behind FOC is assuming that an induction motor is current-controlled [122]. The Park transform converts three-phase time domain components in the abc-reference frame to rotating components in the direct, quadrature, and zero, $dq0$-rotating reference frame. Assuming that the system for this project is balanced, the 0 component is always set at zero. The final coordinate system, therefore, consists of two dimensions, d and q.

The setpoints used in computing the reference currents can be defined by a local grid controller or a microgrid central controller (MCC). Considering the objective of investigating system variations during transients, there is no need for a central controller or energy management system (EMS) for this project. Power is injected or absorbed by the converter based on gating signals sent by the controller [29]. Control is achieved in the synchronous rotating $dq0$-reference frame [123], as mentioned earlier in Chapter 4. Figure 5.9 below presents a schematic of the control process of the 3-phase voltage source converter controller used in this project.
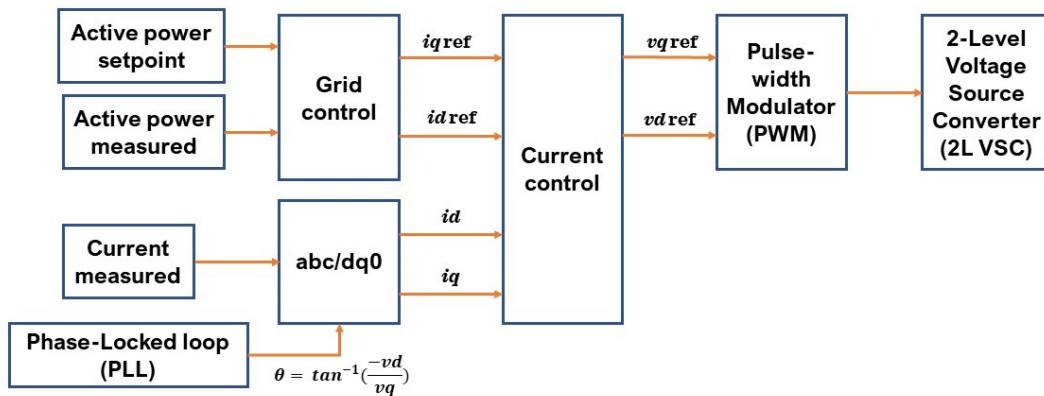
Figure 5.9: Schematic of the VSC control process using vector control

This schematic is further detailed in [124] where a typical control structure of a VSC is given, see Figure 5.10. In this project, the active power and reactive power controllers represent the outer control loop in the standalone AC system.
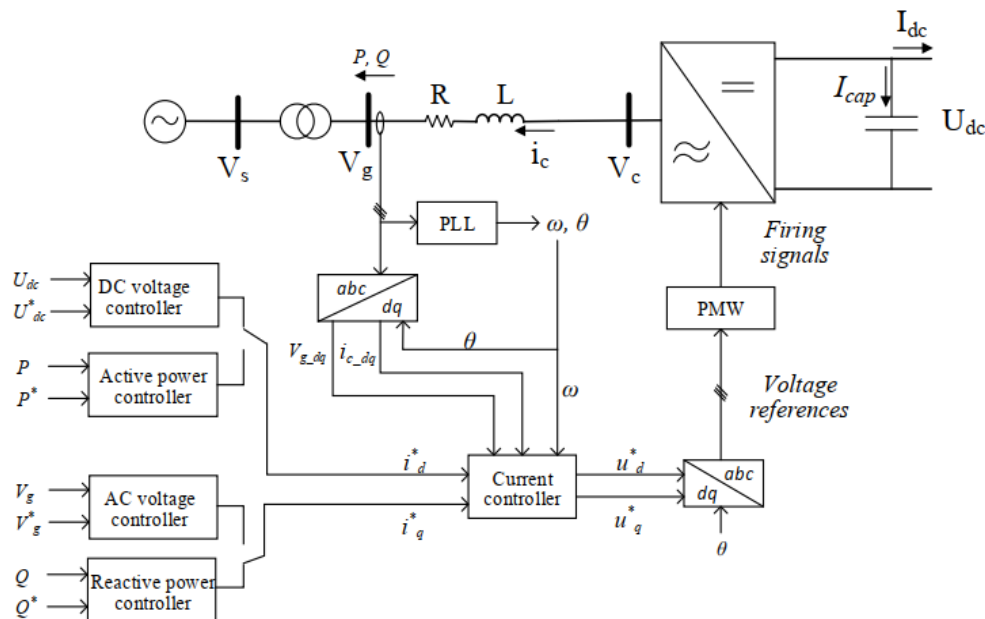

Figure 5.10: Control structure of VSC [124]

The measured three-phase grid voltage and current are converted using the Park Transform into direct and quadrature voltage and current components v_{dq} (v_d and v_q) and i_{dq} (i_d and i_q) respectively to be implemented in the converter controllers. The PLL is a control system which ensures that the phase of the output signal is relative to that of the converted input, i.e. it provides the reference angle for the transformation. Considering an a-phase to d-axis alignment, the Park transformation is given in (5.30) where the d component of the load voltage is set to the desired peak value, and the q component is fixed at zero.

$$\begin{bmatrix} d \\ q \\ 0 \end{bmatrix} = \frac{2}{3} \begin{bmatrix} \cos(\theta) & \cos(\theta - \frac{2\pi}{3}) & \cos(\theta + \frac{2\pi}{3}) \\ -\sin(\theta) & -\sin(\theta - \frac{2\pi}{3}) & -\sin(\theta + \frac{2\pi}{3}) \\ \frac{1}{2} & \frac{1}{2} & \frac{1}{2} \end{bmatrix} \begin{bmatrix} a \\ b \\ c \end{bmatrix} \tag{5.30}$$

The conversion from abc to $dq0$ components of the measured grid voltage and current and the implementation of the PLL are modelled in the 'PLL & Measurements' subsystem of the VSC's main controller as shown in Figure B.7.

The converter controller parameters, as will be seen in the upcoming subchapters, are tuned to maintain a trade-off between stability and response speed for small disturbances and robustness to withstand larger disturbances [125]. The parameters of the control loops are carefully selected to consider a range of operating conditions. The tuning rules which have been applied account for non-ideal operating conditions and try to mitigate them.

The simulation model components use SI units, whereas the control parameters are modelled in the per-unit (pu) system, to facilitate scalability. The following system base values are used in the calculation of the pu values of the controller parameters. The details of these computations can be referred to from the MATLAB script A.2.

$$zb = \frac{vb_{vsc}}{ib_{vsc}} \tag{5.31}$$

$$\omega b = 2 * \pi * fb \tag{5.32}$$

$$Lb = \frac{zb}{\omega b} \tag{5.33}$$

$$Cb = \frac{1}{zb * \omega b} \tag{5.34}$$

$$vb_{dc} = 2 * vb_{vsc} \tag{5.35}$$

$$ib_{dc} = \frac{3}{4} * ib_{vsc} \tag{5.36}$$

$$zb_{dc} = \frac{vb_{dc}}{ib_{dc}} \tag{5.37}$$

$$Cb_{dc} = \frac{3}{8} * Cb \tag{5.38}$$

The known parameters in SI units are changed to pu, following the determination of the AC and DC base values, for use in the controller designs. For the pu series filter resistances and inductances (R_1, R_2, L_1, L_2) required in the inner current control loop:

$$Rt_{pu} = \frac{R_1 + R_2}{zb} \tag{5.39}$$

$$Lt_{pu} = \frac{L_1 + L_2}{Lb} \tag{5.40}$$

The DC-side capacitance in pu is given as:

$$C_{dc,pu} = \frac{C_{dc}}{Cb_{dc}} \tag{5.41}$$

Hence, the decoupled control equation expressed in pu:

$$\left(\frac{L_{pu}}{\omega b}s + R_{pu}\right) * I_{dq,pu}(s) = V_{dq,pu}(s) \tag{5.42}$$

Finally, the equation of the DC bus dynamics from (5.29) in pu:

$$i_{dc,pu} - i_{load,pu} = \frac{1}{\omega_b * C_{dc,pu}}\frac{dV_{dc}}{dt} \tag{5.43}$$

5.2.1 Outer control loop

As mentioned earlier, computations carried out in the AC grid controllers are in per unit (pu) while the power system quantities are in SI-units.

As can be seen from Figure 5.10, the outer controller regulates either DC voltage or active power. The VSC outer controller designed for this project's simulation model controls the active power to follow a given active power setpoint. This scheme generates the reference current id^* sent to the inner current control loop. The AC voltage or reactive power is controlled to generate the reference current iq^*, but iq^* is set to zero. The objective is to supply only active power to a resistive load in the AC grid. A block diagram of the controller is shown in Figure 5.11 below. This diagram is used since the same principle is applied in the control of output active power to give the reference d current.

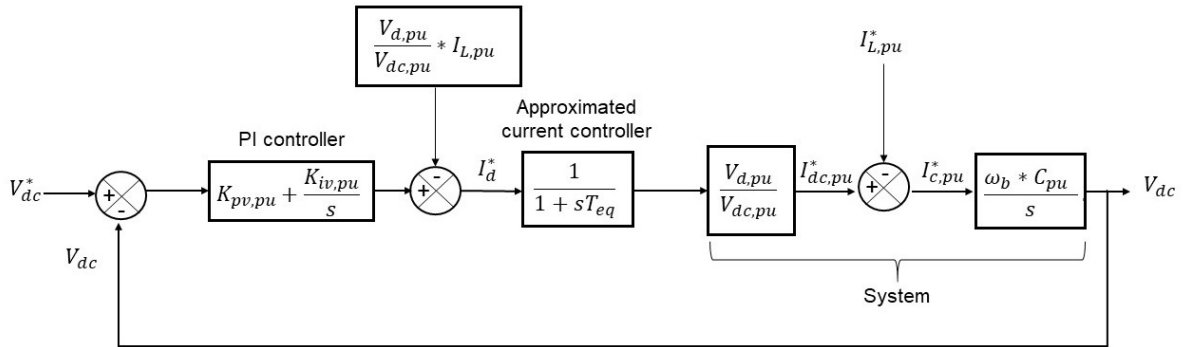**Figure 5.11: Block diagram of the outer voltage controller [125]**

A feedforward reference is included in the forward loop. Adding this reference improves the speed of response since a cascaded control strategy such as that of the VSC is likely to slow down response speed. Since the inner control loop is faster than the outer voltage loop, its second-order closed-loop transfer function is approximated by a first-order

transfer function whose time constant is given by $T_{eq} = 2 * T_a$. T_{eq} is equivalent time constant obtained from the first-order approximation of the current control loop and T_a is the delay associated with PWM switching. This equivalent time constant is determined by equating error functions of the two transfer functions.

The outer grid controller regulates active and reactive power injection into the grid by generating the dq-axes current commands, id^* and iq^*. Generation of these reference currents signifies the implementation of dq-transformation to independently control the active and reactive components of AC output power.

The input measured $dq0$ voltage and current components ($vdq0$ and $idq0$) are used in computing the three-phase instantaneous active and reactive powers (P and Q) and compares them with selected fixed power setpoints P* and Q*, where Q* is set to 0. Referring to (4.12) and (4.13) from Chapter 4:

$$p_{ac} = \frac{3}{2}(v_d * i_d + v_q * i_q) \tag{5.44}$$

$$q_{ac} = \frac{3}{2}(v_q * i_d - v_d * i_q) \tag{5.45}$$

Given that the zero components are equal to zero, they are not considered in the equations. These equations explain how independent control of i_d and i_q gives subsequent control of output powers P and Q.

5.2.1.1 Symmetrical optimum

It is demonstrated in the next subchapter that the modulus optimum criteria are used in the tuning of the controllers for a system having a dominant time constant and a minor one. However, with a pole near the origin or at the origin, pole shifting does not change the situation considerably. In the open-loop transfer function of the outer voltage controller, it already has two poles in the origin, see (5.46). The other alternative to tuning its controllers is known as the symmetrical optimum. With this method, the frequency response of the system is forced to low frequencies as much as possible. Hence, giving the advantage of maximising the phase margin. As the phase margin is maximised at a given frequency, the system tolerates more delays, and this is beneficial for systems with delays. This method optimises system behaviour with respect to disturbance inputs and maintains stability.

In Figure 5.11 above, the system transfer function without considering the feed-forward and disturbance input is given by:

$$G_{v,ol} = Kpv_{pu} * \left(\frac{1 + sT_{iv}}{T_{iv}}\right) * \frac{1}{1 + sT_{eq}} * \left(\frac{V_{d,pu}}{V_{dc,pu}} * \frac{\omega_b * C_{pu}}{s}\right) \tag{5.46}$$

Two new gain terms can be introduced, i.e. $K = \frac{Vd_{pu}}{Vdc_{pu}}$ and $T_c = \frac{1}{\omega_b * C_{pu}}$. Hence, the open-loop transfer function can be simplified to:

$$G_{v,ol} = Kpv_{pu} * \left(\frac{1 + sT_{iv}}{T_{iv}}\right) * \frac{K}{1 + sT_{eq}} * \left(\frac{1}{s * T_c}\right) \tag{5.47}$$

The tuning procedure of the symmetrical optimum is based on two Nyquist criteria [125] given by equations (5.48) and (5.49) below where ϕ_M is phase angle.

$$|Gv, ol(j\omega)| = 1 \tag{5.48}$$

$$\angle G_{v,ol}(j\omega) = -180 + \phi_M \tag{5.49}$$

Differentiation of the angle criterion given in (5.49) with respect to ω, gives the open-loop frequency characteristic of the controlled system a maximum phase margin at the crossover frequency ω_d, i.e.

$$\omega_d = \frac{1}{\sqrt{T_{iv} * T_{eq}}} \tag{5.50}$$

With this condition, the time constant of the controller T_{iv} is found as

$$T_{iv} = T_{eq} * \left(\frac{1 + sin\phi_M}{1 - sin\phi_M}\right) \tag{5.51}$$

The determined crossover frequency ω_d is symmetrical about $1/T_{iv}$ and $1/T_{eq}$. Based on this observed symmetrical property, given that a is the distance between $1/T_{iv}$ and ω and $1/T_{eq}$ and ω:

$$T_{iv} = a^2 * T_{eq} \tag{5.52}$$

Therefore, from the magnitude condition in (5.48), the proportional gain of the PI controller can be determined as:

$$Kpv_{pu} = \frac{T_c}{K\sqrt{T_{iv} * T_{eq}}} = \frac{T_c}{a * K * T_{eq}} \tag{5.53}$$

Having found the PI controller gains, the compensated open-loop and closed-loop transfer functions are given as:

$$G_{v,ol}(s) = \frac{1}{a^3 * s^2 * T_{eq}^2} * \left(\frac{1 + a^2 * s * T_{eq}}{1 + s * T_{eq}}\right) \tag{5.54}$$

$$G_{v,cl}(s) = \frac{1 + a^2 * s * T_{eq}}{1 + a^2 * T_{eq} * s + a^3 * T_{eq}^2 * s^2 + a^3 * s^3 * T_{eq}^3} \tag{5.55}$$

The base values and other fundamental parameters are given below. Computation of the remaining parameters, which are applied in determining the controller parameters, is detailed in the MATLAB script A.2.

Parameter	Description	Value
sb	Base apparent power	5kVA
vb_{grid}	Grid-side base voltage	520V
vb_{vsc}	VSC-side base voltage	260V
fb	Base frequency	60Hz
ωb	Base angular frequency	376.99rad/s
f_{sw}	Switching frequency	5kHz
T_a	Delay due to switching	0.3ms
T_{eq}	Equivalent time constant of the inner control loop	0.6ms
Kp_v	Outer loop controller proportional gain	7.67
Ki_v	Outer loop controller integral gain	2129.4

Table 5.2: System parameters

5.2.2 Inner control loop

A block diagram of the inner current control loop is shown in Figure 5.12. Reference can be made to Figure 5.10 as a representation of the controller process to be described. The current controller is responsible for ensuring that the output current tracks the current reference received from the outer grid controller. The PLL takes the grid voltage as input and calculates the rotating phase angle (θ) with which the converter voltage (u_{dq}^*) and the grid voltage are synchronised at the point of interconnection (POI).
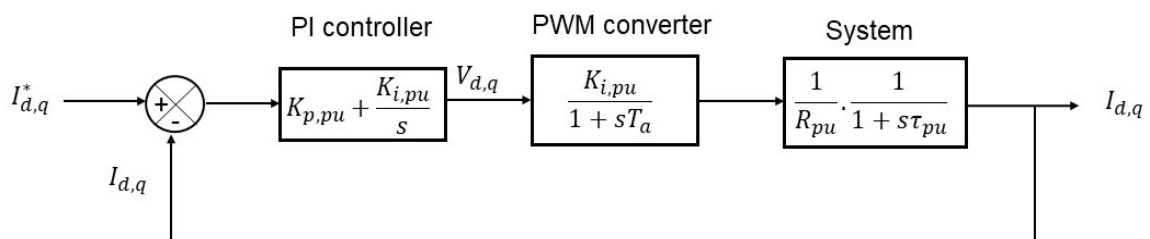

Figure 5.12: Block diagram of the inner control loop [125]

The conversion of the currents in the dq-frame using the 'abc/dq' block, with θ as input, generates DC signals under balanced conditions and full synchronisation, i.e. $dq0$ currents. The dq voltage components (u_d^*, u_q^*) sent to the PWM converter are generated from the processing of the difference/error from comparing the measured and reference currents, i_{dq} and i_{dq}^* by a PI controller. The PWM converter converts the voltage to gating signals for

switching the converter. The PI controller is tuned using the modulus optimum criterion to achieve zero steady-state error and maintain the robustness of the closed-loop system. Figure B.9 shows the simulation model used for the inner current controller. As expected, it is evident that transformation into the dq-frame creates a model which is coupled because of the cross-coupling terms ωLid and ωLiq. With decoupled control of i_d and i_q being the objective, these terms are eliminated using feed-forward terms. It is useful to note that an average voltage reference (U-ref) controlled VSC converter is used in the simulation model; hence no PWM block is implemented. However, digital PWM is assumed.

Non-linearities are mostly neglected during the tuning of the PI controllers. Tuning is carried out using criteria adopted for electric drives [126]. With a scheme involving cascade controllers, control speed is expected to increase towards the inner loop. It is expected that this inner loop is designed to be faster than the outer loop whose controller design has been discussed earlier. The outer loop, on the other hand, is designed for optimum regulation and stability. The inner current control loop is tuned according to the modulus optimum criterion to achieve a quick and straightforward response.

5.2.2.1 Modulus optimum

Modulus optimum (or absolute value optimum criterion) is usually used in tuning the conventional analogue controller of a low-order plant without a time delay. For a controlled system with a dominant time constant and a minor time constant, the control system's standard transfer function is obtained by cancelling out the larger time constant. Also, it is ensured that the closed-loop gain is higher than unity for high frequencies as much as possible [125]. The current controller's open-loop transfer function is given as:

$$Gc,ol = Kp_{pu} * \left(\frac{1 + T_i s}{T_i s}\right) * \frac{1}{1 + T_a s} * \frac{1}{R_{pu}} * \frac{1}{1 + s\tau_{pu}} \tag{5.56}$$

Referring to the equations above, Kp_{pu} and Kpi_{pu} are the proportional and integral gains of the PI controller, respectively. T_i is the PI controller's time constant and τ_{pu} is the system's per unit time constant. With digital pulse-width modulation assumed for this project, T_a is the delay caused by the switching of the power converters. It is calculated based on the switching frequency (f_{sw}) of the converter as:

$$T_a = 1.5 * T_{sw} = \frac{1.5}{f_{sw}} \tag{5.57}$$

Based on the modulus optimum criteria, the parameters for the controller are determined as follows:

$$T_i = \tau_{pu} = \frac{Lt_{pu}}{\omega_b * Rt_{pu}} \tag{5.58}$$

$$Kp_{pu} = \frac{\tau_{pu} * Rt_{pu}}{2 * T_a} = \frac{Lt_{pu}}{\omega_b * 2 * T_a} \tag{5.59}$$

$$Ki_{pu} = \frac{Kp_{pu}}{T_i} = \frac{Rt_{pu}}{2 * T_a} \tag{5.60}$$

The resulting open-loop and closed-loop transfer functions of the system with the controller implemented are:

$$G_{i,ol} = \frac{1}{2 * T_a} * \frac{1}{s(1 + s * T_a)} \tag{5.61}$$

$$G_{i,cl} = \frac{1}{1 + \dfrac{1}{G_{i,ol}}} \tag{5.62}$$

$$G_{i,cl} = \frac{1}{2 * s^2 * T_a^2 + 2 * s * T_a + 1} \tag{5.63}$$

The final system has a natural frequency $\omega_n = 1/T_a\sqrt{2}$ and damping factor $\zeta = 1/\sqrt{2}$. This method is based on simplifying by pole cancellation and optimising the system to an absolute value of 1. The system response always corresponds with the values for ω_n and ζ above. The system can, however, be tuned further to the desired crossover frequency by choosing a total constant gain term from open-loop transfer function to be equal to the desired crossover frequency. The corner frequency is chosen such that it is one or two orders smaller than the switching frequency to avoid interference from switching noise.

5.2.3 Application of tuning methods

For the simulation model of the standalone AC system which has been designed, the following filter parameters in pu have been obtained (total filter inductance, DC bus capacitance, and total filter resistance): $Lt_{pu} = 0.30$, $C_{dc,pu} = 4.25$, and $Rt_{pu} = 0.0094$. The nominal angular frequency (ωb) is 377rad/s. With these parameters, the tuning methods of symmetrical optimum and modulus optimum are used in tuning the controllers. The switching frequency (f_{sw}) is 5kHz as mentioned before. The average time delay (T_a) is therefore $\frac{1.5}{f_{sw}}$.

5.2.3.1 Tuning of the voltage controller using symmetrical optimum

At steady-state, $V_{dc,pu} = V_{d,pu} = 1$; where V_{dc} and V_d are the DC bus voltage and d component of the VSC output voltage, respectively. Choosing $a = 3$, the symmetrical optimum method is used to tune the outer voltage PI controller parameters. The controller gains Kpv_{pu} and Kiv_{pu} are therefore computed as 7.67 and 2129.4, respectively.

The bode plot of the open-loop transfer function of the outer voltage controller presented in Figure 5.13 shows a stable operating limit with a maximum phase margin of 53.1°. This value occurs at a frequency in rad/s of 556.
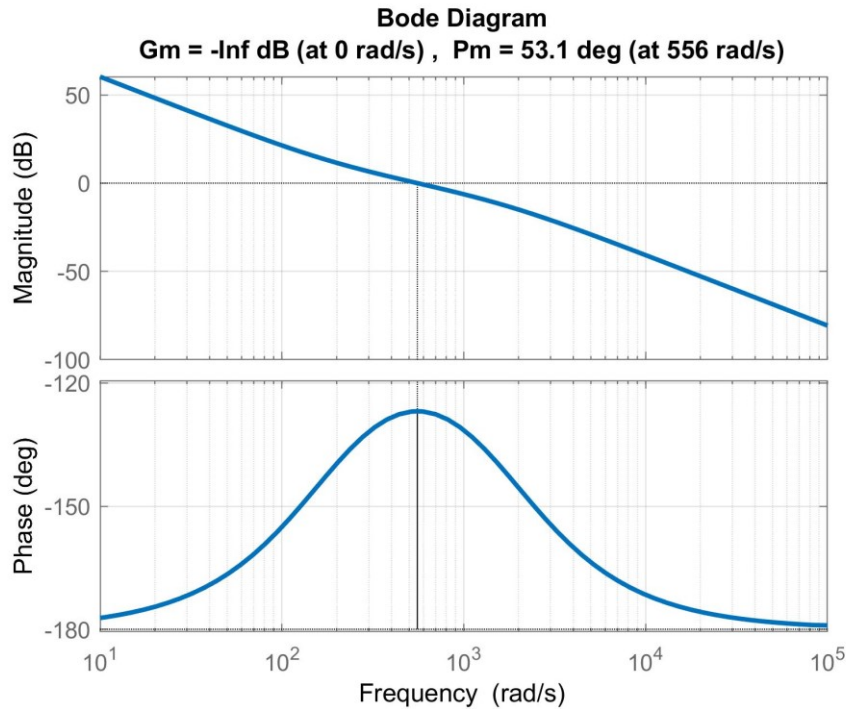
Figure 5.13: Open-loop bode plot of voltage controller transfer function

The controller's step response is shown below. The step response characteristics are a maximum overshoot of 9.49%, a maximum overshoot time of 0.01s, and a settling time of 0.018s.

5.2.3.2 Tuning of the current controller using modulus optimum

Using the modulus optimum criteria, the controller gains obtained are a controller gain (Kp_{pu}) of 1.31 and an integral time constant (T_i) of 0.084. The controller's open-loop transfer function shown in the figure below has a phase margin of 65.5° and an infinite gain margin, giving a stable system, see Figure 5.15. The gain margin occurs at a frequency in rad/s of 1.52k.
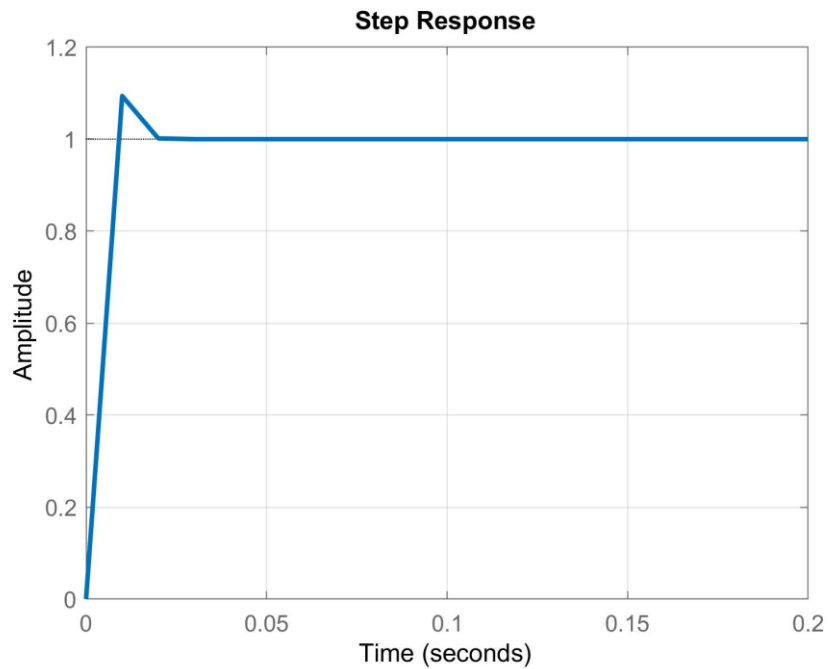
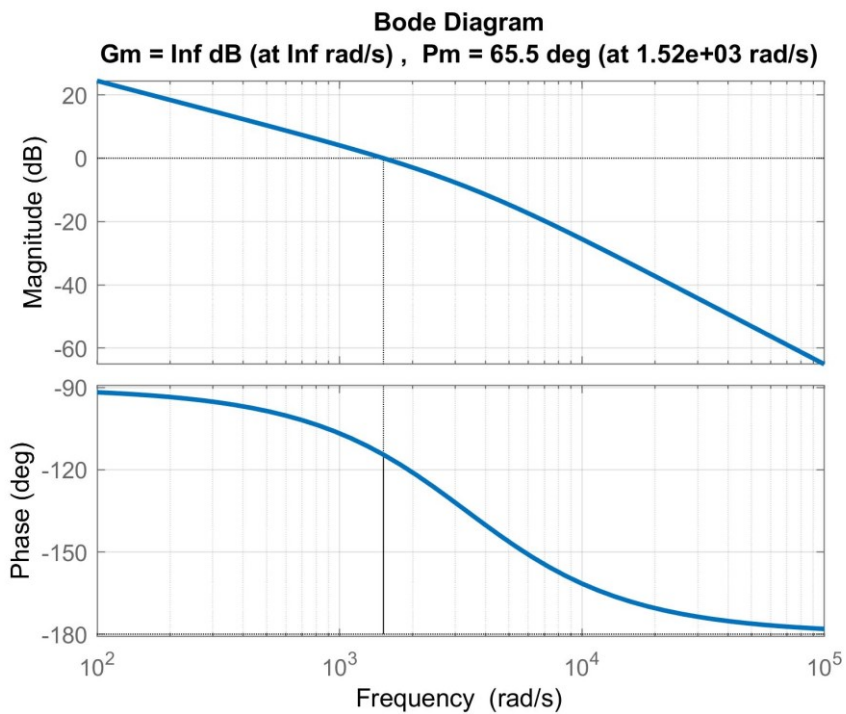**Figure 5.14: Step response of the voltage controller**

Figure 5.15: Open-loop bode plot of the inner current controller

The step response of the closed-loop transfer function of the inner current controller is presented below. The step response characteristics are a maximum overshoot of 4.32%, a maximum overshoot time of 0.0019s, and a settling time of 0.0025s.
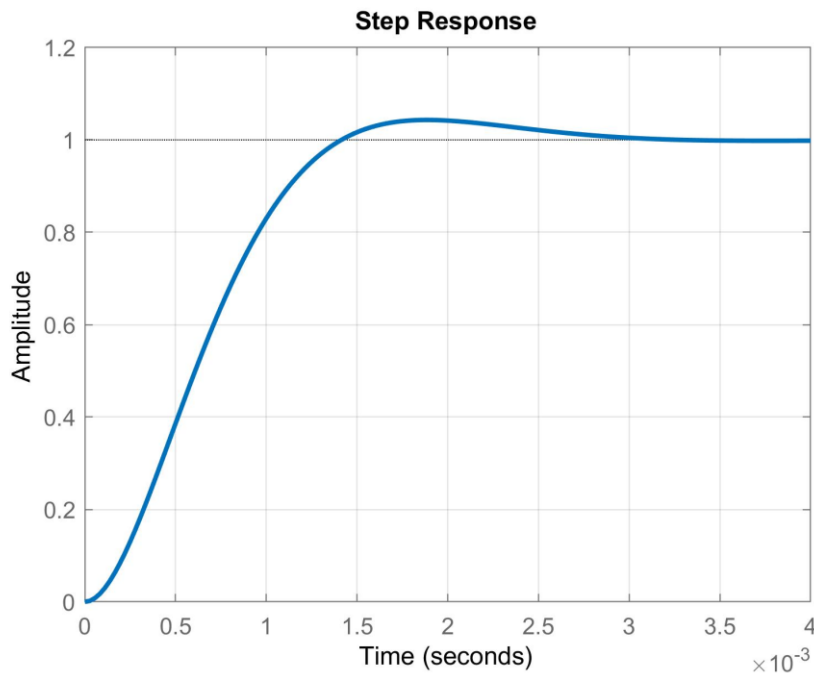
**Figure 5.16: Step response of the current controller**

5.2.4 Verification of 2L-VSC

Now that the two tuning methods have been applied, it is confirmed that the VSC controllers operate within stable regions. The converter's operation in the AC standalone system is verified. As stated earlier, an active power setpoint of 5kW is provided in the outer voltage controller. It is based on this setpoint that the inner current controller current reference is generated.

According to Figure 5.17 (a), the VSC output power follows the reference as is expected with no steady-state error. With a short settling time, the controller is expected to respond to system changes quickly and restore output power within a short time. This observation verifies that the outer voltage loop controller is functioning effectively in giving an accurate current reference to the inner loop. The three-phase voltages and currents are also close to the rated phase-to-phase rated values of the grid. The slight difference from the rated values can be explained to be due to voltage drops in passive elements of the grid.

Since a resistive 3kW load is connected in the AC grid, it is expected that reactive power goes to 0, and this is observed in output grid reactive power. This result corresponds to Figure 5.17 (d), where the dq currents are found to be stable and reach steady state within a short period. i_q goes to zero, following the current reference given to the inner current controller. i_d is expected to be proportional to output active power supplied to the grid.
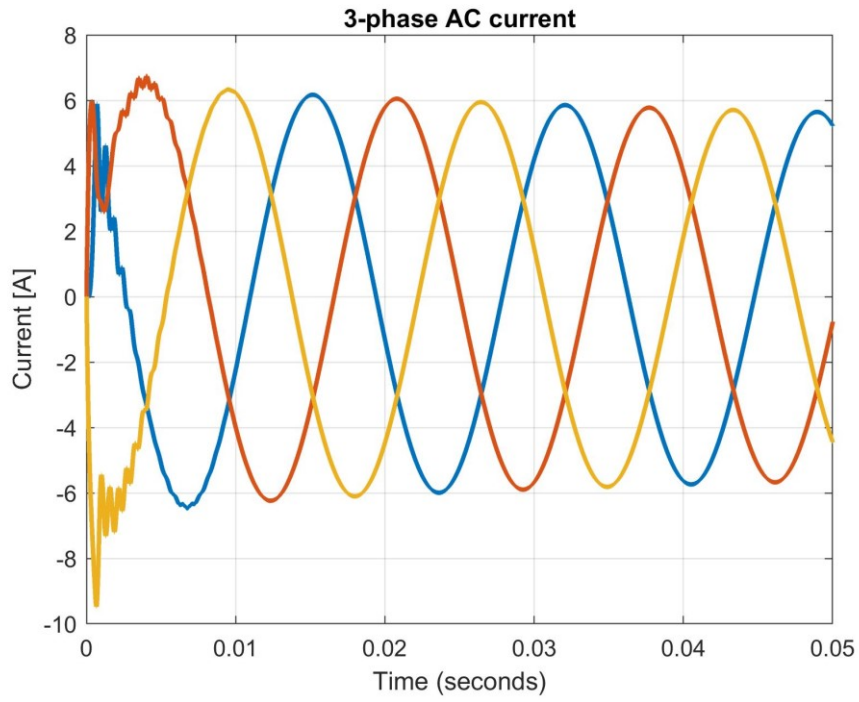
In summary, the 2L-VSC is verified to be functioning to a desirable level based on the design requirements provided.
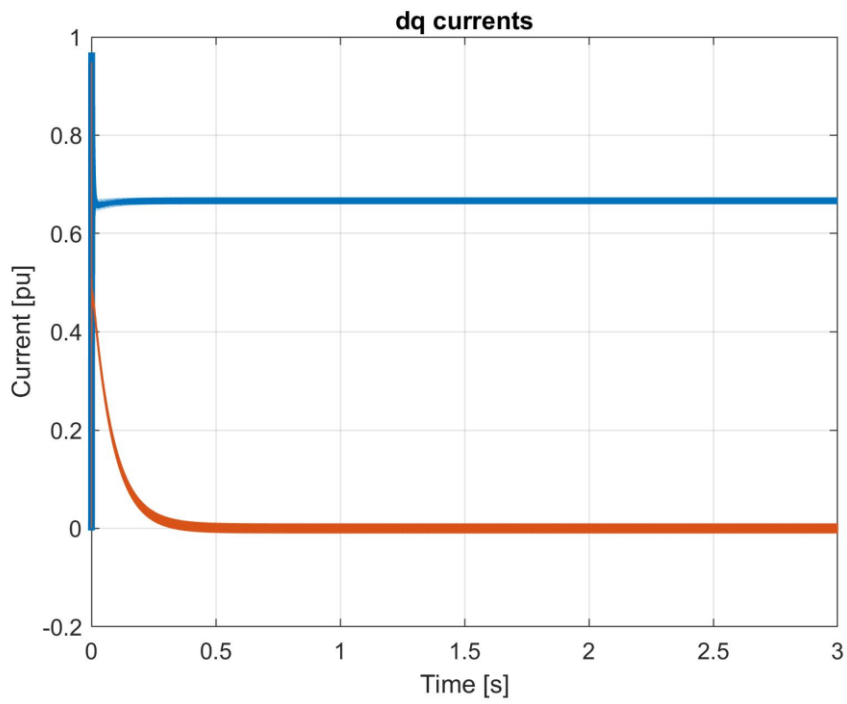
(a)

(b)

71
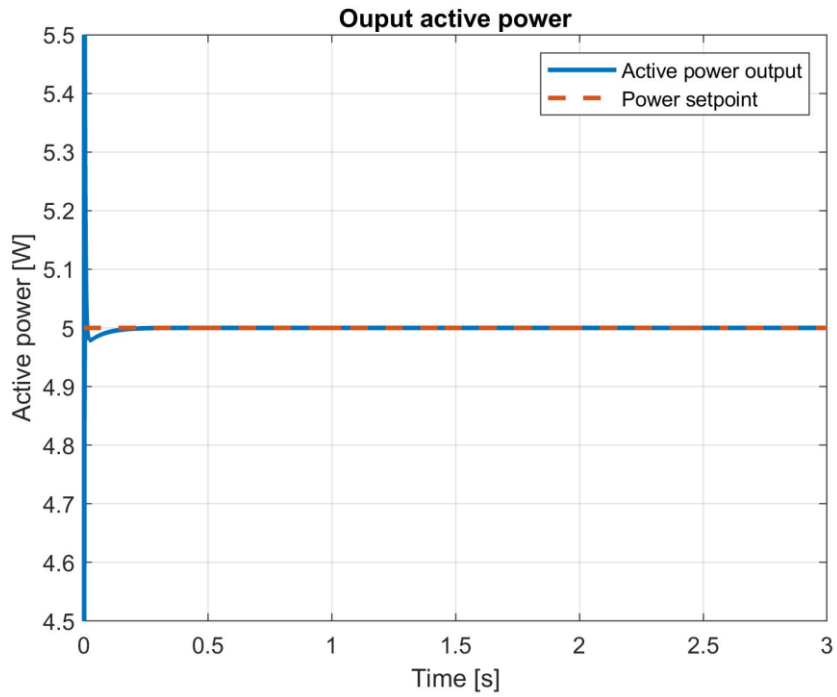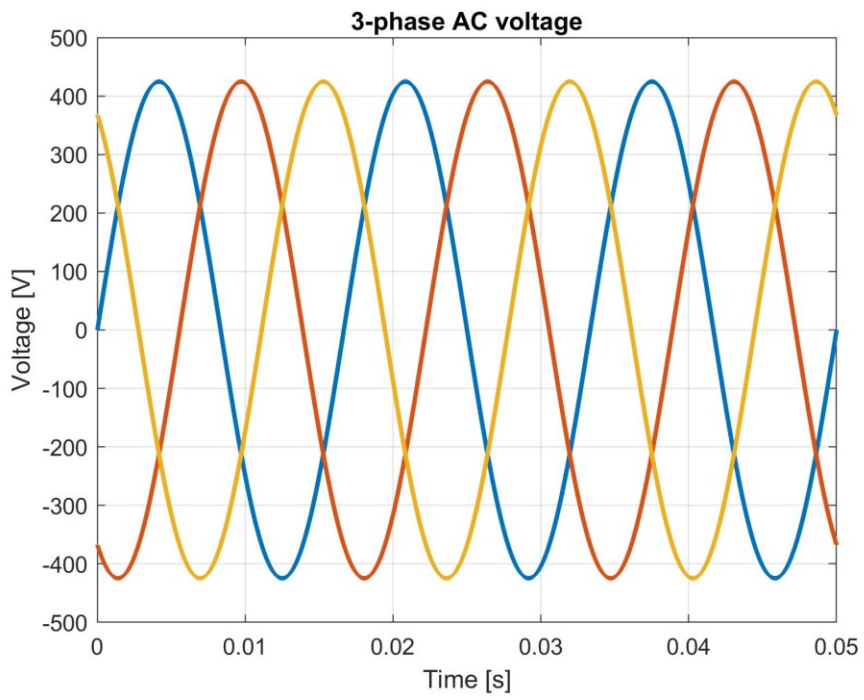
(c)

(d)

Figure 5.17: (a) Output active power to the grid (b) AC grid voltage (c) AC grid current (d) Measured dq currents

6 Comparative study of energy storage

This chapter is a culmination of all the work done throughout this project. It investigates the contribution of hybrid storage to improving voltage stability at the DC bus as compared to a single energy storage system (battery). It is assumed that the performance of the HESS compared with the supercapacitor under the same conditions, produces similar simulation results. Hence the decision to compare the performance only with a battery.

The first performance criterion used in the analyses is load-transient recovery time. This is defined as the time taken for the output voltage, i.e. DC bus voltage, to return and remain within the recovery/settling band (measured in millivolts and volts) around its nominal/steady-state value after a step change in load current. An adequate recovery band to investigate how energy storage improves grid resiliency is 0.25% (=1V) at the nominal DC bus voltage of 400V, for this project. Hence, in the analysis of results, transient recovery time is measured from when the load current step occurs (t=0.5s) until the point where output voltage falls within a settling band +/-1V of 400V (i.e. 399V to 401V).

The second performance criterion used in the analyses is the magnitude of voltage deviation from nominal at the onset of the load current transient. A first step in controlling the magnitude of the DC bus voltage deviation was implemented in Chapter 5 in the design of the bidirectional converter control. The controllers were designed with a maximum voltage deviation (e_v) of 4% (=+/-16V) of nominal DC bus voltage, see MATLAB script A.1. This design limit gives a range of voltage deviation from 384V to 416V. It is observed in the following simulation results that this requirement is fulfilled. In all simulations performed there is no variation of DC bus voltage beyond the maximum deviation limit for the simulated load demands. With this first requirement fulfilled, analysis carried out in this chapter pertinent to voltage magnitude deviation further determines by how much the HESS mitigates voltage deviation relative to a battery.

These two criteria mentioned above suffice to make a complete performance evaluation of energy storage for this project. It is crucial to mitigate voltage deviation as much as possible to avoid the unplanned operation of protection equipment or the damaging system components. Power electronic converters sensitive to high voltage variations can also disconnect the interfacing equipment. Reducing transient recovery time ensures that regular system operation continues within milliseconds of a system transient occurring. Regarding low voltage ride through requirements, the time required for active components to remain connected until the rated operation is restored is reduced.

Based on discussions in previous chapters, it is decided that the DC bus voltage is the system variable of focus for the simulations to be carried out. However, the converter output currents are presented as well to give an idea of their influence on the voltage variations. So far, converters used in both DC and AC standalone systems have been verified to ensure that they operate effectively. The bidirectional DC converters in the DC system are designed with controllers capable of charging and discharging energy storage and principally, regulating DC bus voltage around its nominal value. The supercapacitor storage current controller is given a higher bandwidth of operation, making it absorb high-frequency oscillations following a transient. The battery, on the other hand, has a relatively lower bandwidth of operation; hence it absorbs the low-frequency oscillations and responds

slower than the supercapacitor. The two-level VSC is modelled with suitable controllers as well to ensure output power delivered to the grid follows a given active power setpoint. Its outer and inner control loops were modelled using the symmetrical optimum and modulus optimum methods, respectively. Eventually, the verification of the VSC shows that it supplies rated active and reactive power to the load and other components of the system. It keeps the reactive power or q component of the output current at zero.

The two study cases are a step increase in load demand and a step decrease in load demand. Outputs of simulations are presented and analysed. The effects of passive elements in the DC system on the performance of the energy storage outputs are expected to be different from those caused by AC system components. Therefore, case studies are made for two scenarios: connection in a standalone DC system and connection in a hybrid (DC/AC) system. This way, performances of both storages can be compared for situations when additional non-idealities are present. This is also to investigate the effects of the generation of pulses in the DC bus current when the 2L-VSC draws current. Such pulses have quick edge rates so impose larger transients on the DC bus. Hence, studying both systems gives a better idea of the effects of these additional transients on the energy storage output characteristics. The DC system simulation models used for the battery and HESS are given in Figures B.4 and B.1, respectively. The hybrid system simulation models with battery and HESS are given in Figures B.10 and B.11, respectively.

In carrying out the selected simulations, some system parameters are modified to maintain the stability of the system and give suitable outputs, see MATLAB script A.3. For instance, in the standalone DC system, the DC bus capacitance is increased from its calculated minimum value by a factor of 8 to increase the inertia of the DC bus voltage to withstand transients. However, when this capacitance is used the full system model, it introduces noise in system variables like the d-current and output active power. Hence, a smaller value is chosen for the DC bus capacitance. A change is also made in the power setpoint (P^*) for the 2L-VSC when running simulations of the full system. Using the same base apparent power (S_b) of 5kVA, the power setpoint for carrying out the simulations for this chapter is set to 2.5kVA.

Finally, the methods used in simulating load demand are explained here. For the DC system simulations, a step increase in load demand is simulated by changing the DC load current (I_{dc}) from its rated value of 12.5A to 15A at t=0.5s. Similarly, a step decrease in load demand is simulated using a change in I_{dc} from 12.5A to 10A. In the full DC/AC system, the change in demand is set using a step change in the VSC power setpoint in its outer controller. For a step increase in load demand, P^* is changed from 2.5kW to 3kW. For a step decrease in load demand, it is changed from 2.5kW to 2kW. The use of lower step changes in power setpoint is to avoid the generation of excessive starting transient pulses by the VSC. It is observed that the steps in load current using these setpoints are not as large as in the DC system simulations; however, the objective of determining and analysing the voltage magnitude deviation and recovery time is achieved. The total simulation time is all the cases is $t = 1$s.

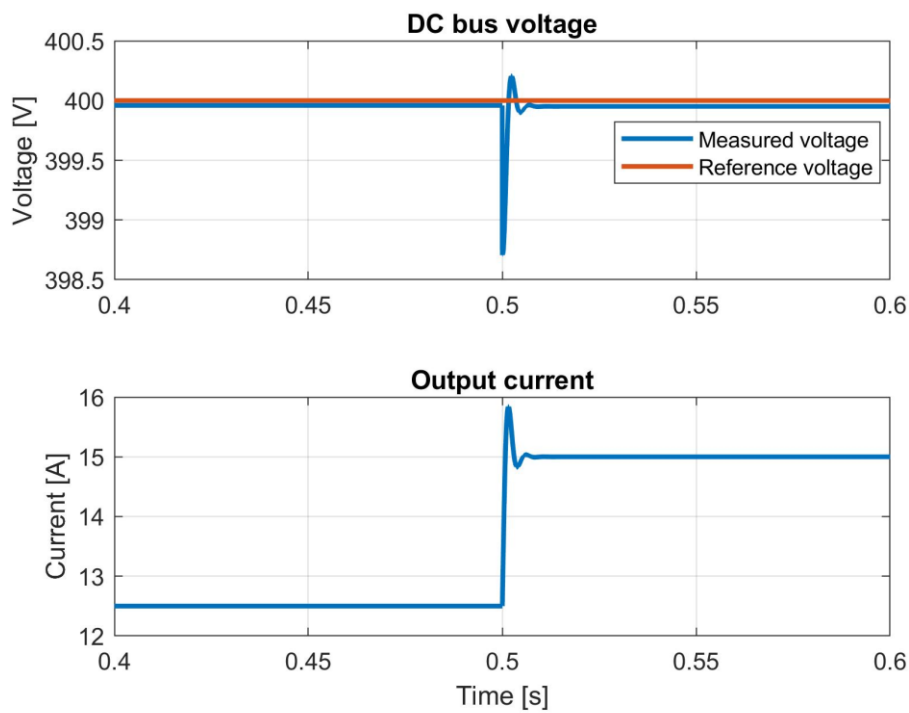After a simulation result is presented for battery and HESS for a given scenario, an analysis is made directly after to facilitate referral to the simulation results. All numerical results provided in the analyses are determined in the Simulink scopes using measurement tools available.

6.1 Step increase in load demand

6.1.1 Connection to DC grid
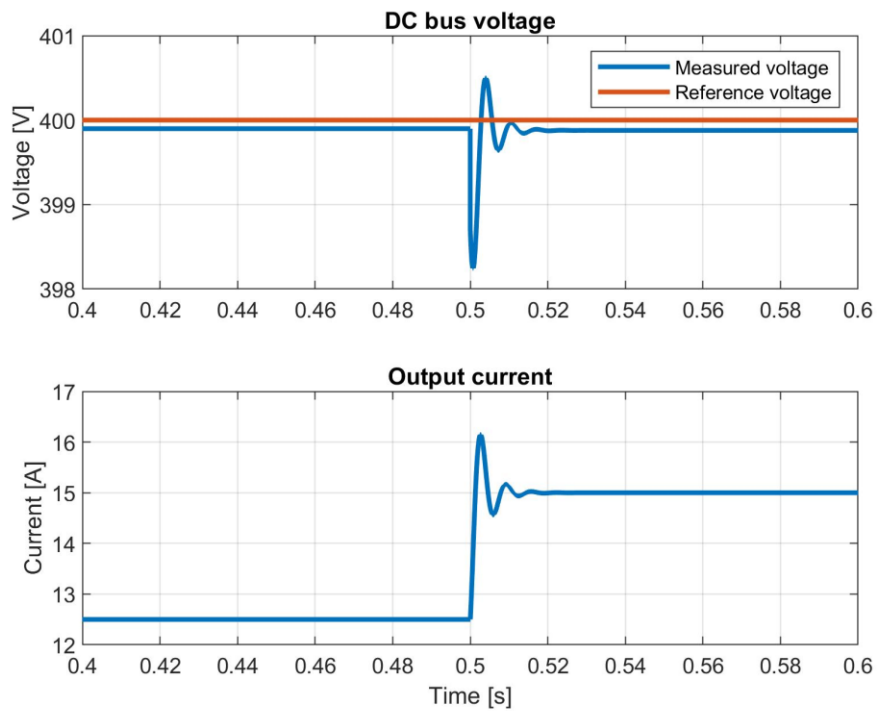
(a)

(b)
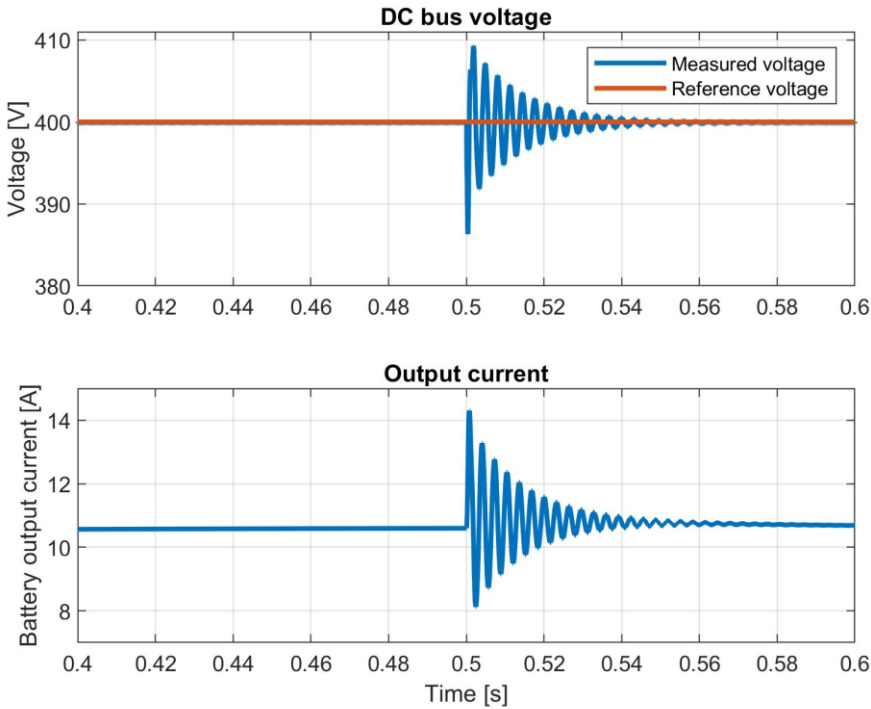
Figure 6.1: (a) Battery (b) HESS

The results presented above in Figure 6.1 show the responses of the two energy storages during a step increase in load demand in the DC system. A sudden increase in load demand results in an immediate proportional decrease in DC bus voltage.

In the battery response of Figure 6.1(a), following a load transient at $t=0.5$s, the DC bus voltage returns to the settling band at approximately $t=0.512$s. This period gives a load transient recovery time of 0.012 seconds. The magnitude of the voltage at the instant of the load change is 398.3V—giving a voltage deviation of 0.425%.

For the HESS response, on the other hand, in Figure 6.1(b), following a load transient at $t=0.5$s, the DC bus voltage returns to the settling band at $t=0.506$s. This gives a transient recovery time of about 0.006 seconds. The magnitude of the voltage at the instant of the load change is 398.7V—representing a deviation of 0.325%.

The overshoot of output converter current of the HESS is lower than that of the battery by a small margin.

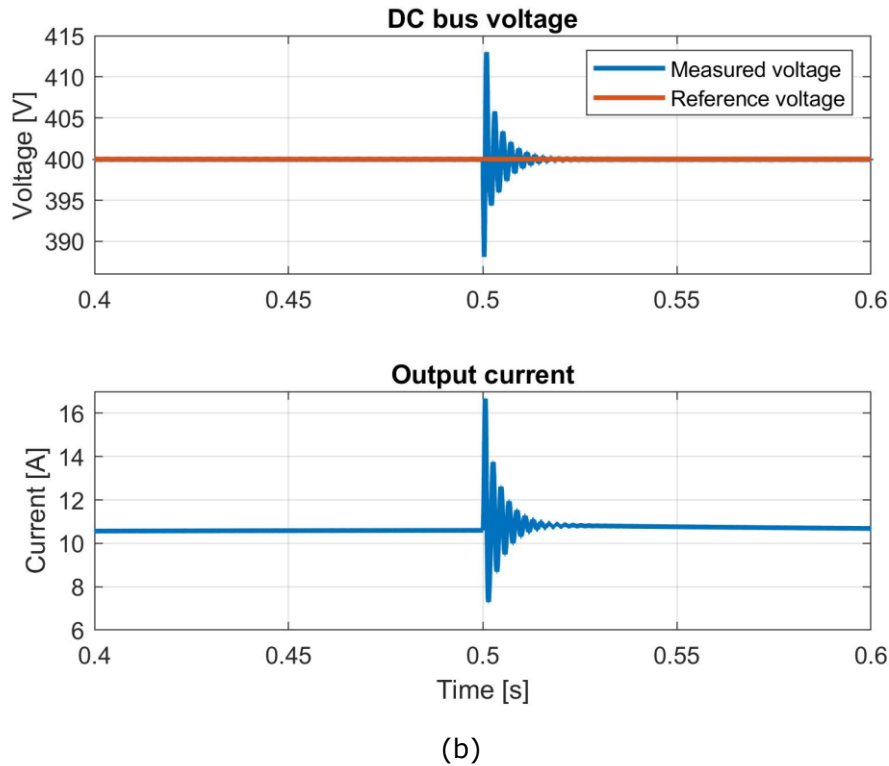## 6.1.2 Connection to 2L-VSC and AC grid

(a)

(b)

Figure 6.2: (a) Battery (b) HESS

The results presented above in Figure 6.2 above show the responses of the two energy storages during a step increase in load demand when connected to the full DC/AC system. Once again, a sudden increase in load demand results in a proportional decrease in DC bus voltage before it is restored.

In the battery response of Figure 6.2(a), following a load transient at t=0.5s, the DC bus voltage returns to the settling band at t=0.575s. This gives a relatively higher transient recovery time of 0.075 seconds as compared to the recovery time in the DC system. The magnitude of the voltage at the instant the load demand increases is 386.3V—giving a deviation of 3.43%.

For the HESS response in Figure 6.1(b), following a load transient at t=0.5s, the DC bus voltage returns to the settling band at t=0.527s. This gives a transient recovery time of 0.027 seconds, also relatively higher than that in the DC system. The magnitude of the voltage at the instant of the load change is 388V—giving a deviation of 3%.

6.2 Step decrease in load demand

6.2.1 Connection to DC grid
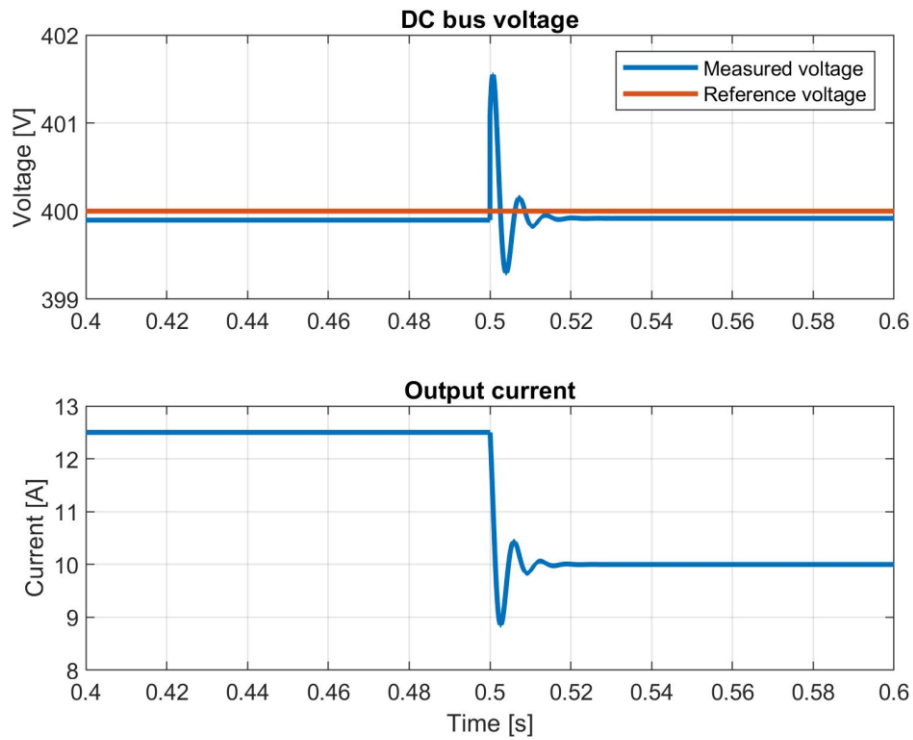
(a)

(b)

Figure 6.3: (a) Battery (b) HESS

The results in Figure 6.3 are the responses of the two energy storages during a step decrease in load demand for the DC system. A sudden decrease in load demand results in a proportional increase in DC bus voltage.

In the battery response of Figure 6.3(a), following a load transient at $t=0.5$s, the DC bus voltage returns to the settling band at $t=0.514$s. This gives a transient recovery time of 0.014 seconds, higher than the step recovery time for the step increase. The magnitude of the increased voltage at the instant of the load reduction is 401.6V—giving a deviation of 0.4%.

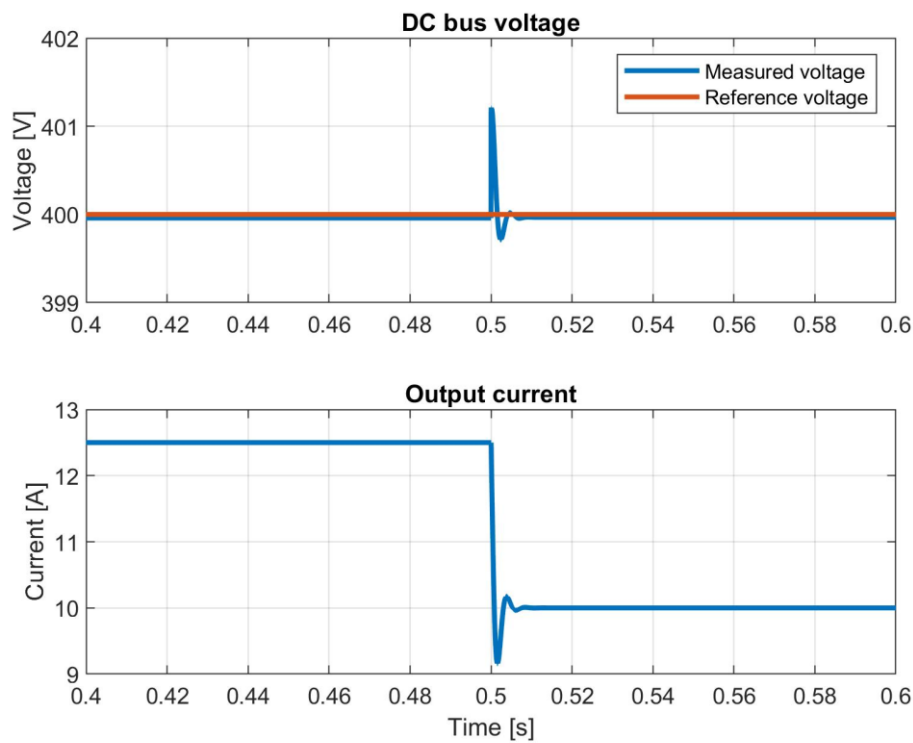For the HESS response, on the other hand, in Figure 6.3(b), following a load transient at $t=0.5$s, the DC bus voltage returns to the settling band at $t=0.504$s. This gives a transient recovery time of 0.004 seconds. The magnitude of the voltage at the instant of the load change is 401.2V—giving a deviation of 0.3%.

Again, the overshoot of the HESS converter output current is observed to be lower than that of the battery converter.

6.2.2 Connection to 2L-VSC and AC grid
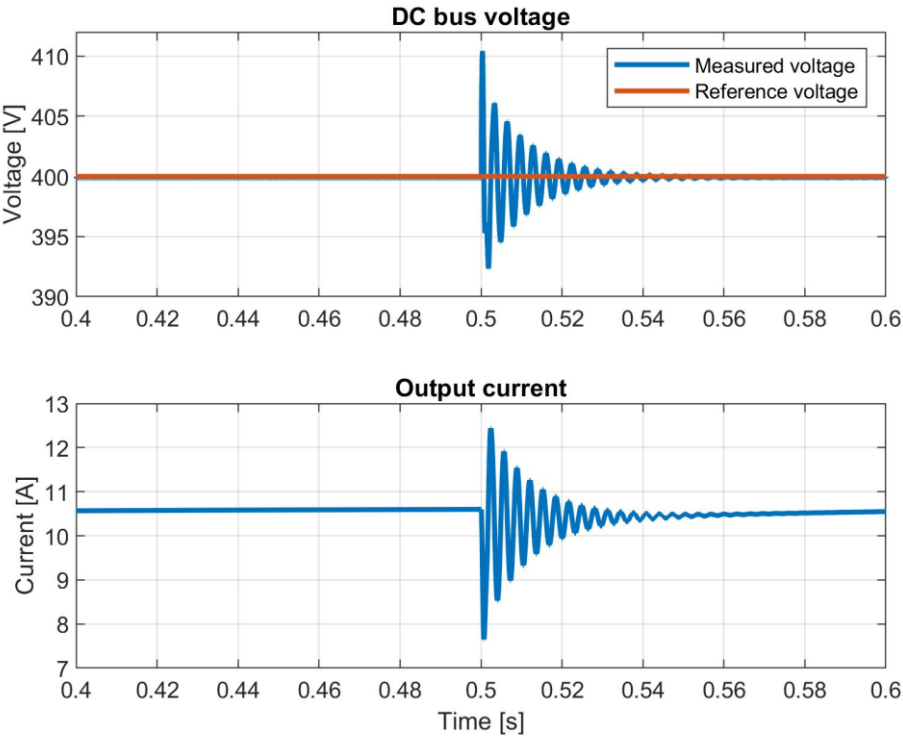

(a)

(b)

Figure 6.4: (a) Battery (b) HESS

Figure 6.4 above shows the responses of the two energy storages during a step decrease in load demand for the full system. A sudden decrease in load demand results in a proportional increase in DC bus voltage.

In the battery response of Figure 6.4(a), following a load transient at t=0.5s, the DC bus voltage returns to the settling band at t=0.547s. This gives a transient recovery time of 0.047 seconds. The magnitude of the increased voltage at the instant of the load reduction is 410.47V—showing a deviation of 2.62%.
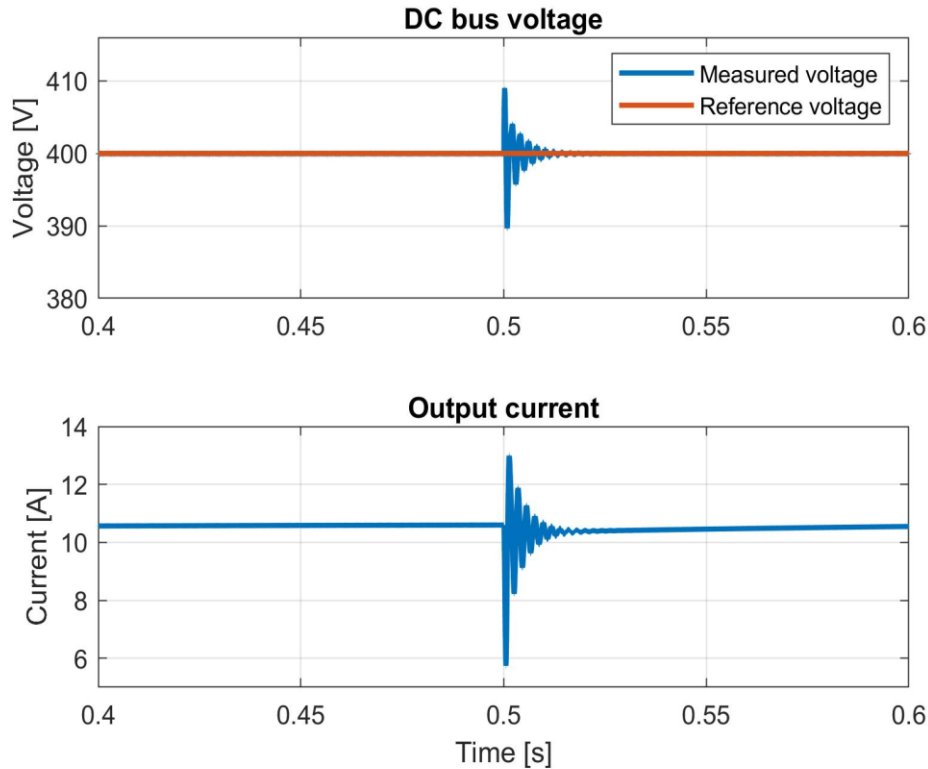
For the HESS response in Figure 6.4(b), following a load transient at t=0.5s, the DC bus voltage returns to the settling band at t=0.520s. This gives a transient recovery time of 0.02 seconds. The magnitude of the voltage at the instant of the load change is 409.1V— giving a deviation of 2.28%.

6.3 Summary and discussion

6.3.1 DC system simulations

Step increase in load demand		
	Battery	**HESS**
Transient recovery time[s]	0.012	0.006
Deviation [%]	0.425	0.325

Step decrease in load demand		
	Battery	**HESS**
Transient recovery time[s]	0.014	0.004
Deviation [%]	0.4	0.3

Table 6.1: Comparison of energy storage responses for (a) Load increase (b) Load decrease in the DC system

6.3.2 Full DC/AC system simulations

Step increase in load demand		
	Battery	**HESS**
Transient recovery time[s]	0.075	0.027
Deviation [%]	3.43	3

Step decrease in load demand		
	Battery	**HESS**
Transient recovery time[s]	0.047	0.02
Deviation [%]	2.62	2.28

Table 6.2: Comparison of energy storage responses for (a) Load increase (b) Load decrease in the DC/AC hybrid system

The results obtained from the simulations have been analysed and tabulated in Tables 6.1 and 6.2 above. In both scenarios, it is observed that the grids with hybrid storage as a DC source are more resilient. They have shorter recovery times making their DC bus voltages

return to the steady-state faster, and their magnitudes of voltage deviation are relatively low. It is concluded that the hybrid energy storage restores the DC bus voltage to nominal within a period shorter than single energy storage.

As expected in the hybrid system with the VSC, voltage magnitude deviations are higher, and the transient recovery period takes longer due to the additional complexity of the system. However, on another scope, it is observed that voltage deviation for both battery and HESS does not go beyond the design limit for the DC converters (4%). The maximum observed deviation from the simulations is 3.43%.

However, should the current load demands given from the setpoint values increase or decrease further, the deviations are likely to go beyond the maximum limits. Another observation is that the DC bus voltage now pulsates during the occurrence of a load step change, as explained earlier. This emphasises the need to design the energy storage converter controllers to be more robust and capable of withstanding heavy transients due to non-idealities of AC system components in a more complex system.

This idea of keeping voltage deviation as minimal as possible is to avoid the effect of voltage variation on operating characteristics of other power system components such as induction motors and protection systems. It is also to keep protection equipment and power electronic converters from switching off unexpectedly to isolate sections of the grid.

7 Overview of limitations

Simulations made are purposely for investigating the contribution of a HESS in restoring system DC bus voltage during sudden system changes/transients, as compared to a battery. Other effects such as power losses and switching harmonics are not of concern in the presented results, although the effects of these phenomena are noticed. The 3-phase VSC used for this study is an average model, and when used in the study of power system dynamics, switching losses, harmonics, and fast switching currents are neglected. Digital pulse-width modulation is assumed; thus, the voltage output of the inner current controller (V_{dq}) is directly sent to the inverter. However, implementing a 2-level PWM generator would provide more practical results. A PWM converter can be used should one require a practical switching response behaviour.

Non-idealities of the DC/DC converter such as winding resistances; switch, capacitor, and inductor voltage drop; and power losses due to switching are not prioritised in the design of the converter for this project. Including a discussion or focus on these operating characteristics will involve the further design of the DC/DC converter such that its performance is improved to mitigate losses due to heating, switching, among others.

Control of the hybrid storage is designed for connection to the DC bus of the power system via a bidirectional DC/DC converter. As such, its purpose in regulating DC bus voltage is directly translated to active power control in the AC grid using the d current. An advanced energy management system (EMS) is not needed or implemented in this project. This would have been necessary if the HESS had been connected directly to the AC system through a voltage source inverter rather than a DC/DC converter. Also, during the converter controller modelling and design, factors such as cost and sizing were not considered. If factored in, these considerations would have influenced the design of the passive components and operating characteristics of the converters.

The transition between the two modes of MG connection is not considered because of the focus on a remote area system with no grid connection. A study of modes of operation would require the design of the grid controller to regulate frequency and voltage of the MG with a microgrid management system (MMS) providing interconnected control. The transition from grid-connected to isolated modes, which is monitored by the MMS to switch between fixed power and frequency-voltage, is not considered in the convertor modelling.

8 Conclusions and further work

8.1 Conclusions

According to the objective of this master's thesis project to investigate the potential of energy storage to increase grid resiliency, various tasks were performed. First among these was reviewing current developments in the offshore energy industry about renewable energy integration and expansion of power transmission and distribution. One major point taken from this review is that there is an increasing growth in renewable energy integration (mainly wind) in offshore systems. This development is accompanied by challenges such as local and system-wide impacts on system variables for which measures must be taken to alleviate deterioration in power supply reliability and quality. Most of these impacts have been determined to affect the voltage and frequency of the power system, mostly. Among the measures identified to maintain the stability of the grid, energy storage has been considered as an effective solution. In better understanding islanded offshore energy systems, a brief review of the setup and characteristics of microgrids is made.

Next, an in-depth review of energy storage technologies reveals that different energy technologies possess different levels of properties like energy density, discharge rate, lifetime, and power density. This makes it impossible to utilise a single technology in several different applications; making them suitable for only specific purposes. The choice of energy storage for an application depends on the designer's requirements and the application for which energy storage is needed. This discussion then led to an understanding of the different grid support applications for which storage technologies are needed: voltage control support, oscillation damping, load following, among others. A number of these applications are relevant to offshore energy systems because these systems have lower grid inertia making their system variables prone to disturbances. The presence of intermittent renewable power sources and energy-intensive load demand signifies the importance of energy storage to contribute to maintaining system stability. On finally comparing the technical and operational properties of a few widely known and commonly used storage technologies, it is determined that the lithium-ion battery and supercapacitor are characterised by the highest energy density and power density, respectively. These properties make them the best candidates for hybridisation and use in a short duration energy system application for grid voltage support. With different hybrid energy storage topologies available to choose from, the full active topology is recommended since full controllability of the HESS storage elements is required. Implementing the parallel full active topology isolates the energy storage elements from the grid bus and decouples them. Employing the right control strategy enhances the volumetric efficiency of the HESS and increases the lifetime of the battery by diverting peak fluctuating load changes to the supercapacitors. Though more expensive and sophisticated compared to the two other topologies, implementation of this topology eventually minimises operational costs of the HESS and provides better performance of the system.

At the end of the comparative study of performances of the battery and hybrid energy storage, it is first shown that connection of energy storage to the grid inherently increases the grid's resiliency against variations in generation and load demand. Secondly, implementing a well thought out hybridisation of two (or more) energy storage elements

to provide grid support has its advantages over utilising single energy storage whose properties or capabilities are limited. The drawbacks of individual storages are counterbalanced by higher levels of the same characteristic in the complementary energy storage. Such a system performs effectively in response to transients or disturbances since it possesses high levels of the desired properties. Therefore, with hybrid energy storage having the appropriate constituent elements and an efficient power electronic interface, better control of output can be achieved.

The time-scale-based control of a HESS has been identified as an effective strategy both in design and life cycle maintenance. For a HESS having a battery and supercapacitor as constituent elements, the battery responds to long-term power demands hence reducing the frequency of its charge and discharge cycles. The supercapacitor acts only to compensate peak and short-period transients. It is finally observed and proven that implementing a well-designed hybrid energy storage control approach has the potential of mitigating the effects of transients on system bus voltage to a desirable level.

As a conclusion to work done for this master's thesis, it is established that energy storage has the potential to increase grid resiliency against variations in system load demand. In going further to adopt a more advanced configuration such as hybridisation makes the energy storage more effective in providing grid support, as shown in the comparative performance evaluation.

8.2 Proposals for further work

Technology-specific models of battery and supercapacitor can be substituted for the DC voltage sources to provide more realistic simulations. Such a modification introduces the physical characteristics and non-idealities of the storage devices. It gives an overview of the nature of the response from these storage devices on a more practical scope. It would be interesting to proceed further in the design process by determining appropriate values of parameters like capacity, response time, and discharge rate based on the type of application.

Another control strategy that can be employed for the HESS is designing the supercapacitor converter controller to be the primary regulator for the DC bus voltage. The voltage control of the battery will then depend on the level of supercapacitor voltage during its discharge period. That is, the battery converter controller continuously measures the supercapacitor voltage as it supplies the DC bus. Based on the difference between the instantaneous supercapacitor voltage and its reference voltage, the battery's reference current is generated using a PI controller. Therefore, the supercapacitor immediately responds to a change in demand and maintains power balance due to its very high bandwidth of operation. Only after this operation will the battery respond to restore supercapacitor voltage to its rated value. The battery converter control can also be designed to supplement uncompensated power from the supercapacitor. For a control scheme such as this, the only perturbation is the load current.

The proposed energy management strategy implemented in this project can be implemented in a more complex system with a distributed generation (DG) unit (e.g. wind

turbine, fuel cell, PV unit) connected in parallel to the HESS. Maximum power point tracking (MPPT) algorithm is implemented to ensure maximum power extraction from the DG source using a unidirectional DC/DC boost converter. Power generation from the primary power source is therefore incorporated in the energy management strategy using the same idea of ensuring equal power flow in and out of the common DC bus. The response of the HESS to step increases and decreases in the main power source supply are additional cases of interest. This proposal provides a basis to investigate how energy storage provides grid support against the intermittency of renewable sources. The variations in source input (for instance wind speed or solar radiation) can be made fast and random during the simulations to determine the robustness of the HESS control strategy.

The distributed controller configuration for an ESS for applications in a standalone energy system is not covered in this work. Among the possible control strategies for an ES, the decentralised strategy is implemented because it provides a simple method to control the converters and eliminates the need for communication with other controllers. The centralised control strategy, which requires communication architectures using a centralised controller, is not considered due to its complexity and the possibility of error. It could be possible to implement a centralised controller which coordinates the operations of the DC/DC converters of the HESS and the 2L-VSC. The impacts on performance, whether positive or negative, of using this control system can then be analysed alongside the decentralised strategy of the HESS used in this project.

Dynamic stability studies can be carried out also to assess the effectiveness of a distributed configuration of energy storage. As observed in this project, the hybrid energy storage connected to a common DC bus gives the advantage of a combined storage system over a single storage device. Application of a distributed configuration of ES comprising batteries, supercapacitors, or batteries and supercapacitors can be studied. Following a planned dispersion strategy, the storage devices can be connected at selected vantage points within the power system grid to compensate for various system variations. One can then determine if the hybrid storage is still as effective compared to the distributed units.

In this project, both battery and supercapacitor produce power when the grid is operational and respond based on the control bandwidths assigned to them. It would be interesting to modify the control of the HESS by implementing a lowpass filter to generate the battery reference current from the total output reference current of the outer voltage controller. The parameters of the filter can be set such that the supercapacitor remains inactive during steady-state operation with no power output until a load or source step change is detected. This strategy allows for the supercapacitor to compensate for only high-frequency oscillations and return to zero output after steady state is reached. The battery remains in operation supplying the rated output power.

Bibliography

[1]   ABB, Oil and Gas Production Handbook: An Introduction to Oil and Gas Production, Transport, Refining, and Petrochemical Industry, Oslo: ABB Oil and Gas, 2013.

[2]   L. Riboldi and L. O. Nord, "Concepts for Lifetime Efficient Supply of Power and Heat to Offshore Installations in the North Sea," *Energy Conversion and Management,* vol. 148, pp. 860-875, 2017.

[3]   K. Das, F. Guo, E. Nuno and N. Cutululis, "Frequency Stability of Power System with Large Share of Wind Power under Storm Conditions," *Journal of Modern Power Systems and Clean Energy,* vol. 8, no. 2, pp. 219-228, 2020.

[4]   J. M. Guerrero, J. C. Vasquez, J. Matas, L. G. de Vicuna and M. Castilla, "Hierarchical Control of Droop-Controlled AC and DC Microgrids--A General Approach Toward Standardization," *IEEE Transactions on Industrial Electronics,* vol. 58, no. 1, pp. 158-172, 2011.

[5]   N. Rezaei and M. Kalantar, "Hierarchical Energy and Frequency Security Pricing in a Smart Microgrid: An Equilibrium-inspired Epsilon Constraint Based Multi-objective Decision Making Approach," *Energy Conversion and Management,* vol. 98, pp. 533-543, 2015.

[6]   W. He, K. Uhlen, M. Hadiyah, Z. Chen, G. Shi and E. del Rio, "Case Study of Integrating an Offshore Wind Farm with Offshore Oil and Gas Platforms and with an Onshore Electric Grid," *Journal of Renewable Energy,* pp. 1-10, 2013.

[7]   Norwegian Petroleum Directorate, "Facts: Fields," [Online]. Available: https://www.norskpetroleum.no/en/facts/field/. [Accessed 11 May 2020].

[8]   Norwegian Petroleum Directorate, "Environment and Technology: Emissions to Air," [Online]. Available: https://www.norskpetroleum.no/en/environment-and-technology/emissions-to-air/. [Accessed 11 May, 2020].

[9]   M. Hyttinen, J.-O. Lamell and T. Nestli, "New Application of Voltage Source Converter (VSC) HVDC To Be Installed on the Gas Platform Troll A," in *CIGRE Conference*, Paris, 2004.

[10]   M. Korpas, L. Warland, W. He and J. O. Tande, "A Case-study on Offshore Wind Power Supply to Rigs," in *DeepWind*, Trondheim, 2012.

[11]   M. Korpas, L. Warland, W. He and J. O. Tande, "A Case-Study on Offshore Wind Power Supply to Oil and Gas Rigs," in *DeepWind*, Trondheim, 2012.

[12]   R. Itiki, S. G. Di Santo, C. Itiki, M. Manjrekar and B. H. Chowdhury, "A Comprehensive Review and Proposed Architecture for Offshore Power System," *Electrical Power and Energy Systems,* vol. 111, pp. 79-92, 2019.

[13]   World Wind Energy Association (WWEA), "Worldwide wind power capacity," WWEA, Bonn, 2019.

[14]   WindEurope, "Offshore Wind in Europe," WindEurope, Brussels, 2020.

[15]   The European Wind Energy Association, "Oceans of Opportunity: Harnessing Europe's Largest Domestic Energy Resource," Brussels, 2009.

[16]   P. Higgins and A. Foley, "The Evolution of Offshore Wind Power in the United Kingdom," *Renewable and Sustainable Energy Reviews,* vol. 37, pp. 599-612, 2014.

[17] J. V. Lamy and I. L. Azevedo, "Do Tidal Stream Energy Projects Offer More Value than Offshore Wind Farms? A Case Study in the United Kingdom," *Energy Policy,* vol. 113, pp. 28-40, 2018.

[18] A. Sahu, N. Yadav and K. Sudhakar, "Floating Photovoltaic Power Plant: A Review," *Renewable and Sustainable Energy Reviews,* vol. 66, pp. 815-824, 2016.

[19] C. Perez-Collazo, D. Greaves and G. Iglesias, "A Review of Combined Wave and Offshore Wind Energy," *Renewable and Sustainable Energy Reviews,* vol. 42, pp. 141-153, 2015.

[20] R. Cazzaniga, M. Cicu, M. Rosa-Clot, P. Rosa-Clot, G. M. Tina and C. Ventura, "Compressed Air Energy Storage Integrated with Floating Photovoltaic Plant," *Journal of Energy Storage,* vol. 13, pp. 48-57, 2017.

[21] J. G. Slootweg, "Wind Power: Modelling and Impact on Power System Dynamics," TU Delft, Delft, 2003.

[22] O. Anaya-Lara, D. Campos-Gaona, E. Moreno-Goytia and G. Adam, Offshore Wind Energy Generation, Chichester: Wiley, 2014.

[23] Union for the Co-ordination of Transmission of Electricity, "Integrating Wind Power in the European Power Systems-Prerequisites for Successful and Organic Growth," Brussels, 2004.

[24] IEEE Standards Association, "IEEE Standard for the Specification of Microgrid Controllers," IEEE, New York, 2017.

[25] F. Sissine, "DOE's Office Of Electricity Delivery And Energy Reliability (OE): A Primer, With Appropriations For Fy2016," *Current Politics and Economics of the United States, Canada and Mexico,* vol. 19, no. 2, 2017.

[26] R. Lasseter, A. Akhil, C. Marnay, J. Stephens, J. Dagle, R. Guttromson, A. S. Meliopoulous, R. Yinger and J. Eto, "Integration of Distributed Energy Resources: The CERTS Microgrid Concept," Berkeley, 2002.

[27] R. H. Lasseter, "MicroGrids," in *IEEE Power Engineering Society Winter Meeting*, New York, 2002.

[28] M. S. Mahmoud, S. A. Hussain and M. A. Abido, "Modelling and Control of Microgrid: An Overview," *Journal of the Franklin Institute,* vol. 351, pp. 2822-2859, 2014.

[29] M. Abedi, G. B. Gharehpetian and K. Arani, "Review of Energy Storage Systems Control Methods in Microgrids," *Electrical Power and Energy Systems,* vol. 107, pp. 745-757, 2019.

[30] D. Pudjianto, G. Strbac, F. van Oberbeeke, A. I. Androutsos, Z. Larrabe and J. T. Saraiva, "Investigation of Regulatory, Commercial, Economic and Environmental Issues in Microgrids," in *International Conference on Future Power Systems*, Amsterdam, 2005.

[31] A. Llaria, O. Curea, J. Jimenez and H. Camblong, "Survey on Microgrids: Unplanned Islanding and Related Inverter Control Techniques," *Renewable Energy,* vol. 36, no. 8, pp. 2052-2061, 2011.

[32] I. S. Bae and J. O. Kim, "Reliability Evaluation of Customers in a Microgrid," *IEEE Transactions on Power Systems,* vol. 23, no. 3, pp. 1416-1422, 2008.

[33] T. Masuta, J. G. da Silva, F. H. Ootake and A. Murata, "Application of Battery Energy Storage System to Power System Operation for Reduction in PV Curtailment Based on Few-hours-ahead PV Forecast," in *IEEE International Conference on Power System Technology (POWERCON)*, Wollongong, 2016.

[34] M. Vasiladiotis and A. Rufer, "A Modular Multiport Power Electronic Transformer With Integrated Split Battery Energy Storage for Versatile Ultrafast EV Charging Stations," in *IEEE Transactions on Industrial Electronics*, 2014.

[35] M. Beaudin, H. Zareipour, A. Schellenbergable and W. Rosehart, "Energy Storage for Mitigating the Variability of Renewable Electricity Sources," *Energy for Sustainable Development,* vol. 14, pp. 302-314, 2010.

[36] H. Ibrahim, A. Ilinca and J. Perron, "Energy Storage Systems—Characteristics and Comparisons," *Renewable and Sustainable Energy Reviews,* vol. 12, pp. 1221-1250, 2008.

[37] W. F. Pickard, A. Q. Shen and N. J. Hansing, "Parking the Power: Strategies and Physical Limitations for Bulk Energy Storage in Supply-demand Matching on a Grid Whose Input Power is Provided by Intermittent Sources," *Renewable and Sustainable Energy Reviews,* vol. 13, pp. 1934-1945, 2009.

[38] L. Freris and D. Infield, Renewable Energy in Power Systems, Jon Wiley & Sons, 2008.

[39] H. R. Baghaee, M. Mirsalam, G. B. Gharehpetian and H. A. Talebi, "Reliability/Cost-based Multi-objective Pareto Optimal Design of Stand-alone Wind/PV/FC Generation Microgrid System," *Energy,* vol. 115, pp. 1022-1041, 2016.

[40] F. Diaz-Gonzalez, A. Sumper, O. Gomis-Bellmunt and R. Villafafila-Robles, "A Review of Energy Storage Technologies for Wind Power Applications," *Renewable and Sustainable Energy Reviews,* vol. 16, pp. 2154-2171, 2012.

[41] S. E. Kazogoklu, "Short Term Energy Storage on Grid," *Journal of Undergraduate Research,* vol. 9, pp. 21-24, 2016.

[42] V. Fernao Pires, E. Romero-Cadaval, D. Vinnikov, I. Roasto and J. F. Martins, "Power Converter Interfaces for Electrochemical Energy Storage Systems-A Review," *Energy Conversion and Management,* vol. 86, pp. 453-475, 2014.

[43] E. Muljadi, C. Butterfield, J. Chacon and H. Romanowitz, "Power Quality Aspects in a Wind Power Plant," in *Power Engineering Society General Meeting*, 2006.

[44] L. Qu and W. Qiao, "Constant Power Control of DFIG Wind Turbines with Supercapacitor Energy Storage," *IEEE Transactions on Industry Applications,* vol. 47, no. 1, pp. 359-367, 2011.

[45] P. Ray, N. Kishor and S. R. Mohanty, "Proportional-Integral Controller Based Small-signal Analysis of Hybrid Distributed Generation Systems," *Energy Conversion and Management,* vol. 52, pp. 1943-1954, 2011.

[46] O. G. Bellmunt, A. Junyent-Ferre, A. Sumper and J. Bergas-Jane, "Ride-Through Control of a Doubly Fed Induction Generator under Unbalanced Voltage Sags," *IEEE Transactions on Energy Conversion,* vol. 23, no. 4, pp. 1036-1045, 2009.

[47] C. Abbey and G. Joos, Integration of Distributed Energy Resources in Power Systems: Implementation, Operation, and Control, London: Elsevier, 2016.

[48] M. H. Ali, P. Minwon, Y. In-Keun, T. Murata and J. Tamura, "Improvement of Wind Generator Stability by Fuzzy Logic-controlled SMES," *IEEE Transactions on Industry Applications,* vol. 45, pp. 1045-1051, 2009.

[49] J. Shi, Y. J. Tang, L. Ren, J. D. Li and S. J. Chen, "Application of SMES in Wind Farm to Improve Voltage Stability," *Physica C: Superconductivity,* vol. 468, no. 15-20, pp. 2100-2103, 2008.

[50] G. O. Suvire and P. E. Mercado, "DSTATCOM with Flywheel Energy Storage System for Wind Energy Applications: Control Design and Simulation," *Electric Power Systems Research,* vol. 80, no. 3, pp. 345-353, 2010.

[51] J. A. Barrado, R. Grino and H. Valderrama-Blavi, "Power Quality Improvement of a Stand-alone Induction Generator Using STATCOM with Battery Energy Storage System," *IEEE Transactions on Power Delivery,* vol. 25, no. 4, pp. 2734-2741, 2010.

[52] H. Hayashi, Y. Hatabe, T. Nagafuchi, A. Taguchi, K. Terazono and T. Ishii, "Test Results of Power System Control by Experimental SMES," *IEEE Transactions on Applied Superconductivity,* vol. 16, pp. 598-601, 2006.

[53] EPRI, "Energy Storage for Grid-connected Wind Generation Applications," U. S. Department of Energy, Palo Alto, 2004.

[54] D. B. Liu, L. J. Shi, Q. Xu, W. J. Du and H. F. Wang, "Selection of Installing Locations of Flywheel Energy Storage System in Multimachine Power Systems by Modal Analysis," in *International Conference on Sustainable Power Generation and Supply*, Nanjing, 2009.

[55] F. Liu, S. Mei, D. Xia, Y. Ma, X. Jiang and Q. Lu, "Experimental Evaluation of Non-linear Robust Control for SMES to Improve the Transient Stability of Power Systems," *IEEE Transactions on Energy Conversion,* vol. 19, pp. 774-782, 2004.

[56] I. Ngamroo, A. N. Cuk-Supriyadi, S. Dechanupaprittha and Y. Mitani, "Power Oscillation Suppression by Robust SMES in Power Systems with Large Wind Power Penetration," *Physica C,* vol. 469, pp. 44-51, 2009.

[57] A. M. Vassallo, Advances in Batteries for Medium and Large-Scale Energy Storage, Darlington: Woodland Publishing, 2015.

[58] D. J. Lee and L. Wang, "Small-signal Stability Analysis of an Autonomous Hybrid Renewable Energy Power Generation/Energy Storage System Part I: Time-domain Simulations," *IEEE Transactions on Energy Conversion,* vol. 23, no. 1, pp. 311-320, 2008.

[59] K. Yoshimoto, T. Nanahara and G. Koshimizu, "Analysis of Data Obtained in Demonstration Test about Battery Energy Storage System to Mitigate Output Fluctuation of Wind Farm," in *CIGRE/IEEE PES Joint Symposium Integration of Wide-Scale Renewable Resources into the Power Delivery System*, Calgary, 2009.

[60] T. Sasaki, T. Kadoya and K. Enomoto, "Study on Load Frequency Control Using Redox Flow Batteries," *IEEE Transactions on Power Systems,* vol. 19, pp. 660-667, 2004.

[61] J. P. Barton and D. G. Infield, "Energy Storage and its Use with Intermittent Renewable Energy," *IEEE Transactions on Energy Conversion,* vol. 19, no. 2, pp. 441-448, 2004.

[62] N. Kawakami, Y. Iijima, M. Fukuhara, M. Bando, Y. Sakanaka, K. Ogawa and T. Matsuda, "Development and Field Experiences of Stabilization System Using 34MW NaS Batteries for a 54MW Wind Farm," in *International Symposium on Industrial Electronics*, Bari, 2010.

[63] Y. Hida, R. Yokoyama, J. Shimizukawa, K. Iba and T. Seki, "Load Following Operation of NAS Battery by Setting Statistic Margins to Avoid Risks," in *IEEE PES General Meeting*, Minneapolis, 2010.

[64] T. K. Brekken, A. Yokochi, A. von Jouanne, Z. Z. Yen, H. M. Hapke and D. A. Halamay, "Optimal Energy Storage Sizing and Control for Wind Power Applications," *IEEE Transactions on Sustainable Energy,* vol. 2, pp. 69-77, 2011.

[65] I. Dimitrios, S. Voutetakis, P. Seferlis, F. Stergiopoulos and C. Elmasides, "Power Management Strategies For a Stand-alone Power System Using Renewable Energy Sources and Hydrogen Storage," *International Journal of Hydrogen Energy,* vol. 34, no. 16, pp. 7081-7095, 2009.

[66] M. Little, M. Thomson and D. Infield, "Electrical integration of renewable energy into stand-alone power supplies incorporating hydrogen storage," *International Journal of Hydrogen Energy,* vol. 32, no. 10, pp. 1582-1588, 2007.

[67] World Energy Council, "Latest Trends in Energy Storage, 2019," 2019.

[68] A. Aktas, K. Erhan, S. Ozdemir and E. Ozde, "Experimental Investigation of a New Smart Energy Management Algorithm for a Hybrid Energy Storage System in Smart Grid Applications," *Electric Power Systems Research,* vol. 144, pp. 185-196, 2017.

[69] A. Karabiber, "Power Management of a Hybrid Energy Storage System in a Domestic Microgrid," in *10th International Conference on Electrical and Electronics Engineering (ELECO)*, Bursa, 2017.

[70] Q. Xu, X. Hu, P. Wang, J. Xiao, P. Tu, C. Wen and M. Y. Lee, "A Decentralized Dynamic Power Sharing Strategy for Hybrid Energy Storage System in Autonomous DC Microgrid," *IEEE Transactions on Industrial Electronics,* vol. 64, no. 7, pp. 5930-5941, 2017.

[71] J. Li, Q. Yang, F. Robinson, F. Liang, M. Zhang and W. Yuan, "Design and Test of a New Droop Control Algorithm for a SMES/Battery Hybrid Energy Storage System," *Energy,* vol. 118, pp. 1110-1122, 2017.

[72] J. Li, X. Wang, Z. Zhang, S. Le Blond, Q. Yang, M. Zhang and W. Yuan, "Analysis of a New Design of the Hybrid Energy Storage System Used in the Residential m-CHP Systems," *Jianwei Li, Xudong Wang, Zhenyu Zhang, Simon Le Blond, Qingqing Yang, Min Zhang, Weijia Yuan,* vol. 187, pp. 169-179, 2017.

[73] T.-T. Nguyen, H.-J. Yoo and H.-M. Kim, "A Flywheel Energy Storage System Based on a Doubly Fed Induction Machine and Battery for Microgrid Control," *Energies,* vol. 8, no. 6, pp. 5074-5089, 2015.

[74] W. Jing, C. H. Lai, S. H. W. Wong and M. L. D. Wong, "Battery-Supercapacitor Hybrid Energy Storage System in Standalone DC Microgrids: A Review," *IET Renewable Power Generation,* vol. 11, no. 4, pp. 461-469, 2017.

[75] J. J. Justo, F. Mwasilu, J. Lee and J.-W. Jung, "AC-Microgrids versus DC-Microgrids with Distributed Energy Resources: A Review," *Renewable and Sustainable Energy Reviews,* vol. 24, pp. 387-405, 2013.

[76] J. P. Zheng, T. R. Jow and M. S. Ding, "Hybrid Power Sources for Pulsed Current Applications," *IEEE Transactions on Aerospace and Electronic Systems,* vol. 37, no. 1, pp. 288-292, 2001.

[77] R. A. Dougal, S. Liu and R. E. White, "Power and Life Extension of Battery-Ultracapacitor Hybrids," *IEEE Transactions on Components and Packaging Technologies,* vol. 25, no. 1, pp. 120-131, 2002.

[78] S. K. Singal, Varun and R. P. Singh, "Rural Electrification of a Remote Island by Renewable Energy Sources," *Renewable Energy,* vol. 32, no. 15, pp. 2491-2501, 2007.

[79] S. Pay and Y. Baghzouz, "Effectiveness of Battery-Supercapacitor Combination in Electric Vehicles," in *IEEE Bologna Power Tech Conference Proceedings*, Bologna, 2003.

[80] R. A. Dougal, S. Liu and R. E. White, "Power and Life Extension of Battery-Ultracapacitor Hybrids," *IEEE Transactions on Components and Packaging Technologies,* vol. 25, no. 1, pp. 120-131, 2002.

[81] Z. Song, H. Hofmann, J. Li, X. Han, X. Zhang and M. Ouyang, "A Comparison Study of Different Semi-Active Hybrid Energy Storage System Topologies for Electric Vehicles," *Journal of Power Sources,* vol. 274, pp. 400-411, 2015.

[82] W. Li and G. Joos, " A Power Electronic Interface for a Battery Supercapacitor Hybrid Energy Storage System for Wind Applications," in *2008 IEEE Power Electronics Specialists Conference*, Rhodes, 2008.

[83] A. Etxeberria, I. Vechiu, H. Camblong and J. M. Vinassa, "Comparison of Three Topologies and Controls of a Hybrid Energy Storage System for Microgrids," *Energy Conversion and Management,* vol. 54, no. 1, pp. 113-121, 2012.

[84] I. J. Cohen, C. S. Westenhover, D. A. Wetz, J. M. Heinzel and Q. Dong, "Evaluation of an Actively Controlled Battery-Capacitor Hybrid Energy Storage Module (HESM) for Use in Driving Pulsed Power Applications," in *IEEE Pulsed Power Conference (PPC)*, Austin, 2015.

[85] A. Kuperman, I. Aharon, S. Malki and A. Kara, "Design of a Semiactive Battery-Ultracapacitor Hybrid Energy Source," *IEEE Transactions on Power Electronics,* vol. 28, no. 2, pp. 806-815, 2013.

[86] S. K. Kollimalla, M. K. Mishra and N. L. Narasamma, "Design and Analysis of Novel Control Strategy for Battery and Supercapacitor Storage System," *IEEE Transactions on Sustainable Energy,* vol. 5, no. 4, pp. 1137-1144, 2014.

[87] E. Jamshidpour, S. Saadate and P. Poure, "Energy Management and Control of a Stand-alone Photovoltaic/Ultra Capacitor/Battery Microgrid," in *IEEE Jordan Conference on Applied Electrical Engineering and Computing Technologies (AEECT)*, Amman, 2015.

[88] J. Cao and A. Emadi, "A New Battery/UltraCapacitor Hybrid Energy Storage System for Electric, Hybrid, and Plug-In Hybrid Electric Vehicles," *IEEE Transactions on Power Electronics,* vol. 27, no. 1, pp. 122-132, 2012.

[89] S. M. Lukic, S. G. Wirasingha, F. Rodriguez, J. Cao and A. Emadi, "Power Management of an Ultracapacitor/Battery Hybrid Energy Storage System in an HEV," in *IEEE Vehicle Power and Propulsion Conference*, Windsor, 2006.

[90] J. Rocabert, A. Luna, F. Blaabjerg and P. Rodeiguez, "Control of Power Converters in AC Microgrids," *IEEE Transactions on Power Electronics,* vol. 27, no. 11, pp. 4734-4749, 2012.

[91] A. Tani, M. B. Camara and B. Dakyo, "Energy Management in the Decentralized Generation Systems Based on Renewable Energy—Ultracapacitors and Battery to Compensate the Wind/Load Power Fluctuations," *IEEE Transactions on Industry Applications,* vol. 51, no. 2, pp. 1817-1827, 2015.

[92] H. Yu, R. Lu, T. Wang and C. Zhu, "Battery/ultra-capacitor Hybrid Energy Storage System Used in HEV," *Journal of Asian Electric Vehicles,* vol. 8, no. 1, pp. 1351-1356, 2010.

[93] J. Jang and J. Yoo, "Equivalent Circuit Evaluation Method of Lithium Polymer Battery Using Bode Plot and Numerical Analysis," *IEEE Transactions on Energy Conversion,* vol. 26, no. 1, pp. 290-298, 2011.

[94] Y. Zhang, Z. Jiang and X. Yu, "Control Strategies for Battery/Supercapacitor Hybrid Energy Storage Systems," in *IEEE Energy 2030 Conference*, Atlanta, 2008.

[95] X. Hu, Q. Xu, P. Wang, J. Xiao, P. Tu, C. Wen and M. Y. Lee, "A Decentralised Dynamic Power Sharing Strategy for Hybrid Energy Storage System in Autonomous DC Microgrid," *IEEE Transactions on Industrial Electronics,* vol. 67, no. 7, pp. 5930-5941, 2017.

[96] Y. Gu, W. Li and X. He, "Frequency-Coordinating Virtual Impedance for Autonomous Power Management of DC Microgrid," *IEEE Transactions on Power Electronics,* vol. 30, no. 4, p. 2014, 2328-2337.

[97] Texas Instruments, "Basic Calculation of Boost Converter's Power Stage," Dallas, 2014.

[98] MathWorks, "Average-Value DC-DC Converter," [Online]. Available: https://se.mathworks.com/help/physmod/sps/ref/averagevaluedcdcconverter.html. [Accessed 18 February 2020].

[99] S. Hajiaghasi, A. Salemnia and M. Hamzeh, "Hybrid Energy Storage for Microgrid Performance Improvement under Unbalanced Load Conditions," *Journal of Energy Management and Technology (JEMT),* vol. 2, no. 1, pp. 32-41, 2018.

[100] S. Sanchez, *Stability Investigation of Power Electronics Systems,* Trondheim: PhD Thesis, 2015.

[101] adafruit, "DIY DC/DC Boost Calculator," 3 June 2020. [Online]. Available: https://learn.adafruit.com/diy-boost-calc/the-calculator. [Accessed 3 June 2020].

[102] M. M. Aly, M. Abdel-Akher, S. M. Said and T. Senjyu, "A developed control strategy for Mitigating Wind Power Generation Transients Using Superconducting Magnetic Energy Storage with Reactive Power Support," *International Journal of Electrical Power and Energy Systems,* vol. 83, pp. 485-494, 2016.

[103] A. Yazdani and R. Iravani, Voltage-Sourced Converters in Power Systems: Modeling, Control and Applications, Hoboken: Wiley, 2010.

[104] P. Kundur, Power System Stability and Control, McGraw-Hill Education, 1994.

[105] A. Reznik, M. G. Simoes, A. Al-Durra and S. M. Muyeen, "LCL Filter Design and Performance Analysis for Grid-Interconnected Systems," *IEEE Transactions on Industry Applications,* vol. 50, no. 2, pp. 1225-1232, 2014.

[106] T. Suntio, T. Messo and J. Puukko, Power Electronic Converters, Weinheim: Wiley-VCH, 2018.

[107] A. Esmaili, B. Novakovic, O. J. Abdel-baqi and A. Nasiri, "A Hybrid System of Li-Ion Capacitors and Flow Battery for Dynamic Wind Energy Support," *IEEE Transactions on Industry Applications,* vol. 49, no. 4, pp. 1649-1657, 2013.

[108] Q. Xie, Y. Wang, Y. Kim, M. Pedram and N. Chang, "Charge Allocation in Hybrid Electrical Energy Storage Systems," *IEEE Transactions on Computer-Aided Design of Integrated Circuits and Systems,* vol. 32, no. 7, pp. 1003-1016, 2013.

[109] N. R. Tummuru, M. K. Mishra and S. Srinivas, "Dynamic Energy Management of Renewable Grid Integrated Hybrid Energy Storage System," *IEEE Transactions on Industrial Electronics,* vol. 62, no. 12, pp. 7728-7737, 2015.

[110] H. Yoo, S. K. Sul, Y. Park and J. Jeong, "System Integration and Power-Flow Management for a Series Hybrid Electric Vehicle using Supercapacitors and Batteries," *IEEE Transactions on Industrial Applications,* vol. 44, no. 1, pp. 108-114, 2008.

[111] A. Mohamed, V. Salehi and O. Mohammed, "Real-Time Energy Management Algorithm for Mitigation of Pulse Loads in Hybrid Microgrids," *IEEE Transactions on Microgrids,* vol. 3, no. 4, pp. 1911-1922, 2012.

[112] M. U. Shahid, M. M. Khan, J. Xu, K. Hashmi and S. Habib, "A Hierarchical Control Methodology for Renewable DC Microgrids Supporting a Variable Communication Network Health," *Electronics,* vol. 7, no. 12, 2018.

[113] S. Dusmez and A. Khaligh, "A Supervisory Power-Splitting Approach for a New Ultracapacitor-Battery Vehicle Deploying Two Propulsion Machines," *IEEE Transactions on Industrial Information,* vol. 10, no. 3, pp. 1960-1971, 2014.

[114] B. Hredzak, V. G. Agelidis and M. Jang, "A Model Predictive Control System for a Hybrid Battery-Ultracapacitor Power Source," *IEEE Transactions on Power Electronics,* vol. 29, no. 3, pp. 1469-1479, 2014.

[115] Y. Gu, X. Xiang, W. Li and X. He, "Mode-Adaptive Decentralised Control for Renewable DC Microgrid with Enhanced Reliability and Flexibility," *IEEE Transactions on Power Electronics,* vol. 29, no. 9, pp. 5072-5080, 2014.

[116] D. E. Olivares, A. Mehrizi-Sani, A. H. Etemadi and C. A. Canizares, "Trends in Mircorgid Control," *IEEE Transactions on Smart Grid,* vol. 5, no. 4, pp. 1905-1919, 2014.

[117] J. M. Guerrero, M. Chandorkar, T.-L. Lee and P. C. Loh, "Advanced Control Architectures for Intelligent Microgrids: Part 1-Decentralised and Hierarchical Control," *IEEE Transactions on Industrial Electronics,* vol. 60, no. 4, pp. 1254-1262, 2013.

[118] J. Zhang, J.-S. Lai and W. Yu, "Bi-directional DC-DC Converter Modeling and Unified Controller with Digital Implementation," in *Twenty-Third Annual IEEE Applied Power Electronics Conference and Exposition*, Austin, 2008.

[119] M. E. Glavin, P. K. Chan, S. Armstrong and W. G. Hurley, "M. E. Glavin, P. K. W. Chan, S. Armstrong and W. G. Hurley, "A Stand-alone Photovoltaic Supercapacitor Battery Hybrid Energy Storage System," in *13th International Power Electronics and Motion Control Conference*, Poznan, 2008.

[120] S. Ruihua, Z. Chao, L. Ruomei and Z. Xiaoxin, "VSCs Based HVDC and Its Control Strategy," in *IEEE/PES Transmission & Distribution Conference & Exposition: Asia and Pacific*, Dalian, 2005.

[121] R. W. De Doncker and D. W. Novotny, "The Universal Field Oriented Controller," *IEEE Transactions on Industry Applications,* vol. 30, no. 1, pp. 92-100, 1994.

[122] M. P. Kazmierkowski, Control in Power Electronics, Warsaw: Academic Press, 2002.

[123] F. Katiraei, M. R. Iravani and P. W. Lehn, "Microgrid Autonomous Operation During and Subsequent to Islanding Process," *IEEE Transactions on Power Delivery,* vol. 20, no. 1, pp. 248-257, 2005.

[124] K. Uhlen and A. G. Endegnanew, "Global Analysis of Frequency Stability and Inertia in AC systems Interconnected through an HVDC," in *2016 IEEE International Energy Conference (ENERGYCON)*, Leuven, 2016.

[125] C. Bajracharya, M. Molinas and J. A. Suul, "Understanding of Tuning Techniques of Converter Controllers for VSC-HVDC," in *Nordic Workshop on Power and Industrial Electronics*, Espoo, 2008.

[126] M. Liserre, *Innovative Control Techniques for Power Converters for Industrial Automation,* Bari, 2002.

[127] J. G. Dedecca and R. A. Hakvoort, "A Review of the North Seas Offshore Grid Modelling: Current and Future Research," *Renewable and Sustainable Energy Reviews,* vol. 60, pp. 129-143, 2016.

[128] X. Luo, J. Wang, M. Dooner and J. Clarke, "Overview of current development in electrical storage technologies and the application potential in power system operation," *Applied Energy,* vol. 137, pp. 511-536, 2015.

[129] H. Karimi, H. Nikkhajoei and R. Iravani, "Control of an Electronically-Coupled Distributed Resource Unit Subsequent to an Islanding," *IEEE Transactions on Power Delivery,* vol. 23, no. 1, pp. 493-501, 2008.

[130] M. Popov, H. Karimi, H. Nikkhajoei and V. Terzija, "Modelling, Control, and Islanding Detection of Microgrids with Passive Loads," in *Proceedings of 14th International Power Electronics and Motion Control Conference EPE-PEMC 2010*, Ohrid, 2010.

[131] E. K. W. Cheng, Classical Switched Mode and Power Converters, Hong Kong: The Hong Kong Polytechnical University, 2002.

[132] V. Ramanarayanan, *Course Material on Switched Mode Power Conversion,* Bangalore: Indian Institute of Science, 2007.

Appendices

A MATLAB scripts

A.1 DC system parameters and bidirectional DC/DC converter control designs

```matlab
%%%% BIDIRECTIONAL DC/DC CONVERTER

clearvars; clc;
s = tf('s');


%% Converter parameters

Vdc = 400; % DC bus nominal voltage
Vr = 0.02*400; % 2 percent voltage ripple
Pdc = 5e3; % Nominal AC power
Rdc = Vdc^2/Pdc; % Rated load
Idc = Pdc/Vdc; % Rated load current
Idcmax = 1.10*Idc; % Maximum load current 10%
ev = 0.04; % Maximum voltage deviation +-4%

Sb = 5e3; % Base apparent power
Vb_vsc = 260*sqrt(2/3); % peak base voltage, VSC: star-connected Vph-ph = Vline = sqrt(3)*Vph-g
Ib_vsc = (2/3)*(Sb/Vb_vsc); % peak base current, VSC

Vb_dc = 2*Vb_vsc; % Base DC voltage
Ib_dc = (3/4)*Ib_vsc; % Base DC current

ILr = 0.10; % 10 percent inductor current ripple

fsw = 10e3; % Base switching frequency
wsw = 2*pi*fsw; % Base switching angular frequency


%% Battery parameters

Vb = 200; % Battery voltage
Db = 1 - (Vb/Vdc); % Battery duty cycle
rb = 0.001; % Input filter resistance
Lb_min = (Db*Vb*(1 - Db))/(2*fsw*Idc); % Minimum source inductance
Lb = Lb_min; % Selected source inductance

Ib = Idc/(1 - Db); % Input current from battery
Ibr = (Vb*Db)/(fsw*Lb); % Inductor peak-to-peak current ripple
Ibrms = sqrt((Pdc/Vb)^2 + Ibr^2/12); % Maximum RMS inductor current
Ibsw = sqrt((Db*(Pdc/Vb)^2) + Ibr^2/12); % Inductor switching peak ripple current

ESRb = Vr/Ibsw; % ESR based on battery inductor switching current


%% Supercapacitor parameters
```

```matlab
Vsc = 250; % Supercapacitor voltage
Dsc = 1 - (Vsc/Vdc); % Supercapacitor duty cycle
rsc = 0.001; % Input filter resistance
Lsc_min = (Dsc*Vsc*(1 - Dsc))/(2*fsw*Idc); % Minimum source inductance
Lsc = Lsc_min; % Selected source inductance

Isc = Idc/(1 - Dsc); % Input current from battery
Iscr = (Vsc*Dsc)/(fsw*Lsc); % Inductor peak-to-peak current ripple
Iscrms = sqrt((Pdc/Vsc)^2 + Iscr^2/12); % RMS inductor current
Iscsw = sqrt((Dsc*(Pdc/Vsc)^2) + Iscr^2/12); % Inductor switching peak ripple
current

ESRsc = Vr/Iscsw; % ESR based on supercapacitor inductor current

fRHPZ = ((1 - Dsc)^2*Rdc)/(2*pi*Lsc); % Right-hand plane zero frequency
wRHPZ = 2*pi*fRHPZ;

%% Output capacitor

Cdc_min = Idc/(fsw*Vr); % Minimum output capacitance
Cdc = 8*Cdc_min; % Adjustment to obtain good reponse
ESR = ESRsc; % Choose higher ESR between battery and supercapacitor


%% Controller design

rho = 0.7; % Damping ratio to yield good step response and damped oscillation
nib = 10; % Order reduction for battery bandwidth
nisc = 6; % Order reduction for supercapacitor bandwith
nv = 20; % Order reduction for HESS voltage controller
wob = wsw/nib; % Battery bandwidth
wosc = wsw/nisc; % Supercapacitor bandwidth
wov = wsw/nv; % Voltage controller bandwidth

fob = wob/(2*pi); fosc = wosc/(2*pi); fov = wov/(2*pi);

% Hv controller parameters
kpv = 2*rho*wob*Cdc; % Voltage control loop proportional gain
kiv = wov^2*Cdc; % Voltage control loop integral gain

% Hi controller parameters
% Battery
kpb = 2*rho*wob*Lb; % Battery current control loop proportional gain
kib = wob^2*Lb; % Battery current control loop integral gain

% Hi controller parameters
% Supercapacitor
kpsc = 2*rho*wosc*Lsc; % Supercapacitor current control loop proportional gain
kisc = wosc^2*Lsc; % % Supercapacitor current control loop integral gain
```

A.2 AC system parameters and 2L-VSC control design

```matlab
%%%% 2-LEVEL VOLTAGE SOURCE CONVERTER

clearvars;
clc;
```

```matlab
s = tf('s');

%% Parameters

Sb = 5e3; % Base apparent power
Pn = 5e3; % Nominal active power
pf = 1; % Power factor with phase angle zero
Pload = 3e3; % Load power
Vload = 520; % Phase-phase voltage at load connection point
Rload = Vload^2/Pload; % Load resistance
Iload = Pload/Vload; % Load current
Vdc = 400; % Nominal DC bus voltage

Vb_vsc = 260*sqrt(2/3); % Peak base voltage at converter side: Star-connected
where Vph-ph = Vline = sqrt(3)*Vph-g
Ib_vsc = (2/3)*(Sb/Vb_vsc); % peak base current at converter side

Vb_grid = 520*sqrt(2/3); % Peak base voltage grid side: Star-connected where Vph-
ph = Vline = sqrt(3)*Vph-g
Ib_grid = (2/3)*(Sb/Vb_grid); % Peak base current at grid side

Zb = Vb_vsc/Ib_vsc;% Base impedance at converter side (for filter pu computation)

fb = 60; % Nominal frequency
wb = 2*pi*fb; % Nominal angular frequency

Lb = Zb/wb; % Base inductance
Cb = 1/(Zb*wb); % Base capacitance

%% DC base values

Pb_dc = Pn; % Base power
Vb_dc = 2*Vb_vsc; % Base voltage
Ib_dc = (3/4)*Ib_vsc; % Base current
Zb_dc = Vb_dc/Ib_dc; % Base impedance
Rb_dc = (8/3)*Zb; % Base resistance
Cb_dc = (3/8)*Cb; % Base capacitance
Lb_dc = (8/3)*Lb; % Base inductance

L = 2e-4; % Battery converter inductor
r = 0.001; % Source resistor
ESR  = 0.4753; % DC bus capacitor equivalent series resistance
Cdc = 1.5625e-4*2; % DC bus capacitor
Cdcpu = Cdc/Cb_dc; % DC bus capacitor in pu

fsw = 5e3; % AC switching frequency
wsw = 2*pi*fsw; % AC switching angular frequency

%% LCL filter design

L2pu = 0.06; % Transformer leakage reactance in pu
R2pu = 0.002; % Transformer leakage resistance in pu

L2 = L2pu*Lb; % SI unit values of transformer leakage reactance and resistance
R2 = R2pu*Zb;

Cfact = 0.05*Cb; % Filter capacitor = 5% of maximum power factor variation of grid
Cf = 9e-6; % Adjustment to improve output
```

```matlab
m = 0.5; % Modulation factor of typical SPWM where maximum peak-to-peak current
ripple occurs
ILmax = (Pn*sqrt(2))/(3*(260/sqrt(3))); % Maximum inverter output current
Imax_ripple = 0.1*ILmax; % 10 percent ripple in maximum output inverter current

L1 = Vdc/(6*fsw*Imax_ripple); % VSC side inductor of LCL filter
R1 = 0.1; % VSC side resistor of LCL filter

wres = sqrt((L1 + L2)/(L1*L2*Cf)); % Resonance frequency
fres = wres/(2*pi);

Rf = 1/(3*wres*Cf); % Filter capacitor damping resistor

Pf = (260/sqrt(3))^2/Rf; % Power comsumption by filter capacitor and damping
resistor
XCf = 1/(2*pi*fb*Cf);
Qf = (260/sqrt(3))^2/XCf;


%% Calculation of per-unit values

L1pu = L1/Lb;
R1pu = R1/Zb;

Ltpu = L1pu + L2pu;
Rtpu = R1pu + R2pu;


%% Inner current controller (Modulus optimum criteria)

Ta = 1.5/fsw; % Delay associated with modulation where corner frequency is 1 to 2
orders less than switching frequency
Ti = Ltpu/(wb*Rtpu); % Time constant, tau in pu

% PI controller parameters
kpi = Ltpu/(2*wb*Ta); % Proportional gain
kii = kpi/Ti; % Integral gain

% Compensated transfer functions of inner control loop
gol_i = (1/(2*Ta*s))*(1/(1 + Ta*s)); % Open-loop
gcl_i = 1/(2*Ta^2*s^2 + 2*Ta*s + 1); % Closed-loop

wo = 1/(sqrt(2)*Ta); % Control frequency
ro = Ta*wo; % Optimal approximation of 0.707


%% Outer grid controller (Symmetrical optimum)

a = 3; % Default value of a

Teq = 2*Ta; % Equivalent time constant of the inner loop as seen by outer voltage
loop
p = 1/Teq; % Pole location of the inner loop
alpha = 6; % A gain to obtain a smaller zero frequency than pole frequency, i.e.
wz < wp
phi = asin((alpha - 1)/(alpha + 1)); % Phase margin defined by alpha
z = p/alpha; % Control design zero
```

```matlab
wcutoff = sqrt(z*p); % Frequency at which maximum phase margin is reached

if a == -1
    b = 1/(Cdcpu*wb);
    kvv = b*wcutoff;
else
    kvv = (Cdcpu/wb)*wcutoff;
end

% PI controller parameters
kpv = kvv; % Proportional gain
kiv = kvv*z; % Integral gain

% Compensated transfer functions
gol_v = (1/(a^3*Teq^2*s^2))*((1 + a^2*Teq*s)/(1 + Teq*s));
gcl_v = (1 + a^2*Teq*s)/(1 + a^2*Teq*s + a^3*Teq^2*s^2 + a^3*Teq^3*s^3);
```

A.3 Full hybrid DC/AC system

```matlab
clearvars; clc;

s = tf('s');


%% Parameters

Sb = 5e3; % Base apparent power
Pn = 2.5e3; % Nominal active power
pf = 1;
Pb = Sb*pf;
Vdc = 400;
Vr = 0.02*Vdc;

Pload = 3e3;
Vload = 520;
Rload = Vload^2/Pload;
Iload_ac = Pload/Vload;
Iload_dc = Pn/Vdc;


fsw_ac = 5e3; % VSC PWM switching frequency
wsw_ac = 2*pi*fsw_ac;

fsw_dc = 10e3; % DC converters PWM switching frequency
wsw_dc = 2*pi*fsw_dc;

Vb_vsc = 260*sqrt(2/3); % peak base voltage converter side: star-connected Vph-ph
= Vline = sqrt(3)*Vph-g
Ib_vsc = (2/3)*(Sb/Vb_vsc); % peak base current grid side

Vb_grid = 520*sqrt(2/3); % peak base voltage grid side: star-connected Vph-ph =
Vline = sqrt(3)*Vph-g
Ib_grid = (2/3)*(Sb/Vb_grid); % peak base current grid side

Zb = Vb_vsc/Ib_vsc;% base impedance converter side (for filter)
fb = 60; % nominal frequency
```

```matlab
wb = 2*pi*fb; % angular frequency

Lb = Zb/wb;
Cb = 1/(Zb*wb);

%% DC base values

Pb_dc = Pn;
Vb_dc = 2*Vb_vsc;
Ib_dc = (3/4)*Ib_vsc;
Zb_dc = Vb_dc/Ib_dc;
Rb_dc = (8/3)*Zb;
Cb_dc = (3/8)*Cb;
Lb_dc = (8/3)*Lb;

ESR  = 0.4753;
Cdc_min = Iload_dc/(fsw_dc*Vr); % Minimum output capacitance
Cdc = Cdc_min*2; % Mutiplied by a factor of 2 for full system
Cdcpu = Cdc/Cb_dc;


%% 2L-VSC
%% LCL filter design

L2pu = 0.06; % Transformer leakage reactance and resistance in pu
R2pu = 0.002;

L2 = L2pu*Lb; % SI unit values
R2 = R2pu*Zb;

Cfact = 0.05*Cb; % Filter capacitor - 5% maximum power factor variation
Cf = 9e-6;

m = 0.5; % modulation factor of typical SPWM where maximum peak-to-peak current
ripple occurs
ILmax = (Pn*sqrt(2))/(3*(260/sqrt(3)));
Imax_ripple = 0.1*ILmax;

L1 = 2*Vdc/(6*fsw_ac*Imax_ripple); % VSC side inductor
R1 = 0.2;

wres = sqrt((L1 + L2)/(L1*L2*Cf)); % Resonance frequency
fres = wres/(2*pi);

Rf = 1/(3*wres*Cf); % Filter capacitor damping resistor

Pf = (260/sqrt(3))^2/Rf; % Active power drawn by Rf
XCf = 1/(2*pi*fb*Cf);
Qf = (260/sqrt(3))^2/XCf; % Capacitive reactive power drawn by Cf


%% Calculation of per-unit values

L1pu = L1/Lb;
R1pu = R1/Zb;

Ltpu = L1pu + L2pu;
Rtpu = R1pu + R2pu;
%% Inner current controller (Modulus optimum) %%%%%%%%%%%%%%%%%%%%
```

```matlab
% Delay associated with modulation
Ta = 1.5/fsw_ac; % corner frequency 1 or 2 orders less than switching frequency

% Controller parameters design

Ti = Ltpu/(wb*Rtpu); % Time constant, tau in pu
kpi = Ltpu/(2*wb*Ta); % proportional gain
kii = kpi/Ti; % integral gain

% Compensated transfer functions of inner control loop
gol_i = (1/(2*Ta*s))*(1/(1 + Ta*s));
gcl_i = 1/(2*Ta^2*s^2 + 2*Ta*s + 1);

wo = 1/(sqrt(2)*Ta); % control frequency
ro = Ta*wo; % optimal approx. of 0.707


%% Outer grid controller (Symmetrical optimum) %%%%%%%%%%%%%%%%%%%%%%

a = 3; % default value of a

Teq = 2*Ta; % equivalent time constant of the inner loop
p = 1/Teq; % pole location of the inner loop
alpha = 6; % a gain to obtain a smaller zero frequency than pole frequency, i.e.
wz < wp
phi = asin((alpha - 1)/(alpha + 1)); % phase margin defined by alpha
z = p/alpha; % control design zero

wcutoff = sqrt(z*p); % frequency at which maximum phase margin is reached

if a == -1
    b = 1/(Cdcpu*wb);
    kvv = b*wcutoff;
else
    kvv = (Cdcpu/wb)*wcutoff;
end

kpv_ac = kvv; % proportional gain of outer control loop controller
kiv_ac = kvv*z; % integral gain of outer control loop controller

% Compensated transfer functions
gol_v = (1/(a^3*Teq^2*s^2))*((1 + a^2*Teq*s)/(1 + Teq*s));
gcl_v = (1 + a^2*Teq*s)/(1 + a^2*Teq*s + a^3*Teq^2*s^2 + a^3*Teq^3*s^3);




%% BIDIRECTIONAL DC/DC CONVERTER
%% Parameters

Pdc = 5e3;
Iloadmax = 1.10*Iload_dc;
ev = 0.04;


Vb_dc = 2*Vb_vsc;
Ib_dc = (3/4)*Ib_vsc;


ILr = 0.10; % 10 percent inductor current ripple
Ts_power = 2e-5; Ts_control = 20e-4;
```

```matlab
%% Battery parameters

Vb = 200;
Db = 1 - (Vb/Vdc);
rb = 0.001;
Lb_min = (Db*Vb*(1 - Db))/(2*fsw_dc*Iload_dc);
Lb = Lb_min;

ILb = Iload_dc/(1 - Db);
ILbr = (Vb*Db)/(fsw_dc*Lb);
ILbrms = sqrt((Pdc/Vb)^2 + ILbr^2/12);
ILbsw = sqrt((Db*(Pdc/Vb)^2) + ILbr^2/12);

ESRb = Vr/ILbsw;

%% Supercapacitor parameters

Vsc = 250;
Dsc = 1 - (Vsc/Vdc);
rsc = 0.001;
Lsc_min = (Dsc*Vsc*(1 - Dsc))/(2*fsw_dc*Iload_dc);
Lsc = Lsc_min;

Isc = Iload_dc/(1 - Dsc);
ILscr = (Vsc*Dsc)/(fsw_dc*Lsc);
ILscrms = sqrt((Pdc/Vsc)^2 + ILscr^2/12);
ILscsw = sqrt((Dsc*(Pdc/Vsc)^2) + ILscr^2/12);

ESRsc = Vr/ILscsw;


%% Controller design

rho = 0.7; % damping ratio
nib = 10;
nisc = 6;
nv = 20;
wob = wsw_dc/nib; % battery bandwidth lower than switching frequency by order
1/nib
wosc = wsw_dc/nisc; % supercapacitor bandwidth lower than switching frequency by
order 1/nisc
wov = wsw_dc/nv; % voltage controller with lowest bandwidth

%% Hv controller parameters
kpv_dc = 2*rho*wob*Cdc;
kiv_dc = wov^2*Cdc;

%% Hi controller parameters
% Battery
kpb = 2*rho*wob*Lb;
kib = wob^2*Lb;

% Hi controller parameters
% Supercapacitor
kpsc = 2*rho*wosc*Lsc;
kisc = wosc^2*Lsc;
```

B Simulink simulation models
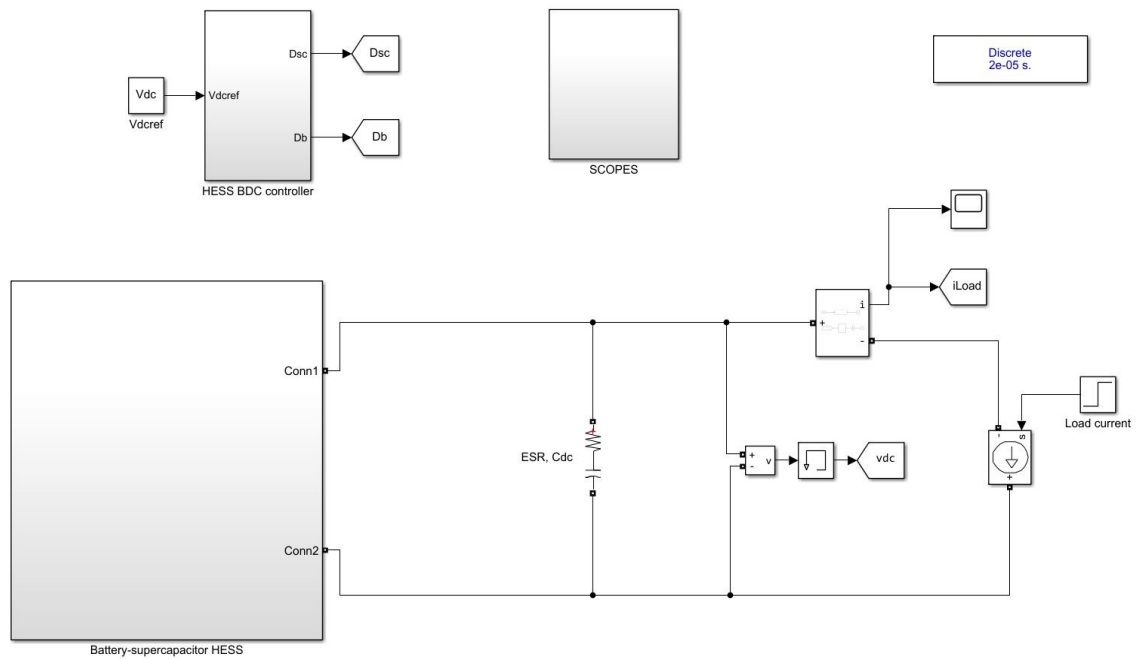
Figure B.1: Standalone DC system with HESS
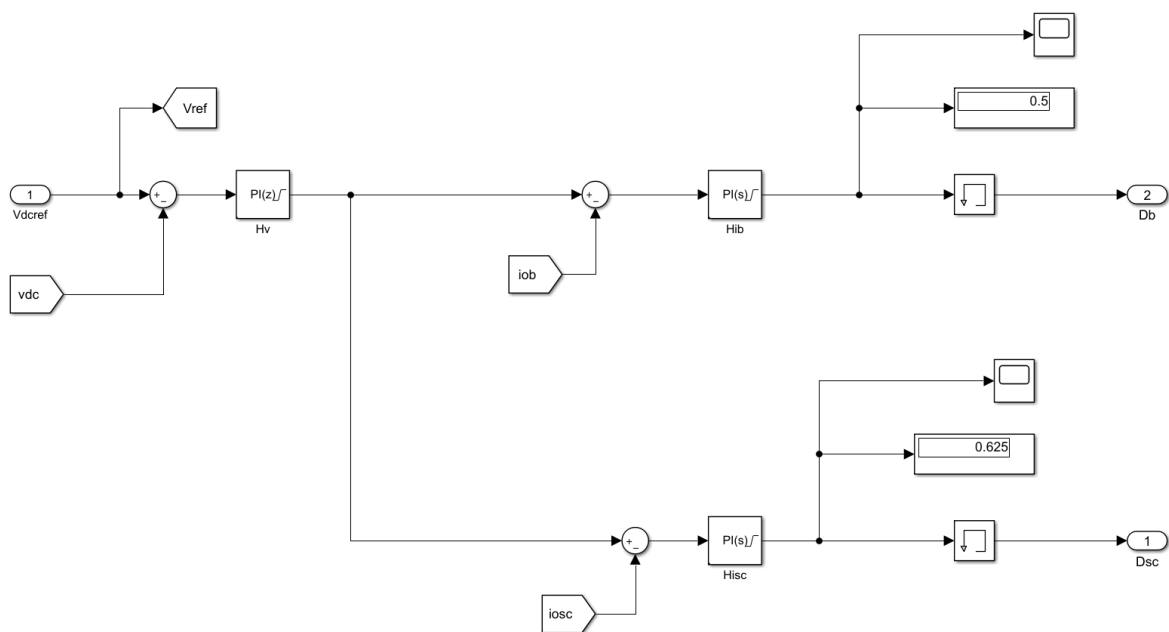
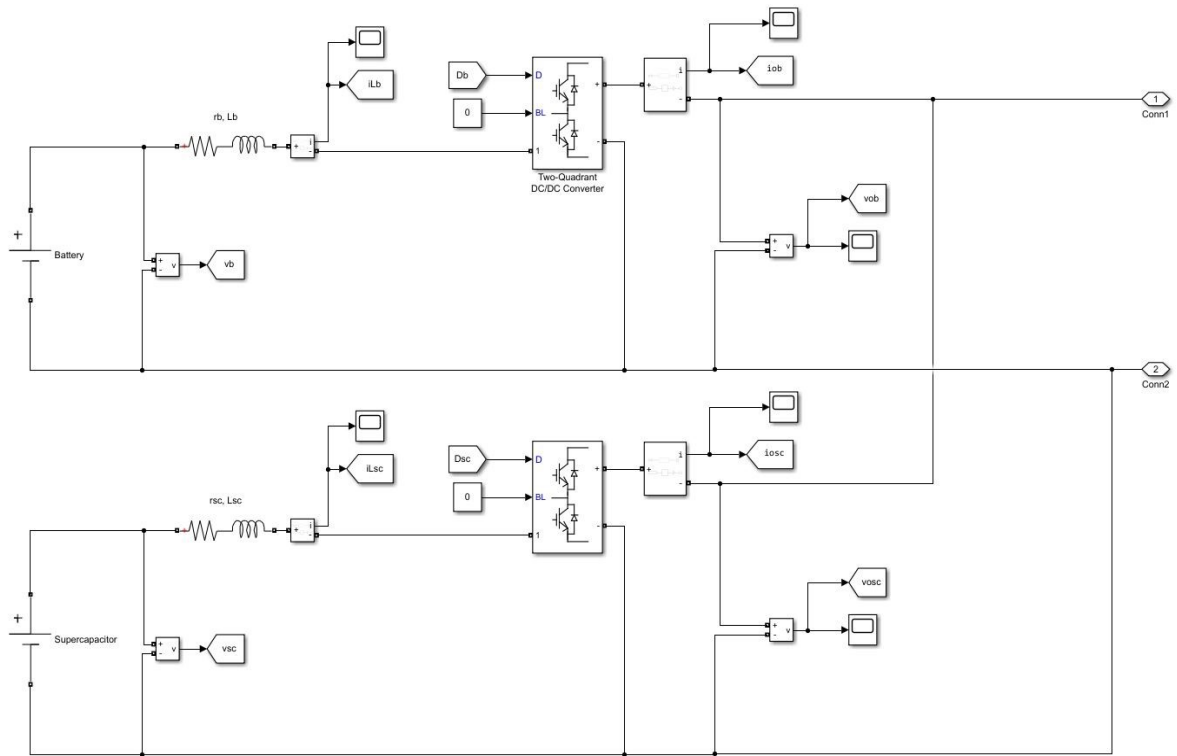**Figure B.2: Structure of HESS controller**

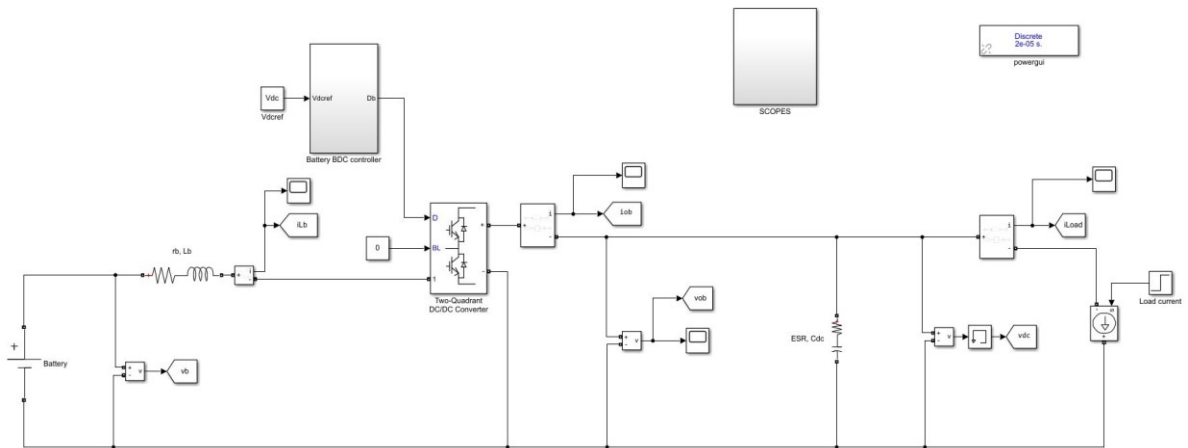**Figure B.3: Parallel active topology of HESS storage elements**
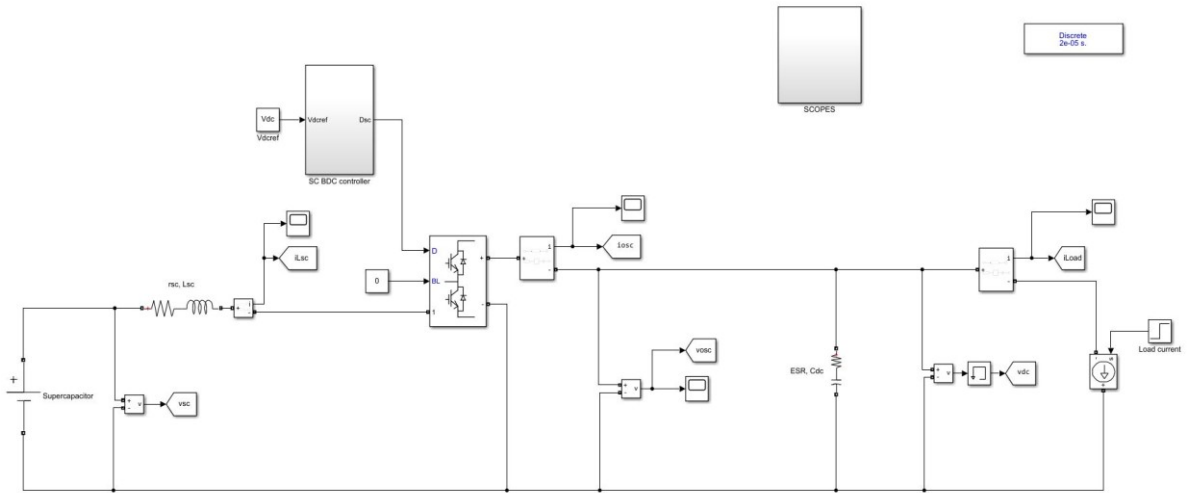

Figure B.4: Battery-only connection to the DC grid

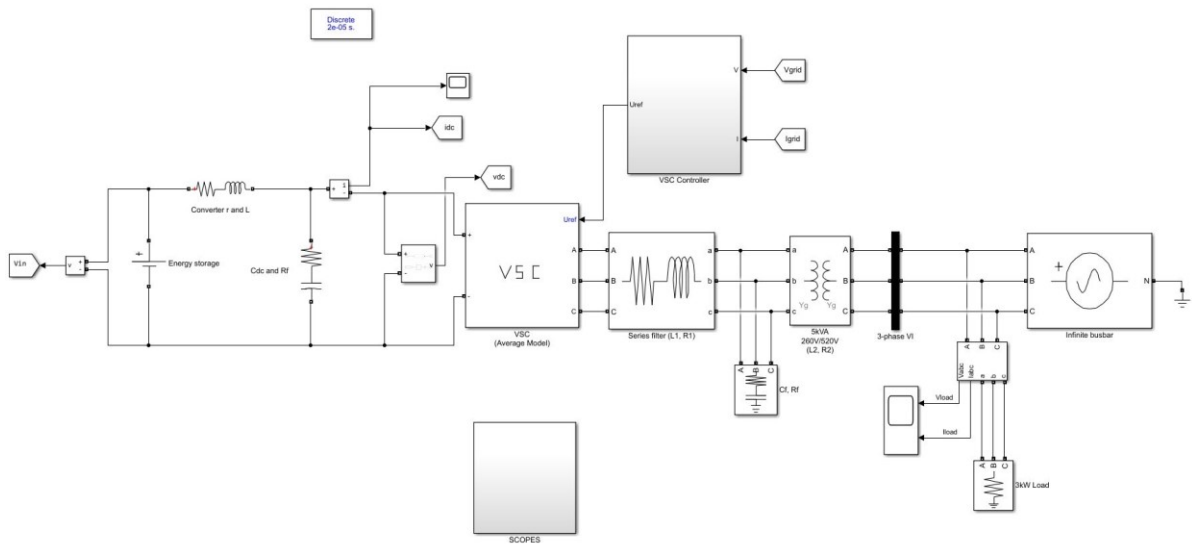**Figure B.5: Supercapacitor-only connection to the DC grid**
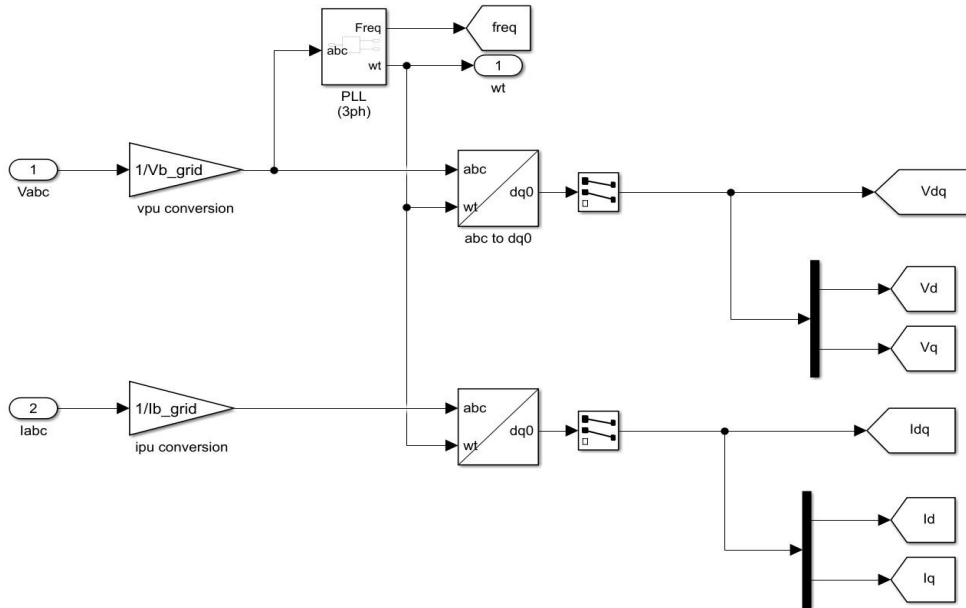

Figure B.6: Standalone AC system
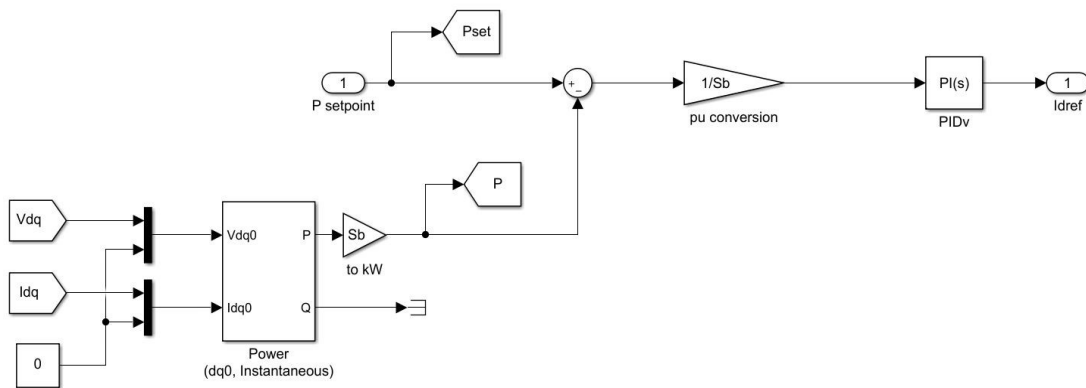
Figure B.7: PLL and measurements subsystem
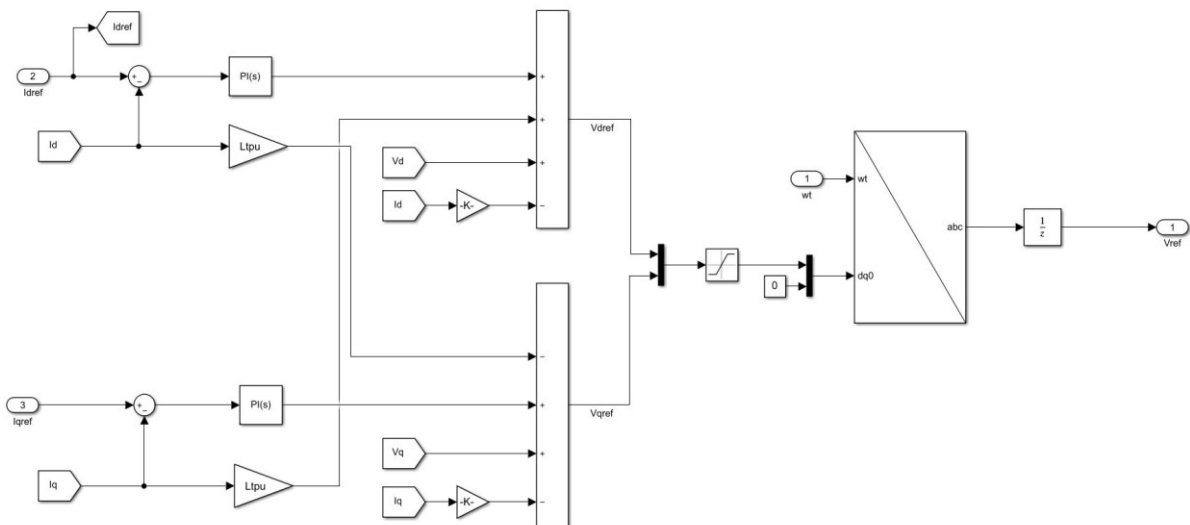

Figure B.8: VSC outer controller

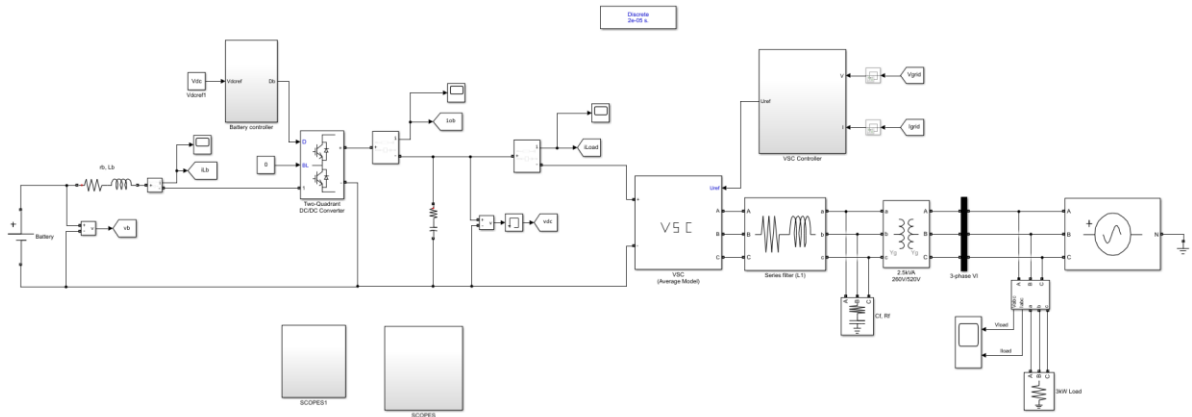**Figure B.9: VSC inner current controller**

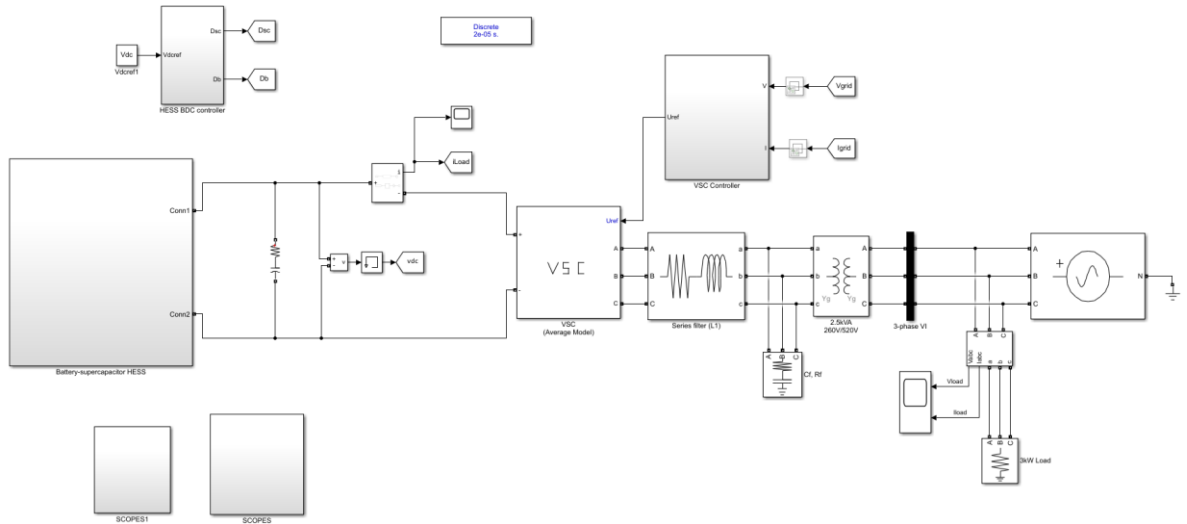**Figure B.10: Battery connection in hybrid DC/AC power system**

Figure B.11: HESS connection in hybrid DC/AC power system

C Park and Clarke's transformation systems

Transformation	Transforms	Matrix for transformation
Clarke	abc to $\alpha\beta$	$\frac{2}{3}\begin{pmatrix} 1 & -\frac{1}{2} & -\frac{1}{2} \\ 0 & \frac{\sqrt{3}}{2} & -\frac{\sqrt{3}}{2} \end{pmatrix}$
Inverse Clarke	$\alpha\beta$ to abc	$\begin{pmatrix} 1 & 0 \\ -\frac{1}{2} & \frac{\sqrt{3}}{2} \\ -\frac{1}{2} & -\frac{\sqrt{3}}{2} \end{pmatrix}$

Park	$\alpha\beta$ to dq	$\begin{pmatrix} cos\theta & sin\theta \\ -sin\theta & cos\theta \end{pmatrix}$
Inverse Park	dq to $\alpha\beta$	$\begin{pmatrix} cos\theta & -sin\theta \\ sin\theta & cos\theta \end{pmatrix}$

Table C.1: Park and Clarke's transformations details